

**HYPERSENSPECTRAL IMAGING USING SILICON  
MICROMACHINED VIBRATORY GRATING SCANNER**

**CHEO KOON LIN**

*(B. Eng., M. Eng, National University of Singapore)*

**A THESIS SUBMITTED  
FOR THE DEGREE OF DOCTOR OF PHILOSOPHY  
DEPARTMENT OF MECHANICAL ENGINEERING  
NATIONAL UNIVERSITY OF SINGAPORE**

**2013**

To my parents and my wife for their love, support and encouragement

# DECLARATION

I hereby declare that this thesis is my original work and it has been written by me in its entirety.

I have duly acknowledged all the sources of information which have been used in this thesis.

This thesis has also not been submitted for any degree in any university previously.

A handwritten signature in black ink, appearing to read 'Cheo Koon Lin', with a stylized, cursive script.

Cheo Koon Lin

14<sup>th</sup> February 2013

# Acknowledgements

First and foremost I would like to extend my deepest gratitude to my supervisors, Assoc. Prof. Zhou Guangya and Assoc. Prof. Chau Fook Siong who continuously conveyed a spirit of adventure in research and scholarship. Without their guidance and persistence this dissertation would not have been possible.

I would also like to thank my fellow lab mates in Micro and Nano Systems Initiative (MNSI) in National University of Singapore (NUS): Dr. Yu Hongbin, Dr. Tian Feng, Dr. Du Yu, Dr. Wang Shouhua, Dr. Chew Xiong Yeu and Dr. Mu Xiaojing, for their selfless help and assistance as well as the generous sharing of their knowledge and expertise. It has been great fun and honour to work together with a group of such calibre.

Finally, the love, support and encouragements from my family and especially my wife Grace who had unwaveringly accompanied me on this journey of late nights and weekends working in the lab. Their understanding has enabled me to pursue this research with vigour and confidence.

Once again, many thanks to all,

Cheo Koon Lin

NUS, Singapore

2013



# Publications

## Journal Publications

- [1] **Kelvin K.L. Cheo**, Y. Du, G. Zhou and F.S. Chau, “Post-Corrections of Image Distortions in a Scanning Grating-Based Spectral Line Imager”, *IEEE Photonics Technology Letters*, vol. 25, n. 12, pp. 1103-1106, (2013)
- [2] G. Zhou, **Kelvin K.L. Cheo**, Y. Du, F.S. Chau, H. Feng, Q. Zhang, “Hyperspectral imaging using a microelectrical-mechanical-systems-based in-plane vibratory grating scanner with a single photodetector”, *Optics Letters*, vol. 34, n 6, p 764-766, (2009).
- [3] G. Zhou, **Kelvin K.L. Cheo**, Y. Du, F.S. Chau, “An optically interrogated microgyroscope using an out-of-plane lamellar grating”, *Sensors and Actuators: A Physical*, vol. 154, n 2, p 269-274, (2009).
- [4] Y. Du, G. Zhou, **Kelvin K.L. Cheo**, Q. Zhang, H. Feng, B. Yang and F.S. Chau, “High speed laser scanning using MEMS driven in-plane vibratory grating: Design, modeling and fabrication” *Sensors and Actuators, A: Physical*, vol. 156, n 1, pp. 134-144, (2009).
- [5] Y. Du, G. Zhou, **Kelvin K.L. Cheo**, Q. Zhang, H. Feng and F.S. Chau, “A 2-DOF circular-resonator-driven in-plane vibratory grating laser scanner” *IEEE/ASME Journal of Microelectromechanical Systems*, vol. 18, n 4, pp. 892-904, (2009).
- [6] Y. Du, G. Zhou, **Kelvin K.L. Cheo**, Q. Zhang, H. Feng and F.S. Chau, “A high-speed MEMS grating laser scanner with a backside thinned grating platform fabricated using a single mask delay etching technique” *Journal of Micromechanics and Microengineering*, vol. 20, n 11, 115028 (2010).
- [7] Y. Du, G. Zhou, **Kelvin K.L. Cheo**, Q. Zhang, H. Feng and F.S. Chau, “Double-layered

- vibratory grating scanners for high-speed high-resolution laser scanning” *IEEE/ASME Journal of Microelectromechanical Systems*, vol. 5, n 19, pp. 1186-1196 (2010).
- [8] Y. Du, G. Zhou, **Kelvin K.L. Cheo**, Q. Zhang, H. Feng, and F.S. Chau, “A 21.5kHz High Optical Resolution Electrostatic Double-layered Vibratory Grating Laser Scanner” *Sensors and Actuators, A: Physical*, vol. 168, n 2, pp. 253-261, (2011).

## Conference Proceedings

- [1] G. Zhou, **Kelvin K.L. Cheo**, Y. Du and F.S. Chau, “A novel optical lamellar grating out-of-plane microgyroscope” *IEEE 21st International Conference on Micro Electro Mechanical Systems*, pp. 864-867, (2008).
- [2] G. Zhou, **Kelvin K.L. Cheo**, Y. Du and F.S. Chau, “Hyperspectral imaging using a micro- machined in-plane vibratory grating scanner” *15th International Conference on Solid-State Sensors, Actuators and Microsystems (TRANSDUCERS 2009)*, pp. 1377-1380, (2009).
- [3] G. Zhou, **Kelvin K.L. Cheo**, Y. Du and F.S. Chau, “Built-in optical angular position sensing mechanism for high-resolution vibratory grating scanner” *Proceedings of the 16th International Conference on Optical MEMS & Nanophotonics*, pp. 17-18, (2011).
- [4] Yu Du, **Kelvin K.L. Cheo**, Guangya Zhou, and Fook Siong Chau, “A Spectral Line Imager Based On A MEMS Vibratory Grating Scanner” *IEEE/LEOS International Conference on Optical MEMS and Nanophotonics*, pp.210-211, (2012).
- [5] Y. Du, G. Zhou, **Kelvin K.L. Cheo**, Q. Zhang, H. Feng and F.S. Chau, “A micromachined vibratory sub-wavelength diffraction grating laser scanner” *IEEE/LEOS International Conference on Optical MEMS and Nanophotonics*, pp. 98-99, (2008).
- [6] Y. Du, G. Zhou, **Kelvin K.L. Cheo**, Q. Zhang, H. Feng and F.S. Chau, “Dynamic characterization of a 2-DOF circular resonator-driven vibratory grating scanner with geometric nonlinearity” *Proceedings of the SPIE-The International Society for Optical Engineering, 4<sup>th</sup> International Conference on Experimental Mechanics*, vol. 7522, 75221S (9 pp.), (2009).
- [7] Y. Du, G. Zhou, **Kelvin K.L. Cheo**, Q. Zhang, H. Feng and F.S. Chau, “Synchronized

- laser scanning of multiple beams by MEMS gratings integrated resonant frequency fine tuning mechanisms” *IEEE/LEOS International Conference on Optical MEMS and Nanophotonics*, pp. 81-82, (2010).
- [8] G. Zhou, Y. Du, **Kelvin K.L. Cheo**, H. Yu, F.S. Chau, “Optical scanning with MEMS in-plane vibratory gratings and its applications” *IEEE/LEOS International Conference on Optical MEMS and Nanophotonics*, pp. 21-22, (2010).
- [9] Y. Du, G. Zhou, **Kelvin K.L. Cheo**, Q. Zhang, H. Feng and F.S. Chau, “A 50 kHz micromachined electrostatic driven vibratory grating laser scanner” *Physics Procedia, International Conference on Optics in Precision Engineering and Nanotechnology (ICOPEN 2011)*, vol. 19, pp. 308-314, (2011).
- [10] Y. Du, G. Zhou, **Kelvin K.L. Cheo**, Q. Zhang, H. Feng and F.S. Chau, “A high-speed electrostatic double-layered vibratory grating scanner with very high optical resolution” *16th International Solid-State Sensors, Actuators and Microsystems Conference (TRANSDUCERS'11)*, pp. 2546-2549, (2011).
- [11] G. Zhou, Y. Du, **Kelvin K.L. Cheo**, F.S. Chau, “MEMS-driven diffraction gratings for rapid scanning of laser beams with very high optical resolution” *Proceedings of the SPIE - The International Society for Optical Engineering*, vol. 8191, 819105 (10 pp.), (2011).
- [12] Y. Du, G. Zhou, Q. Zhang, H. Feng, **Kelvin K.L. Cheo**, B. Yang and F.S. Chau “Micromachined high speed, high optical efficiency laser scanner using sub- wavelength diffraction grating” *22<sup>nd</sup> European Conference on Solid-State Transducers (Euroensors XXII)*, Dresden, Germany, pp. 1373-1376, (2008).

# Table of Contents

Acknowledgements.....	I
Publications.....	II
Table of Contents.....	VI
Summary .....	VIII
List of Symbols and Acronyms.....	XVI
1. Introduction .....	1
1.1. Motivation and background .....	1
1.2. Contribution .....	5
1.3. Structure .....	6
2. Principles and Status of Hyperspectral Imaging .....	7
2.1. Spectral Imaging System.....	7
2.1.1. Hyperspectral Imaging .....	7
2.1.2. Classifications of imaging techniques.....	10
2.1.3. Common Artifacts in Spectral Imaging .....	13
3. MEMS Grating Scanner for Hyperspectral Imaging.....	15
3.1. Principle of the MEMS grating scanner.....	15
3.2. MEMS Grating Scanner Development .....	24
3.2.1. Fabrication process flow for grating platform and connection pillar .....	28
3.2.2. Fabrication process flow for 2-DOF electrostatic comb-driven circular resonator.....	29
3.2.3. Post-assembly process.....	31
4. Hyperspectral Imaging in Double Galvano-Mirror Configuration .....	35
4.1. Configuration Overview.....	35
4.2. Optical Model.....	36
4.2.1. Spectral Resolution.....	39
4.2.2. Spatial Resolution.....	40
4.2.3. Theoretical Limits.....	41
4.3. Correction of Distortion .....	44
4.4. Post Signal Processing .....	50
5. Double-Galvano Mirror Implementation .....	52
5.2. Optical Setup and Procedure .....	52

5.3.	Results .....	59
5.3.3.	Summary .....	61
5.4.	Zeroth-order Optical Feedback .....	62
6.	Single-Galvano Mirror Configuration.....	70
6.1.	Overview .....	70
6.2.	Image Processing.....	71
6.2.3.	Delaunay Triangulation .....	72
6.2.4.	Processing Steps.....	73
6.3.	Single-Galvano Mirror Optical Modelling.....	76
6.3.3.	Sampling Points Modelling .....	76
6.3.4.	Optical Performance .....	79
7.	Single-Galvano Mirror Implementation.....	82
7.1.	Electronics Setup.....	82
7.2.	Optical System Setup .....	84
7.2.3.	Optical Alignment and Calibration .....	86
7.2.4.	Sample Target and Enclosure.....	98
8.	Conclusion.....	104
	References.....	108

# Summary

Spectral imaging combines the advantages of two well-known scientific methodologies, namely imaging and spectroscopy. A spectral imager basically outputs a stack of images of a scene or a sample acquired in continuous bands over a spectral range. A traditional grating spectrometer measures spectral amplitude by dispersing the wavelengths of the incoming light over a range of angles. The spectral amplitude can be measured by using an array of detectors or by rotating the grating and using a single detector.

Current systems are however large and expensive. Miniaturization would potentially open up new applications in portable devices. The MEMS grating scanner provides an exciting platform for a low-cost, hand-held hyperspectral imager to be realized.

The MEMS grating scanner performs scanning through the in-plane rotation of a diffraction grating platform, with the rotated angle of the platform directing the path of the diffracted beam. The platform is allowed to rotate through connected resonating structures. Actuating the device involves electrostatically driven comb-fingers. The in-plane rotation of the platform significantly minimised the major hurdle of high-speed scanning devices: dynamic deformation of the optical platform. High speed, large aperture and large optical scanning range are thus possible for grating scanners.

As a grating element is used in the optical beam scanning, it introduces unique characteristics of its own. Firstly, the grating element diffracts the incoming beam of light into its constituent wavelengths, with different wavelengths having a different diffracted angle. Secondly, different diffraction orders with different optical intensities result. Thirdly, the scanned-line might not be straight: some bowing might occur.

To understand how MEMS grating scanner would fit into a hyperspectral imaging system, we established the model of the scanning mechanism of the MEMS grating scanner and what characteristics it possesses. In our first configuration, we performed a slow scan of the spectral information and a fast scan of the spatial information. We achieve this by doing a slow adjustment of the incident and diffracted angle of the beams that reach a single photodetector and a fast spatial scan through the rotation of the gratings scanner. This setup requires a high-speed scanning mechanism, which the grating scanner fulfills. Two galvano mirrors are used to steer the incident and reflected beam angles of the grating scanner, thereby determining which dispersed wavelength reaches the photodetector. A pin-hole is placed before the detector to select the wavelength that enters the detector. A single-point highspeed avalanche photodiode detects the intensity of the resultant beam. The two galvano mirrors have to traverse synchronized through a predetermined angular relationship governed by the dispersion characteristics of the binary grating. The resultant data collected are sequential spatial information of specific wavelengths. Post-signal processing was employed to reconstruct the spectral image.

The first configuration suffered from complexity of the optical system and complying electronics. This results in limitations in the spectral range and miniaturization potential. To overcome this, a second configuration is proposed by taking advantage of the increased computational capabilities of present systems. Instead of a hardware-based distortion correction mechanism, a software approach was implemented. All of the sampled data points can be correlated to their actual wavelength and spatial location. From this known distorted image map, a corrected profile where the wavelengths and spatial points are linearly distributed is required, of which the points are known. Since the locations of the corrected points will not likely fall correspondingly to the acquired points, some way of mapping one onto the other is required. A post-processing algorithm incorporating Delaunay Triangulation

IX



(DT) is used for minimising the furthest distance of the neighbouring points of which to select for each corrected points, thereby improving the accuracy of the subsequent interpolation step. This second configuration simplifies the overall optical system by only requiring a single galvano-mirror, reducing the electronics driving synchronization requirements and also improves the overall miniaturization potential.

# List of Figures

Figure.1.1. Schematic showing the typical gimbaled scanning mechanism of an optical flat mirror .....	1
Figure 1.2 Schematic showing the scanning mechanism of the grating scanner.....	3
Figure 1.3 a). Schematic showing the deformation of an optical flat mirror at high frequency operation. b). Grating scanner remains flat even operating at high frequencies.....	3
Figure 2.1. Schematic showing the data acquisition domain for the various schemes [20]...	12
Figure 2.2. Schematic illustrating smile and keystone artifact (Fisher et al 1998) .....	14
Figure 3.1. Schematics showing the parameters in the model .....	15
Figure 3.2. Schematic showing the change in period with respect to rotation angle.....	16
Figure 3.3. Schematic showing the model for the projection screen.....	18
Figure 3.4. Simulated scan lines with varying grating pitches.....	20
Figure 3.5. Simulated scan lines with varying angle of incidences.....	21
Figure 3.6. Graph showing the close approximation for the linear model.....	23
Figure 3.7. SEM image showing the MEMS grating scanner device with the inset showing the sectional profile of the fabricated gratings.....	24
Figure 3.8. Schematic illustration of the assembled electrostatic double-layered vibratory grating scanner with a 5mm diameter grating platform.....	26
Figure 3.9. Schematic illustration of the grating platform with connection pillar.....	27
Figure 3.10. Schematic illustration of the 2-DOF electrostatic comb-driven circular resonator.....	28
Figure 3.11. Fabrication process flow for the diffraction grating, grating platform and connection pillar.....	29

Figure.3.12. Fabrication process flow for the 2-DOF electrostatic comb-driven circular resonator.....	30
Figure 3.13. Schematic illustration of the post-assembly process.....	31
Figure 3.14. Microscope image showing the (a) whole view (b) part view of the assembled double-layered vibrating grating scanner with a 3mm diameter grating platform. ....	33
Figure. 3.15. Photographic image showing the assembled double-layered vibrating grating scanner on a PCB substrate.....	33
Figure. 3.16. Schematic illustration of the experimental setup for the prototype double-layered vibratory grating scanner.....	34
Figure 4.1. Schematic illustration showing the simplified model of the proposed hyperspectral imager.....	37
Figure 4.2. Schematic showing the parameters involved in the algorithm.....	41
Figure 4.3. Graph showing ratio $\gamma/\delta\theta$ with varying normalized wavelengths and field angles.....	43
Figure 4.4. Graph showing ratio $\gamma/\delta(\lambda/\Lambda)$ with varying normalized wavelengths and field angles.....	44
Figure 4.5. Schematic illustration showing the “smile” and spectral keystone distortions.....	45
Figure 4.6 Simulated scan bow before and after correction with wavelengths of (a) 450nm and (b) 850nm respectively.....	46
Figure 4.7. Simulated relationship between the rotation angle and the wavelengths to correct the spectral keystone distortions.....	47
Figure 4.8. Simulated scan bow at different wavelengths after corrections of the “smile” and spectral keystone distortions.....	48

Figure 4.9. Schematic of a miniature double galvano-mirror hyperspectral imager a with MEMS vibratory grating scanner.....	49
Figure 5.1. Schematic showing the optical configuration for the proof-of-concept.....	53
Figure 5.2. The optical setup used in the experiment.....	54
Figure 5.3. Incident and diffracted angles required for bow-free scanning for 500nm pitch grating.....	54
Figure 5.4. The signal synchronization and control necessary in the imaging system.....	56
Figure 5.5. Optical setup showing stable laser spots when grating scanner at resonance.....	57
Figure 5.6. Schematic showing the driving voltages for both galvano-mirrors.....	58
Figure 5.7. Post-processed spectral image with insets showing the detailed spot profiles.....	60
Figure 5.8. Schematic showing the spectral cross-section profile of the laser diodes.....	61
Figure 5.9. Incident and diffracted angles required for bow-free scanning with 400nm grating.....	61
Figure 5.10. Graph showing the percentage drop in overall intensity of the first-order diffracted beam as the grating platform is rotated with respect to an incident TM-polarized beam.....	63
Figure 5.11. Schematic of the optical setup to measure the zeroth-order beam.....	65
Figure 5.12. Intensity profile of zeroth-order beam at orthogonal polarization angles of (a) $0^\circ$ and (b) $90^\circ$ .....	66
Figure 5.13. Graph showing the profile of the intensities obtained for the zeroth-order beam as the polarizer and the rotation angle of the grating is changed.....	67

Figure 5.14. Zeroth-order peak voltage with respect to the optical scan angle during resonance operation.....	68
Figure 5.15. Real-time sinusoidal driving voltages and acquired detector readings for the zeroth-order beam.....	68
Figure 6.1. Schematic illustration showing three major image distortions in the proposed spectral imager and meshed network using DT on a modelled 10x10 set of points.....	74
Figure 6.2. Schematic illustration showing meshed network using DT on a modelled 10x10 set of points with the desired Cartesian grid .....	75
Figure 6.3. Schematic illustration of obtaining intensity of a data point in the correct profile using linear interpolation.....	76
Figure 6.4. Schematic illustration showing the configuration of the improved scanning grating based hyperspectral imaging system.....	76
Figure 6.5. Flowchart of obtaining corresponding spatial and spectral positions of each sampled data point using reverse ray-tracing.....	79
Figure 6.6. Schematic illustration of a single galvano-mirror miniature hyperspectral imager using MEMS vibratory grating scanner.....	80
Figure 7.1. Schematic showing all the electronics involved in the operation, synchronization and data acquisition of the spectral imaging system.....	83
Figure.7.2. Picture of the optical system aligned on an optical isolation table with one side of the enclosure removed.....	84
Figure 7.3. Photographic image showing the (a) imaging slit and (b) rectangular pinhole....	85
Figure 7.4. Visual representation of the spectral image characteristics simulated at fewer data points.....	85
Figure 7.5. Summary of new system parameters and the predicted performance.....	86

Figure 7.6. Picture showing the red laser diode being used to calibrate the system and the inset shows the close-up view .....	87
Figure 7.7. Picture showing the raw data map .....	88
Figure 7.8. Picture showing the data points being mapped to its spatial and spectral locations .....	89
Figure 7.9. Picture showing the final distortion corrected Cartesian spectral map .....	90
Figure 7.10. Picture showing the recalibrated system based on the 635nm red laser diode.....	90
Figure 7.11. Picture showing the single-mode visible wavelength optical fiber with the stage assembly .....	92
Figure 7.12. Figure showing the post-processed spectral image for red (top) and green (bottom) lasers .....	93
Figure 7.13. Figures showing the acquired images for 632.8nm red laser from (a) 20mm up, (b) 10mm up, (c) 10mm down and (d) 20mm down .....	95
Figure 7.14. Figures showing the acquired images for 532.8nm green laser from (a) 20mm up, (b) 10mm up, (c) 10mm down and (d) 20mm down .....	98
Figure 7.15. Photograph and parameters of the LED target .....	99
Figure 7.16. (a) Picture of the complete enclosure and all the electronic instruments used in the operation and testing of the system. (b) Picture showing setup when illuminated by the LED array .....	100
Figure 7.17. Corrected hyperspectral image of the LED target .....	101
Figure 7.18. Intensity map image of the LED target .....	101
Figure 7.19. Comparison of LEDs expected datasheet spectrum and acquired spectrum for (Left) green LED and (right) blue LED.....	102

# List of Symbols and Acronyms

$\theta$	Field angle
$\theta_p$	Polarizer angle
$\alpha$	Incident angle
$\beta$	Diffraction angle
$\phi$	Rotation angle
$\gamma$	Slope angle, out-going diffracted ray makes with the optical axis
$\lambda$	Wavelength
$\Lambda$	Grating period
$\Lambda_x$	Effective grating period X-axis
$\Lambda_y$	Effective grating period Y-axis
$d$	Grating diameter
$\vec{e}_x$	Unit vector along X-axis
$\vec{e}_y$	Unit vector along Y-axis
$\vec{e}_z$	Unit vector along Z-axis
$f$	Focal length

$k_x^i$	Incident wavevector X-axis
$k_y^i$	Incident wavevector Y-axis
$k_x^m$	$m^{th}$ order diffracted wavevector X-axis
$k_y^m$	$m^{th}$ order diffracted wavevector Y-axis
$m$	Diffraction order
$\vec{r}$	Normalized wavevector
$R'_x$	Projected X-axis coordinate on screen
$R'_y$	Projected Y-axis coordinate on screen
ADC	Analog to Digital Convertor
APD	Avalanche Photo Detector
DAQ	Data Acquisition
GUI	Graphical User Interface
FOV	Field of View
FWHM	Full Width Half Maximum
LED	Light Emitting Diode
NI	National Instruments
PCB	Printed Circuit Board
PMT	Photo Multiplier Tube



# 1. Introduction

## 1.1. Motivation and background

Since the first publication of a miniature spatial light modulator [1], the field of microoptoelectromechanical systems (MOEMS) has been growing from strength to strength. The possibility of a micro-scale optical processing engines opens up new applications [2]. Perhaps one of the most successful stories is the digital micromirror device (DMD) from Texas Instruments. It has found widespread adoption in projector displays, digital cinemas and large-screen TVs [3]. Other notable developments include display applications using grating light valve (GLV) [4] and optical switches for networking [5].

One of the most common devices is the MEMS optical micromirror. These micromirrors typically have a smooth flat platform being used as a mirror surface. This platform is then supported along one or two axes which allow the platform to rotate about them (single or double gimbaled). The rotated angle of the mirror redirects an incoming beam of light, see Fig.1.1.

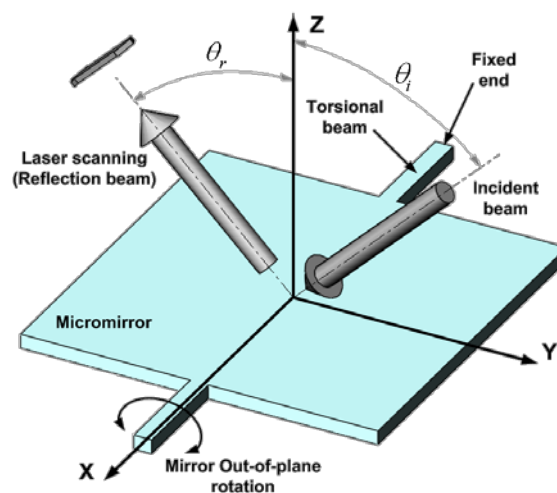


Figure.1.1. Schematic showing the typical gimbaled scanning mechanism of an optical flat mirror

Several variations have been proposed over the years, which have found applications in wavelength-selective switches [6] and optical crossconnects [7]. Micromirrors have received much attention as the miniature size of device implies low inertia, which translates to potentially higher operating frequencies compared to macro-scanners. As they can also be batch fabricated not unlike ICs, they are therefore cheap to produce. A promising direction had been the development of high-resolution projection engines. However, such engines would require the micromirrors' operating frequency to be in the tens of kilohertz. Current designs are not capable of meeting this requirement without optical degradation due to dynamic non-rigid-body deformation of the mirror platform. Minimizing dynamic non-rigid-body deformation of high-speed out-of-plane micromirror scanners would typically require thicker micromirror platforms, which in turn lowers the resonating and operating frequency. Thus, some form of balance needs to be struck between frequency and optical performance.

It is on this basis that the concept of a grating scanner was developed [8]. The grating scanner performs scanning through the in-plane rotation of a diffraction grating platform, with the rotated angle of the platform directing the path of the diffracted beam (Fig. 1.2.). The zeroth-order beam reflects directly off the grating regardless of the platform's orientation. The platform is allowed to rotate through connected resonating structures. Actuating the device involves electrostatically driven comb-fingers.

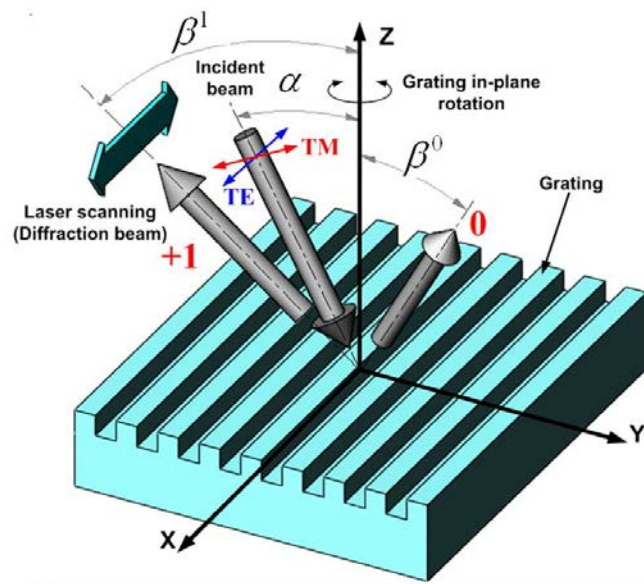


Figure 1.2 Schematic showing the scanning mechanism of the grating scanner

The in-plane rotation of the platform significantly minimised a major hurdle of high-speed scanning devices: dynamic deformation of the optical platform (Fig. 1.3.). High speed, large aperture and large optical scanning range are thus possible for grating scanners.

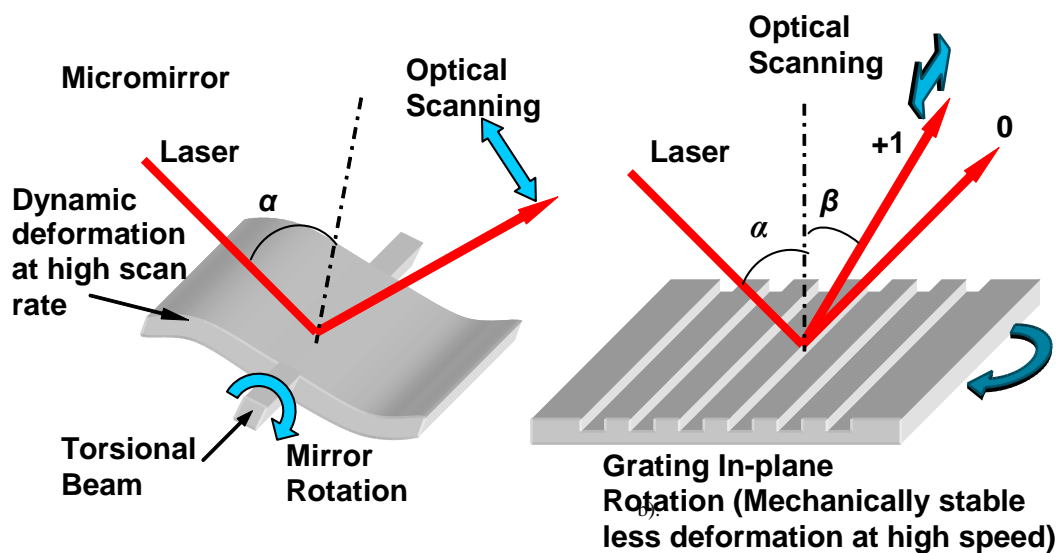


Figure 12.1.1.3 a). Schematic showing the deformation of an optical flat mirror at high frequency operation.

b). Grating scanner remains flat even operating at high frequencies

Previous work had been on the device design, optical modelling, structural analysis and multi-grating analysis. Several milestones had been achieved along the way.

Firstly was the establishment of the grating design model required to optimise the scan quality [9]. Due to the fact that the scanning mechanism is based on the diffraction characteristic of the grating rather than the reflection off a plane mirror, there arises bowing in the projected scan lines. Also, the incoming beam is diffracted into several orders of varying intensities depending on the grating pitch and incoming beam angle. Our previous work established the model and experimental verification that optimises minimal bowing in the scan lines and maximum optical efficiency by working in the 1<sup>st</sup>-order diffraction.

Secondly was the grating fabrication which optimised the optical efficiency of the reflected beam [10]. More than 75% of the optical intensity of incident beam was diffracted off the grating was achieved for scanning for a binary sub-wavelength grating.

However, as a grating element is used in the optical beam scanning, it does introduce unique characteristics of its own. Firstly, the grating element diffracts the incoming beam of light into its constituent wavelengths, with different wavelengths having a different diffracted angle. Secondly, different diffraction orders with different optical intensities result. Thirdly, the scanned-line might not be straight: some bowing might occur. All of these issues had been addressed in our previous work [9] and we have established and verified design guidelines to minimize these effects. We have

- established a grating design guideline that optimises the diffraction efficiency for the 1<sup>st</sup>-order diffraction
- verified the incident and diffracted angles that results in a bow-free scan line

The dispersive nature and the scanning capability of the grating scanner open up other potential applications for the technology. Spectral imaging, which is a combination of spectroscopy and imaging, is one potential candidate. Typical systems rely on a dispersive element like a grating, and an array detector to obtain the spectral image. However, utilizing single pixel detectors is an attractive prospect for miniaturization as well as for delivering a wide variety of wavelengths. This is particularly true for infrared systems where array detectors are expensive and complex due to the need for thermal cooling.

A single pixel detector configuration requires high-speed scanners to direct selected spectral bands from each spatial point to the detector. At the same time, a dispersive element is needed to split the light from each spatial point into its spectral constituents. A high-speed micromachined vibratory grating scanner satisfies both criteria.

## **1.2. Contribution**

With the grating scanner's characteristics and performance well established, the aim of this work is to investigate possible spectral imaging configurations which the device will be uniquely suited.

This work looks into the development of a spectral imaging system with a hyperspectral resolution capability. It is then necessary to decide how best to incorporate the grating scanner into a viable system and what, if any, competitive advantages the grating scanner can offer to the field. Understanding the limitations will permit considerations of techniques which can be applied to overcome them. It will also serve as a platform to further explore other potential applications for the grating scanner.

### **1.3. Structure**

The following chapters proceed to shed light on the development of a hyperspectral imaging system based on a MEMS grating scanner. Chapter 2 first explores the background on spectral imaging and the various configurations and issues.

Chapter 3 then develops a model for the grating scanner operation and its development.

Chapter 4 describes the optical model of the first configuration of the spectral imager utilizing double galvano-mirrors.

Chapter 5 shows the experimental setup for the double galvano-mirror configuration and the results obtained.

Chapter 6 then describes the model for a second configuration using a single galvano-mirror

The experimental results, optical alignments and calibration steps are discussed in Chapter 7 with finally a summary in Chapter 8.

## 2. Principles and Status of Hyperspectral Imaging

This chapter looks into the basis for spectral imaging systems and looks at how the grating scanner can be ideally suited.

### 2.1. Spectral Imaging System

#### 2.1.1. Hyperspectral Imaging

Spectral imaging [11] combines the advantages of two well-known scientific methodologies, namely imaging and spectroscopy. A spectral imager basically outputs a stack of images of a scene or a sample acquired in continuous bands over a spectral range. A traditional grating spectrometer measures spectral amplitude of each spectral band by dispersing the wavelengths of the incoming light over a range of angles. The spectral amplitude of each band can be measured by using an array of detectors or by rotating the grating and using a single detector.

Spectral imaging is often differentiated based on their spectral resolution. What is known as panchromatic imagers [44] are those that view the image in a single waveband. Multispectral imagers have 3-12 multiple filters. A RGB camera would be a good example of such a system. Multi-channel cameras [32] are also possible to acquire a higher number of wavebands. A useful figure of merit to classify more powerful system is called relative spectral resolution, which is the absolute spectral resolution divided by the length of the viewable spectrum. Ultraspectral imagers have relative spectral resolution of 0.1 while hyperspectral systems are characterised by having tens or hundreds of wavebands and a relative spectral resolution order of 0.01 [12]. Hyperspectral imagers thus are systems with

much higher spectral resolution over a continuous spectrum. This is necessary for a more powerful discrimination capability. By obtaining the spectra for each pixel, this enables all the tools and algorithms of standard image processing techniques to be combined with the spectral interrogation, classification and correlation techniques to deliver extended analysis capability on the scene.

For such systems, the spectral wavebands can be defined to optimize the discrimination of various colours, absorption band edges and band depth in an image. Any set of wavebands can then be defined within the total spectral bandwidth and spectral resolution of that cube by computer manipulation. The wavebands can be adjusted and need not be continuous. This capability greatly enhances the ability of the hyperspectral imager to adapt to almost any imaging situation. The objective is then to correlate the image pixel spectra with known material spectra. This allows the identification of the material(s) in each pixel and even the ability to quantify the amount of different materials within a pixel via spectral unmixing [13]. With this information, 2 dimensional spatial distribution maps can be constructed of identified materials in the object scene.

The ability of hyperspectral imager to measure reflectance, absorption band depth and spectral edge shifts over time coupled with spatial information creates the possibility to analyse material changes. For example in remote sensing applications, the shift in the chlorophyll band edges of observed vegetation indicates stress [13]. Other potential applications of hyperspectral imaging include mineral identification in geology, terrain classification and camouflaged target detection in defense systems, on-line inspection of food products, coastal and inland water studies, environmental hazards monitoring and tracking, cancer detection in biomedical and life sciences.



Current systems are however large and expensive. Miniaturization would potentially open up new applications in portable devices. The grating scanner provides an exciting platform for a low-cost, hand-held hyperspectral imager to be realized.

Miniaturization brings about challenges in the optical system. In order to separate light into its constituents, some dispersive element like a grating is typically necessary. Differentiating large number of narrow spectral bands is helpful where the detector is placed further away so that light can be dispersed. In a confined space, the dispersion quality of the element needs to be stronger. However, more pronounced distortions in the spectral distribution occur.

Alternative mechanisms have been explored which are more computational based like compressive sensing [26] to reduce the acquisition process of a spectral image. First discussed in [33], compressed sensing is based on the fact that signals encountered are sparse in some domain, and such sparsity are exploited through reducing the number of sampling points required. Coded Aperture Snapshot Spectral Imaging (CASSI) [34] is such a imaging architecture that allows the capturing spectral imaging information of a 3D cube with just a single 2D measurement of the coded and spectrally dispersed source field. The intensities of the optical image have to be modulated to implement measurement patterns on the image plane. Means of generating the modulation patterns include relay lens/prism structure [43] and spatial light modulators [45]. Such developments have garnered interest in recent years, including using MEMS DMD devices [42] as the modulation mechanism.

We will look at the system in further details in the following sections.

### **2.1.2. Classifications of imaging techniques**

Spectral imagers may be divided into classes based on two aspects: the methods by which they achieve spatial and spectral discriminations. Spatial discriminations include whiskbroom, pushbroom, framing and windowing [14].

Whiskbroom-scanning instrument employs a zero-dimensional or spot or point field-of-view (FOV) which scans the object in both the along-track and cross-track directions. The complete spectral information is acquired at the same time through passing the spot through a dispersive element and a linear array of detectors. Such a system is simple to implement, low-cost due to the number of components and ease of calibration and maintaining accuracy. Being a spatial scanning-based system has the fundamental drawback of a distorted image if the scanning is not done fast enough. This is especially evident when the relative motion in the scene during the acquiring process is large.

A pushbroom-scanning [20] instrument employs a 1-D FOV which is scanned in one direction. Typically the scan direction for a pushbroom-scanning instrument is the along-track direction but there are examples of pushbroom instruments that scan in the cross-track direction. In most pushbroom instruments, the restriction of the FOV is obtained by placing a slit aperture in an intermediate focal plane. This is one of the more common techniques. By acquiring the spectral information of the whole 1-D FOV at the same time, this technique allows a longer integration time per pixel. Thus pushbroom imaging spectrometers offer the signal-to-noise ratio performance that is required for orbiting platforms or systems which are imaging weaker signals. However, the sensor array necessary for such a task would be a 2-D detector. The recovered spectrum from a pushbroom sensor potentially can contain substantial artifacts that compromise identification of the feature's composition. Further, pushbroom spectrometer artifacts can cause pixel classification algorithms to fail by

producing many nonphysical spectral signatures [15]. Volume holographic lenses [39][40] provides a way to achieve high resolution in the spatial dimension as well as the spectral dimension concurrently.

Comparatively, a whiskbroom imager can achieve the highest spectral and spatial uniformity as calibration needs to be done to a relatively smaller 1-D array of detectors. Thus, it is more appropriate for airborne than orbiting platforms as they cannot easily provide adequate signal-to-noise ratio performance from orbit owing to the limited integration time.

A framing instrument employs a 2-D FOV, which remains fixed on the object during acquisition, though multiple acquisitions may be required to cover an object of general length in the along-track direction.

Windowing is a new class of instrument that employ 2-D FOV that moves across the object in a continuous fashion in the along-track direction. Windowing is actually distinct from the time-delay integration technique used by some panchromatic imagers. In a windowing instrument, a distinct exposure is acquired each time the FOV moves forward by one ground sample and no integration occurs.

An illustration showing the relative imaging techniques is shown in Fig.2.1. A three dimensional spectral cube is shown with  $x$ ,  $y$  spatial locations and  $\lambda$  being the wavelength. A whisk-broom scanner mechanism (a) collects all the spectral information of a single spatial location at a time. The spatial points of the image plane are collected sequentially. A filtered camera (b) images the whole image plane at a given waveband,  $\Delta\lambda$ , in a snapshot. The spectral cube is completed through mapping through different wavebands. Finally, a pushbroom mechanism (c) acquires the whole spectral distribution of a spatial line  $x$ . The  $y$  coordinate is scanned to complete the spectral cube.

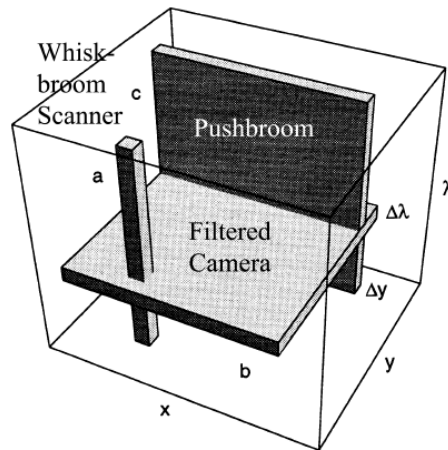


Figure 2.1. Schematic showing the data acquisition domain for the various schemes [20]

Methods of acquiring spectral information include filtering, dispersive and interferometric techniques. Dispersive instruments may use either a prism or grating. Essentially, incoming beams are dispersed into its constitutional wavelengths and a single or a linear array of detectors is positioned to detect the individual intensities. The simplicity of using dispersive elements makes it highly attractive for cost-effective applications.

The interferometric class are Fourier-transform spectrometers (FTS) [24] [25][41] which are based on two-beam interferometers such as the Michelson, Mach-Zender or Sagnac. Which providing higher resolution, the complexity and the need for tuneable parts to scan through the wavelengths makes such classes more suitable for critical applications. Very narrow bandwidth spectral images can also be obtained through directly modulating and tuning lasers incident on the object [38].

The filtering class includes multiple-beam interferometers such as the Fabry-Perot ,interference and thin-film filters [36] as they obtain spectral discrimination by passing at any instant only a narrow range of wavelengths, while blocking all other wavelengths. In simpler cases, several filters work in tandem to cover the necessary spectrum bands.

Multispectral imagers are a good example where only 3-12 wavelength profiles are required. MEMS-based tunable filters [35] are also attractive alternatives.

The different combinations between the spatial and spectral discriminations techniques open up different configurations for various applications. Though not all permutations are physically realisable, the combinations still provide enough variety to suit most needs and serve as a reference guideline to implementation strategies.

### 2.1.3. Common Artifacts in Spectral Imaging

Spectral imaging comes with its own set of unique issues. Even a simple RGB imager (i.e. camera) has common concerns over the photo-realism of the acquired images.

For high performance imagers, the location of the peak of the spectral response function (SRF) and its half-width (as well as shape) must be known to within a small fraction of the nominal pixel bandwidth, typically less than a few percent. Uncalibrated distortion along the spatial direction (**smile**) [16] as well as the spatial variation of the optical PSF must be kept to a minimum, typically a small fraction of a pixel. Smile is defined as the deviation from straightness of the monochromatic image of the slit.

It is also desirable to reduce the distortion along the spectral direction (called **keystone**). Keystone is the variation of slit magnification with wavelength. This error means that the amount of mixing of the spectra from spatially adjacent pixels will vary with wavelength. This affects the recovered spectrum of pixels located close to sharp boundaries in the image or of targets that are less than a few pixels large. A general keystone tolerance is difficult to give as the effect of the error will depend on the form of the spectra and the optical point spread function (PSF). Both artefacts are illustrated in Fig.2.2. below.

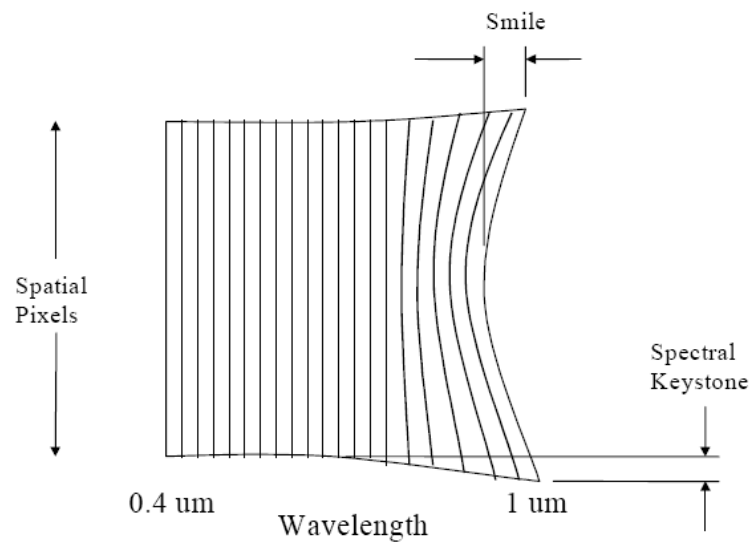


Figure 2.2. Schematic illustrating smile and keystone artifact [28]

The technical origins for both artefacts are different for different systems but both artefacts have to be considered in the system development.

# 3. MEMS Grating Scanner for Hyperspectral Imaging

## 3.1. Principle of the MEMS grating scanner

To understand how MEMS grating scanner would fit into a hyperspectral imaging system, we have to first establish the model of the scanning mechanism of the grating scanner and what characteristics it possesses.

The optical model showing the various angle and axis definitions are shown in Fig.3.1. below.

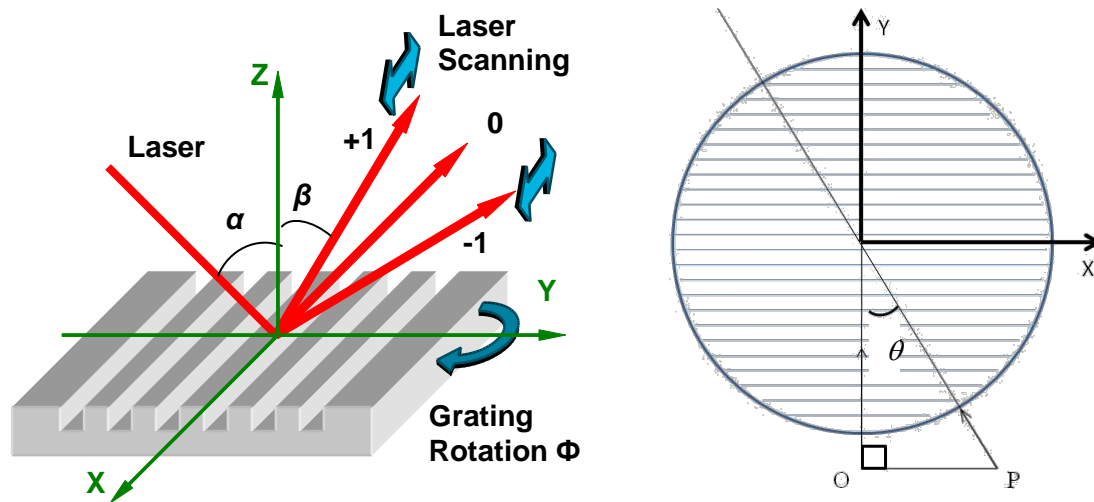


Figure 3.1. Schematics showing the parameters in the model

From the schematics, two angles determine the incident beam from any location on the image plane, the field angle  $\theta$  and the incident angle  $\alpha$ . The field angle  $\theta$  determines the location from angle point parallel to the X-axis, the incident angle  $\alpha$  determines a position parallel to the Z-axis.

The X and Y components of the wave-vector of the chosen  $m^{th}$ -order diffraction beam are given by the well-known grating equation [17]

$$k_x^m = k_x^i - m \frac{2\pi}{\Lambda_x} \quad (1)$$

$$k_y^m = k_y^i - m \frac{2\pi}{\Lambda_y} \quad (2)$$

Where  $k_x^i$  and  $k_y^i$  are the X and Y components of the incident wave-vector,  $\Lambda_x$  and  $\Lambda_y$  are the effective grating periods along the respective X and Y directions.

When the grating is rotated in-plane at an angle of  $\phi$ , the effective grating period becomes (Fig.3.2.)

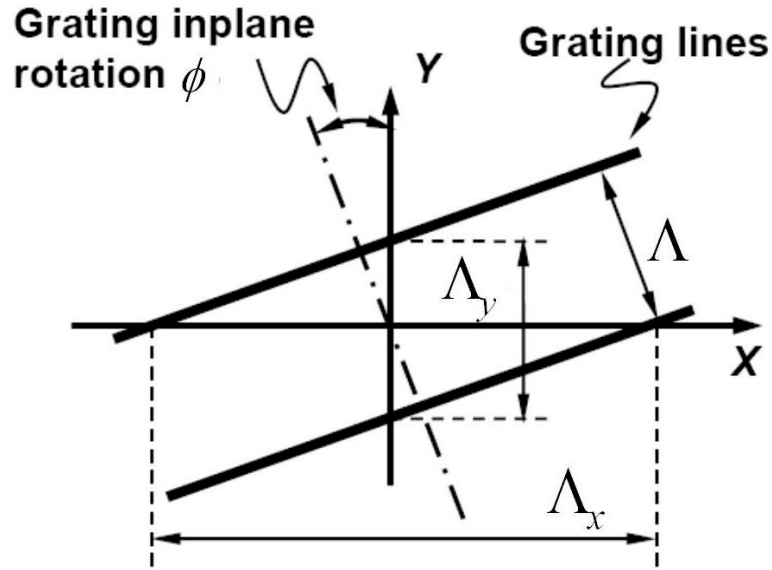


Figure 3.2. Schematic showing the change in period with respect to rotation angle.

$$\Lambda_x = \frac{\Lambda}{\sin \phi} \quad (3)$$

$$\Lambda_y = \frac{\Lambda}{\cos \phi} \quad (4)$$



From Fig.3.1. for a beam from position P at the image plane at angle  $\theta$  and incident angle  $\alpha$  onto the grating,  $k_x^i$  and  $k_y^i$  is shown to be

$$k_x^i = \left( \frac{2\pi}{\lambda} \right) \sin \theta \quad (5)$$

$$k_y^i = \left( \frac{2\pi}{\lambda} \right) \cos \theta \sin \alpha \quad (6)$$

Substituting (5) and (6) into (1) and (2) and recognizing that the Z-component is simply the preservation of the wave-vector, the components of the wave-vector is then

$$k_x^m = -\left( \frac{2\pi}{\lambda} \right) \sin \theta - m \frac{2\pi}{\Lambda} \sin \phi \quad (7)$$

$$k_y^m = \left( \frac{2\pi}{\lambda} \right) \cos \theta \sin \alpha - m \frac{2\pi}{\Lambda} \cos \phi \quad (8)$$

$$k_z^m = \sqrt{\left( \frac{2\pi}{\lambda} \right)^2 - (k_x^m)^2 - (k_y^m)^2} \quad (9)$$

Therefore, the complete normalized wave-vector pointing to the direction of the outgoing  $m^{th}$ -order is shown to be given by

$$\vec{r} = \left( \frac{\lambda}{2\pi} \right) [k_x^m \vec{e}_x + k_y^m \vec{e}_y + k_z^m \vec{e}_z] \quad (10)$$

where  $\vec{e}_x$ ,  $\vec{e}_y$  and  $\vec{e}_z$  are the unit vectors along the X, Y and Z directions respectively. What is obtained here is a general expression that describes how a beam of light would behave after leaving the grating scanner.

For simplicity, we investigate the resultant beam from a single point where  $\theta = 0$ . In this case, (5) and (6) simplify to  $k_x^i = 0$ , and  $k_y^i = \left(\frac{2\pi}{\lambda}\right)\sin\alpha$ . We will determine the resultant scanned lines profiles on a projection screen.

We assume that a projection screen  $X'O'Y'$  is placed at a distance  $l$  from the grating with its normal vector parallel to the direction of the chosen  $m^{th}$  - order diffraction when the grating is at rest (Fig.3.3.).

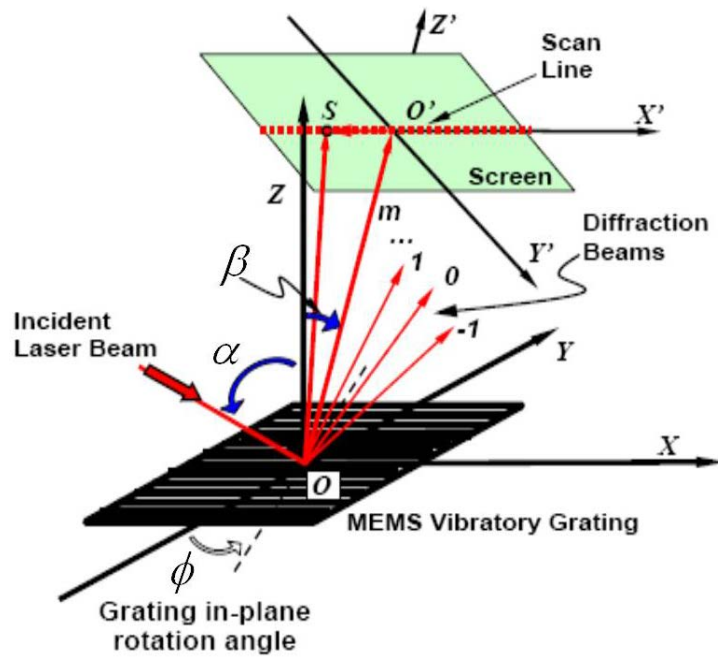


Figure 3.3. Schematic showing the model for the projection screen

To find the projected spot **S** on the screen, we see that

$$\begin{aligned}\overrightarrow{O'S} \perp \overrightarrow{OO'} &\Rightarrow \overrightarrow{O'S} \cdot \overrightarrow{OO'} = 0 \\ &\Rightarrow l\vec{r}(0) \cdot \{t\vec{r}(\theta_R) - l\vec{r}(0)\} = 0\end{aligned}$$

Where  $t$  is the distance from **O** to **S**. Rearranging gives us

$$t = \frac{l}{\vec{r}(0) \cdot \vec{r}(\theta_R)} \quad (11)$$

The projected location on the screen is therefore

$$\vec{R} = \overrightarrow{OS} = t\vec{r}(\theta_R) = \frac{l}{\vec{r}(0) \cdot \vec{r}(\theta_R)} \vec{r}(\theta_R) \quad (12)$$

To find the coordinates of the laser spot on the projection screen  $X'O'Y'$ , we perform a coordinate transform. From Fig.3.3, we can see that  $X'Y'Z'$  coordinates can be obtained by rotating the  $XYZ$  system about the  $X$ -axis through an angle of  $-\beta$  followed by a translation of distance  $l$  towards the positive  $Z$ -direction. The new coordinates of the spot  $\mathbf{S}$  are then

$$\vec{R}' = \begin{bmatrix} R'_x \\ R'_y \\ R'_z \end{bmatrix} = \begin{bmatrix} 1 & 0 & 0 \\ 0 & \cos \beta & -\sin \beta \\ 0 & \sin \beta & \cos \beta \end{bmatrix} \vec{R} - \begin{bmatrix} 0 \\ 0 \\ l \end{bmatrix} \quad (13)$$

This provides us with the complete scanning profile of an incident beam being diffracted.

To establish the scanning mechanism, we look at the  $X$ -component of  $\vec{R}'$

$$R'_x = \left\{ \frac{l}{\vec{r}(0) \cdot \vec{r}(\theta_R)} \right\} \left( -\frac{m\lambda}{\Lambda} \sin \phi \right) = K \left( -\frac{m\lambda}{\Lambda} \sin \phi \right) \quad (14)$$

For small-angle approximations, we can show that  $K \approx l$ , therefore

$$R'_x \approx \left( -\frac{m\lambda}{\Lambda} l \phi \right) \quad (15)$$

The length of the projected line thus has an approximate proportional relationship with the rotated angle of the grating.

Given an incidence angle onto the grating, different wavelengths will be diffracted by different angles in a direction perpendicular to the scan axis. To perform spectral imaging, it is thus possible to pick up the intensities at different diffracted angles to acquire the spectrum profile at the point of scanning. As the grating rotates, the spectrum profile of the line scanned by the grating scanner is thus acquired. However, there are two issues that have to be addressed before the configuration can be adopted successfully.

Firstly, the  $R'_x$  and  $R'_y$  components from (13) allow us to plot the scanned line profile as the grating rotates through  $\phi$ . Fig.3.4. shows simulated scan lines of a first-order diffracted beam on a projected screen at a distance of  $l = 135$  mm from the grating, where the period of the grating is varied from 0.5  $\mu\text{m}$ , 1  $\mu\text{m}$  and 5  $\mu\text{m}$ . The wavelength is assumed to be 635 nm (red), angle of incidence is set at  $20^\circ$  and  $\phi$  is varied from  $-5^\circ$  to  $5^\circ$ .

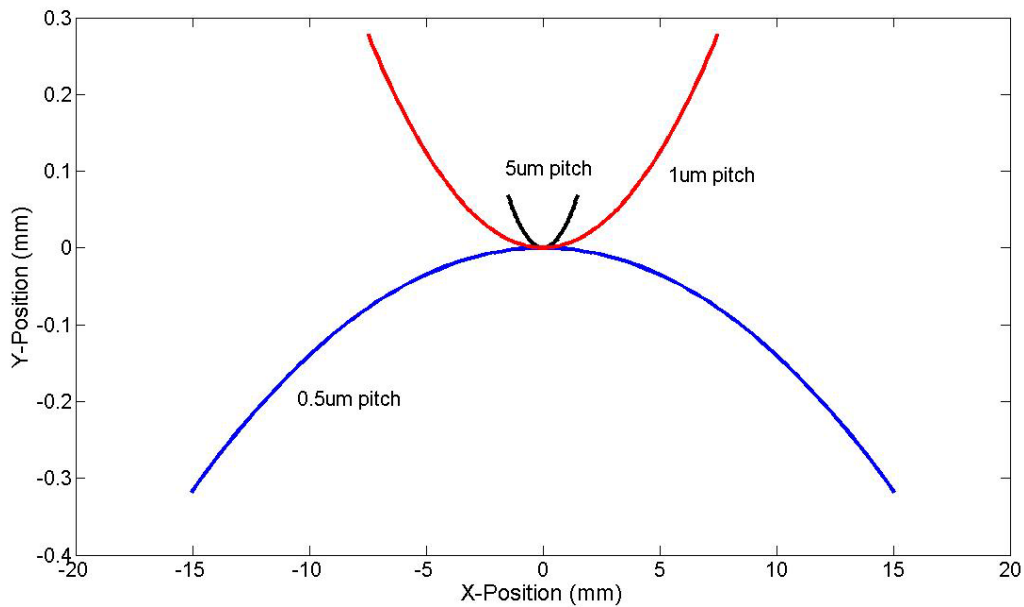


Figure 3.4. Simulated scan lines with varying grating pitches

Besides pitch variation, there is also the issue of incidence angle. Using similar configurations, with the pitch at 0.5 $\mu$ m, 635nm wavelength, the angle of incidence is varied from 15°, 20° and 25° as shown in Fig.3.5.

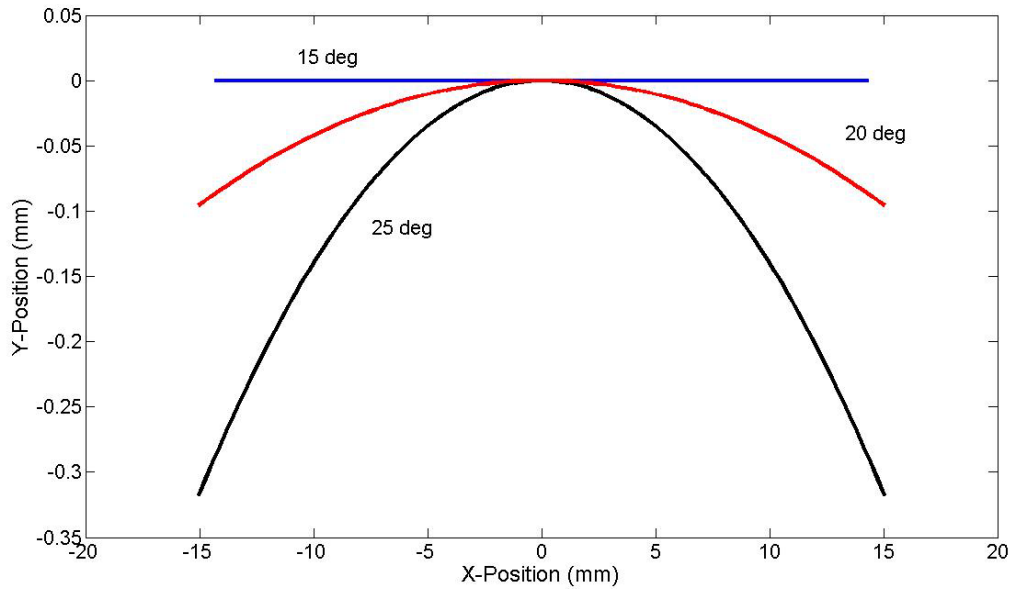


Figure 3.5. Simulated scan lines with varying angle of incidences

The combination of these two factors of pitch and incidence angle essentially means that the projected scan line for a particular wavelength will not be straight but might be bowed as the gratings scanner scans through  $\phi$ . There is an optimum condition between the grating pitch, incidence angles and the wavelengths currently being imaged. Amongst these few parameters, the grating pitch is perhaps the least flexible. It has to be determined at the onset of the grating design and fabrication process. The wavelength dependence is unavoidable since we are scanning through the spectrum. That leaves us with the variation of the incidence angle as the only parameter tunable during operation.

To achieve a bow-free scan for a particular wavelength, the incident and diffracted angles has to satisfy [17]

$$\sin \alpha = \frac{m\lambda}{\Lambda} - \frac{\Lambda}{m\lambda} \quad (16)$$

$$\sin \beta = \frac{\Lambda}{m\lambda} \quad (17)$$

This has important implications in the implementation of the spectral imager. Firstly, a linear array of detectors might not be a suitable candidate for sensing due to the bowing effect. The resultant spectral distribution from every spatial point as the grating scans through  $\phi$  has to be a straight line in order for all the dispersed spectral components to be incident on the linear array. It would not be feasible to compensate all of the angles to achieve bow-free of every wavelength continuously. As shown previously, given a grating pitch  $\Lambda$  and incident angle  $\alpha$ , only small spectral region will be accurately positioned to land on the linear array. An obvious alternative would be to use a 2-D array and calibrate the detection to synchronize with the grating rotation. This approach would be both expensive and computationally more intensive. Moreover, long wavelengths sensitive 2-D arrays may not be easily available.

A simpler mechanism would be to use two galvano mirrors to work in tandem to ensure that the incident and diffracted angle of the particular wavelength reaches a single photodetector as the grating scans. These mirrors need to traverse an angular trajectory determined by the equations for the particular wavelength to be measured. This would allow all wavelengths to be directed into the single photodetector sequentially. In this manner, the photodetector has to resolve the information reaching it temporally. Each wavelength bin has lower integration time than in the case of a full-field imager. The photodetector has to operate at a faster response time and higher-sensitivity.

Secondly, the scan length of a particular wavelength is not fixed. The scan length  $R'_x$  was earlier shown to be  $R'_x \approx -\frac{m\lambda}{\Lambda}l\phi$ .

The scan length is therefore changed in an approximate linear relationship with the wavelength. A comparison between the theoretical and approximation scan length with respect to scan angle is shown in Fig.3.6, which shows a good approximation to linearity. We assumed an incidence angle of  $25^\circ$ , varying wavelengths from 550nm to 700nm and a large grating rotational angle of  $15^\circ$  in order to see some noticeable non-linearity sets in.

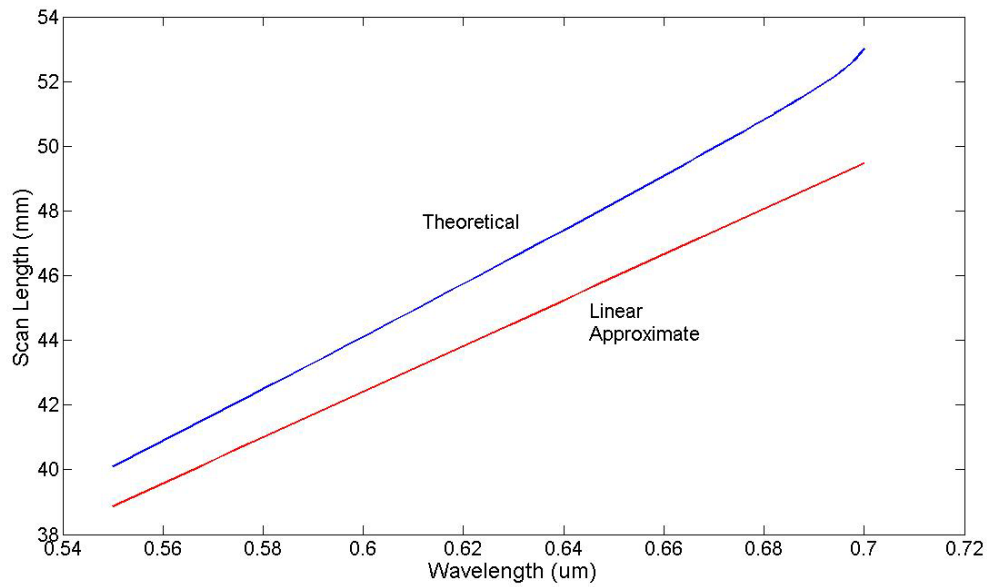


Figure 3.6. Graph showing the close approximation for the linear model

This implies that compensation is necessary to take the discrepancy into account. Two approaches are possible. One, through a feedback loop of the two galvano mirrors' position, we vary the scanning amplitude of the grating scanner to ensure that all spectral lines are scanned with equal scan length. Two, one can post-process the acquired data to compensate. This can be done by identifying the smallest scan length of the spectrum (typically the

smallest wavelength) and take that as the scan length that the spectral image should offer. Data points beyond this scan length for other wavelengths are discarded.

### 3.2. MEMS Grating Scanner Development

Earlier work in the group established the viability of high optical efficiency scanning. Optical efficiency of about 80% was theoretically predicted and experimentally verified. We were able to predict and design with a reasonable amount of certainty, a high efficiency binary grating scanner.

An early MEMS grating scanner had a grating platform diameter of 1 mm with a grating period of 500nm. The grating depth of 125nm was found to be optimal in its diffractive efficiency. This device has a resonance frequency at 20.347 kHz with a mechanical half rotation angle of 5.44 degrees when operated in air. At a wavelength 600 nm, this scanner is capable of scanning an optical full angle of 13.7 degrees.

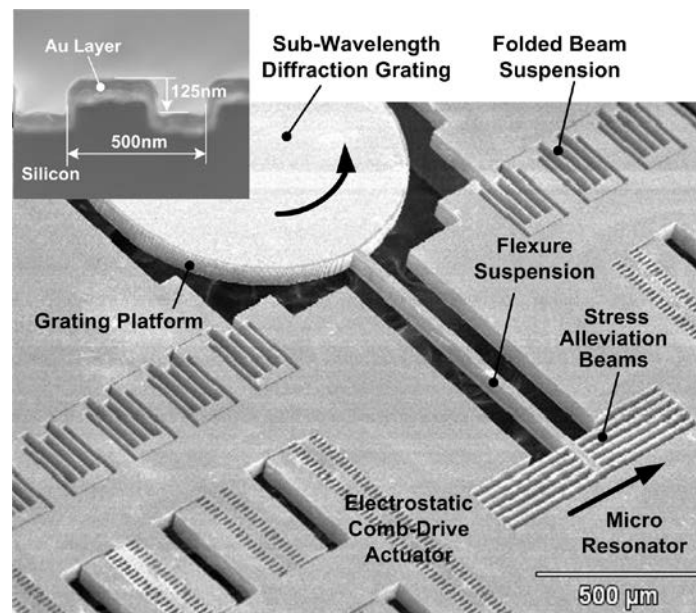


Figure 3.7. SEM image showing the MEMS grating scanner device with the inset showing the sectional profile of the fabricated gratings



The light collection ability lies in the aperture size of the scanning device. In this regard, a large aperture size is required for imaging systems such as spectral imagers. A single-layered grating scanner allows for simple fabrication processes of the device. However, further enhancements of the optical performance are constrained. Since the rotational angle of the grating platform is inversely proportional to the diameter of the diffraction grating when the maximum allowable deformation of platform suspension flexures is fixed, the aperture size and the optical scan angle cannot be increased simultaneously. In addition, increasing the diameter of the grating platform will increase its rotational inertia and the stiffness of the suspension flexures has to be increased by either widening or shortening the flexures to maintain the same scanning frequency. This will induce excessive stress inside the suspension flexures and reduce the scanning amplitude.

Double-layered vibratory grating scanner [29], where the grating platform and its driving actuator are located in different layers, is proposed to further improve optical performance instead. As shown in Fig.3.8, the grating platform is located in the top layer and connected to a connection platform through a round pillar at its center. The connection platform and driving actuator are located in a separate layer below the grating and are supported by several flexures. Under this configuration, the rotational angle of the grating platform is no longer determined by the size of the diffraction grating but by the diameter of the connection platform. Therefore, the size of the diffraction grating can be increased and the size of the connection platform reduced to minimum, thus increasing the aperture size and the scanning amplitude simultaneously. This configuration significantly boosts its optical resolution. Furthermore, the double-layered configuration allows the thickness of the grating platform and suspension flexures be independently designed.

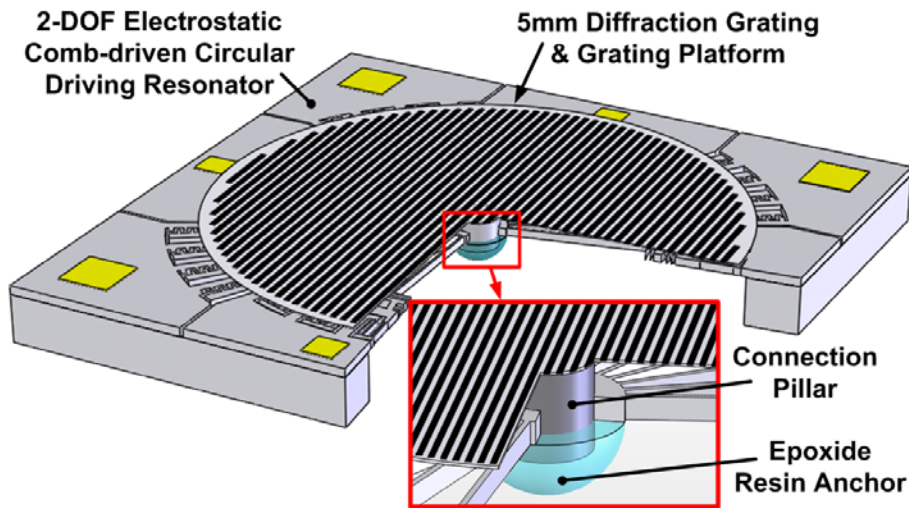


Figure 3.8. Schematic illustration of the assembled electrostatic double-layered vibratory grating scanner with a 5mm diameter grating platform.

Many different approaches are available to fabricate the electrostatic double-layered vibratory grating scanner, such as the multi-layer surface micromachining process [18], the wafer bonding process [19] and the post assembly process. We chose to use a combination of the bulk micromachining process and the post assembly process to fabricate the device, which not only reduces the complexities and difficulties of the device fabrication but enables enough flexibility to the device design. The grating platform, which has the diffraction grating on its top and the connection pillar on its back, and the driving actuator are designed and will be fabricated separately using the bulk micromachining process. They are assembled together by using a specially designed aligner and bonded together using epoxide resin.

The grating platform with the connection pillar is schematically shown in Fig.3.9. The diffraction grating, with a 500nm grating pitch and 5mm diameter, is patterned on the front side of the circular grating platform, which has a thickness of 20 $\mu\text{m}$ . The connection pillar is attached to the backside of the grating platform at its centre. Its radius and the thickness are 200 $\mu\text{m}$  and 300 $\mu\text{m}$  respectively.

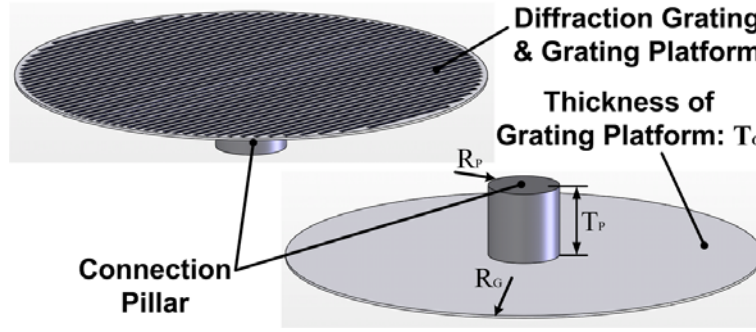


Figure 3.9. Schematic illustration of the grating platform with connection pillar.

The schematic illustration of the 2-DOF electrostatic comb-driven circular resonator, which acts as the driving actuator, is shown in Fig. 3.10. The circular connection platform, with the mounting hole at its centre, is connected to the outer comb-driven circular resonator through 28 single-beam flexures, each of them having two pairs of perpendicularly-connected stress alleviation beams. The radius of the connection platform and the mounting hole are  $270\mu\text{m}$  and  $200\mu\text{m}$  respectively. Among the 28 single-beam flexures, 14 are  $24\mu\text{m}$  wide and  $1280\mu\text{m}$  long and the rest,  $26\mu\text{m}$  wide and  $1480\mu\text{m}$  long. The outer circular resonator is suspended by 32 sets of circular folded beam suspensions with beams of width  $16\mu\text{m}$  and length  $350\mu\text{m}$ . Each stress alleviation beam has a width of  $6\mu\text{m}$  and length of  $255\mu\text{m}$ . There are 280 movable circular fingers for one-side driving with finger width  $7\mu\text{m}$ , finger gap  $5\mu\text{m}$  and initial finger overlap angle  $0.7^\circ$ . The thickness of all the structures in the driving actuator layer is  $150\mu\text{m}$ .

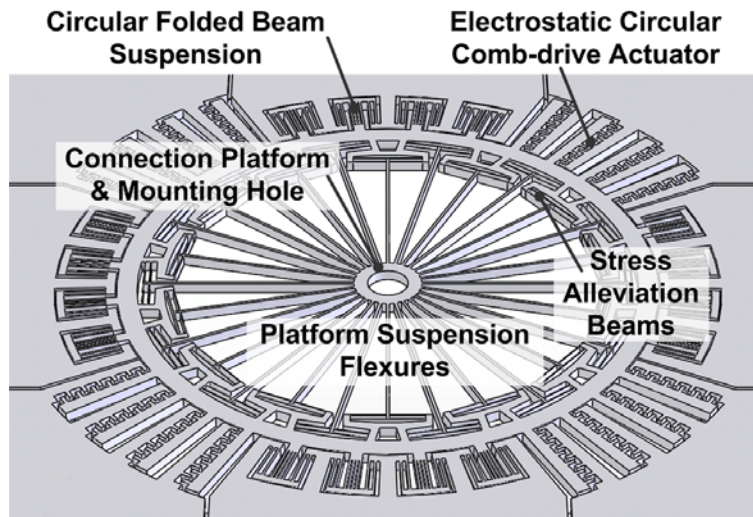


Figure 3.10. Schematic illustration of the 2-DOF electrostatic comb-driven circular resonator.

### 3.2.1. Fabrication process flow for grating platform and connection pillar

The diffraction grating, grating platform and connection pillar was fabricated using bulk silicon micromachining technology with a total of four photo masks used. Normal silicon wafers with a thickness of 750 $\mu\text{m}$  was used in the fabrication process. Fig.3.11. shows a schematic of the fabrication process flow. With reference to Fig.3.11, a 200nm low-pressure chemical vapor deposition (LPCVD) silicon nitride layer is first deposited on both sides of the wafer. The top layer is removed by a reactive ion etching (RIE). Next, the diffraction grating (mask layer L1) with a 500nm grating period and 50% duty cycle is patterned using deep-UV lithography and etched using timed plasma etching. The grating groove depth will be controlled to achieve maximum efficiency. Next, the grating platform (mask layer L2) is formed by using a timed deep reactive ion etching (DRIE) process, of which the etching depth is controlled to be 10 $\mu\text{m}$ . This defines the thickness of the grating platform and serves as an etching stop mark for the following process. Then LPCVD silicon nitride layer on the backside of the SOI wafer, which served as the hard mask for the following wet-etching process, is patterned using RIE (mask layer L3). Subsequently, a 550 $\mu\text{m}$ -deep square cavity, which thins down the silicon substrate to 200 $\mu\text{m}$ , is formed by

wet anisotropic Si etch in KOH solution (35 wt%, 75°C). After that, a 1 $\mu$ m plasma-enhanced chemical vapor deposition (PECVD) un-doped silicon glass (USG) layer is deposited onto the wafer's backside and the bottom of the etched cavity and patterned using RIE process (mask layer L4). Finally, the connection pillar is formed and the grating platform is released by another timed DRIE process (around 200 $\mu$ m) which stopped when trenches formed by the previous DRIE process are fully exposed. The thickness of the grating platform are controlled by the 1<sup>st</sup> timed DRIE etching and the thickness of the connection pillar is defined by the depth of the backside cavity, formed by wet anisotropic Si etch which has excellent etching uniformity.

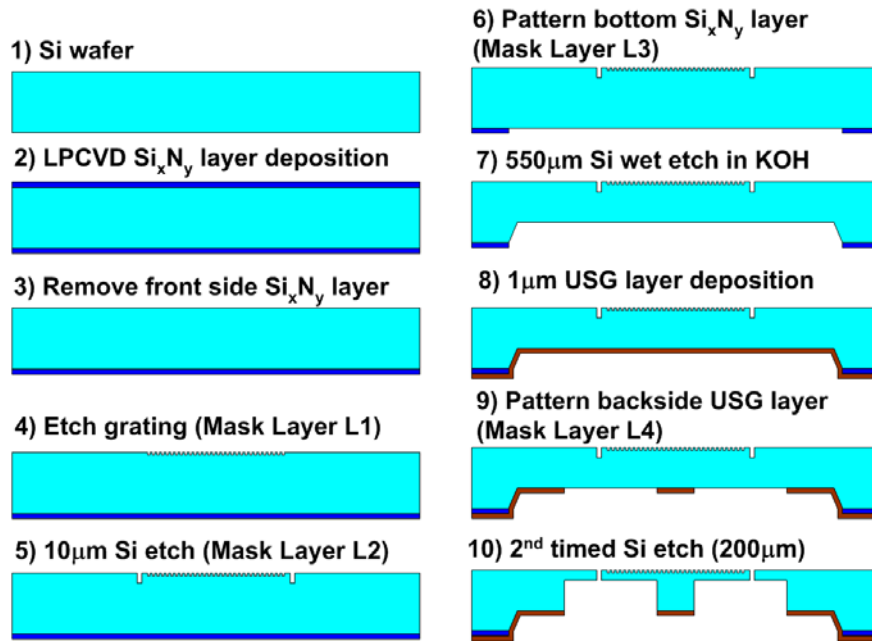


Figure 3.11. Fabrication process flow for the diffraction grating, grating platform and connection pillar.

### 3.2.2. Fabrication process flow for 2-DOF electrostatic comb-driven circular resonator

The 2-DOF electrostatic comb-driven circular resonator is fabricated using SOI micromachining technology; three photo masks were used in this process. The SOI wafer has a 150- $\mu$ m-thick heavily doped silicon device layer, a 2- $\mu$ m-thick buried oxide (BOX) layer

and a 600- $\mu\text{m}$ -thick silicon substrate. The fabrication process flow is illustrated in Fig.3.12. As shown in Fig.3.12, a 1 $\mu\text{m}$  PECVD USG layer is first deposited onto the SOI wafer's front side and patterned by using a RIE process (mask layer L1). It is subsequently used as the hard mask for the following DRIE etching process. The SOI wafer is patterned on its backside (mask layer L2) and the 600- $\mu\text{m}$ -thick silicon substrate was etched through by a following DRIE process to expose the region encompassing all the structures. The BOX layer is used as a stop layer for the DRIE etching process. Next, the 150- $\mu\text{m}$ -thick silicon device layer is etched through from the wafer's front side by another DRIE process, which is also stopped at the BOX layer. After this step, the connection platform with a mounting hole, the circular comb-drive actuator and suspension flexures are formed. The USG layer on the wafer's front side and the exposed BOX layer are etched away in BOE solution so that all the structures formed in the silicon device layer are released. Finally, the metal pads for wire bonding are formed by evaporating 1000 Å/5000 Å thick Ti/Au layer through a shadow mask (mask layer L3).

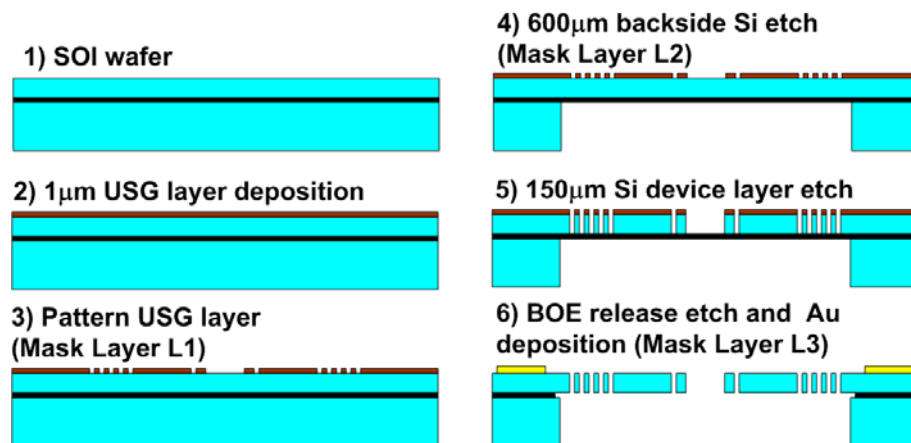


Figure.3.12. Fabrication process flow for the 2-DOF electrostatic comb-driven circular resonator.

### 3.2.3. Post-assembly process

The grating platform and the 2-DOF electrostatic comb-driven circular resonator was assembled by a post-fabrication process to form the double-layered vibratory grating scanner.

The schematic illustration of the post assembly process is shown in Fig.3.13.

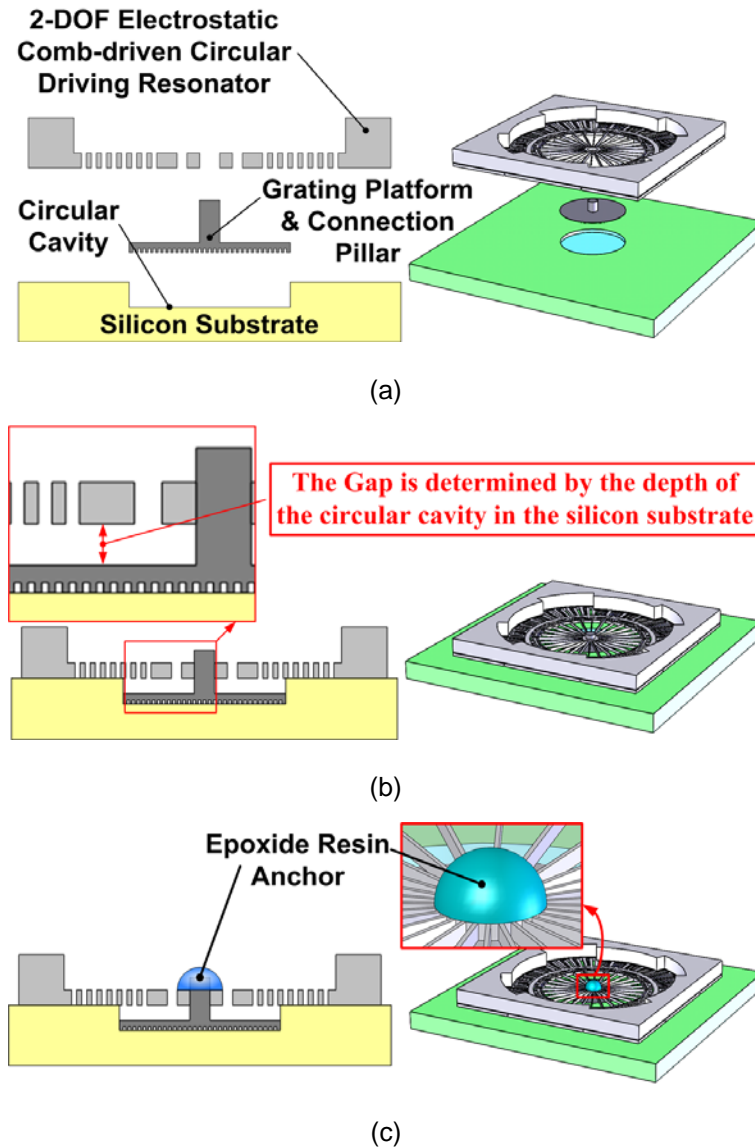


Figure 3.13. Schematic illustration of the post-assembly process.

As shown in Fig.3.13(a), both the grating platform and 2-DOF electrostatic comb-driven circular resonator are turned upside down before assembly. A silicon substrate with a circular cavity located at its centre, which is used as a mold during the manual assembly process, is designed and fabricated using the bulk micromachining process. The circular

cavity having diameter 5050 $\mu\text{m}$  and depth 100 $\mu\text{m}$  is formed by a timed DRIE process, ensuring that the bottom of the cavity is parallel to the surface of the substrate. Then the grating platform is placed inside the circular cavity in the fixed silicon substrate and the driving resonator is held by a gripper attached to a 3-axes precision positioner. The 2-DOF circular resonator is then aligned under a microscope so that the mounting hole and the connection pillar were concentric. Next, the 2-DOF circular resonator is pressed tightly until it contacts the surface of the fixed silicon substrate. Meanwhile, the connection pillar is inserted into the mounting hole, as shown in Fig.3.13(b). The gap between the grating platform and the 2-DOF circular resonator is determined by the depth of the circular cavity in the silicon substrate. The parallelism between the diffraction grating and its driving actuator is ensured by the accuracy of the fabricated silicon substrate. Finally, the connection pillar and the connection platform were bonded together by Epoxy Adhesive (as shown in Fig.3.13 (c)) and cured in oven to achieve full strength.

Microscope images of the whole and the part view of the assembled double-layered vibratory grating scanner are shown in Fig.3.14 (a) & (b) respectively. The assembled device was glued on a printed circuit board (PCB) substrate with all the electrodes wire bonded. Fig. 3.15. shows a photograph of the assembled double-layered vibratory grating scanner on a PCB substrate.



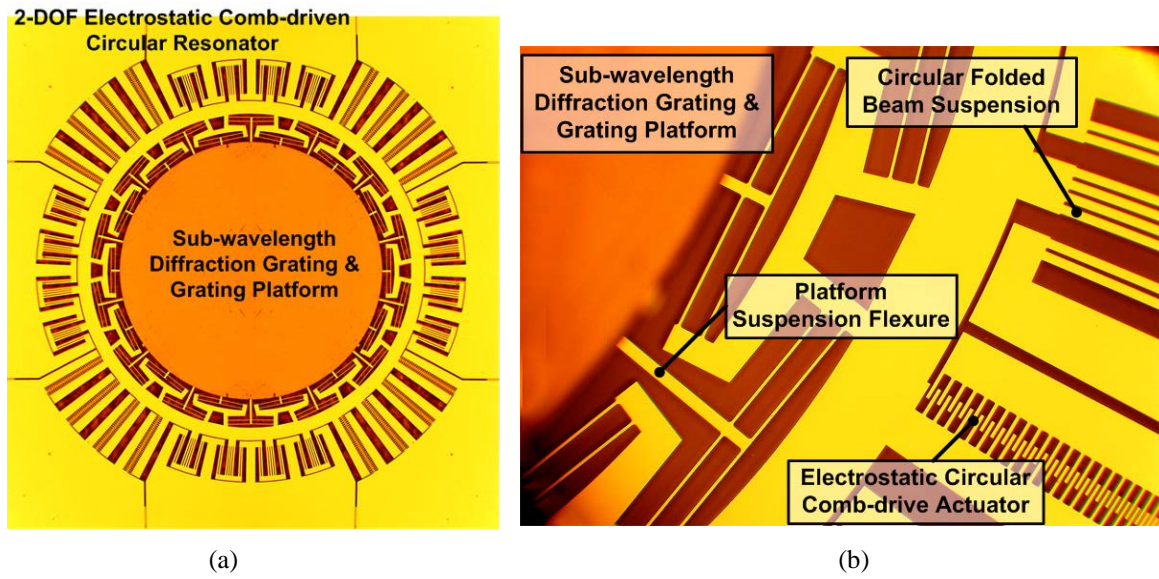


Figure 3.14. Microscope image showing the (a) whole view (b) part view of the assembled double-layered vibrating grating scanner with a 3mm diameter grating platform.

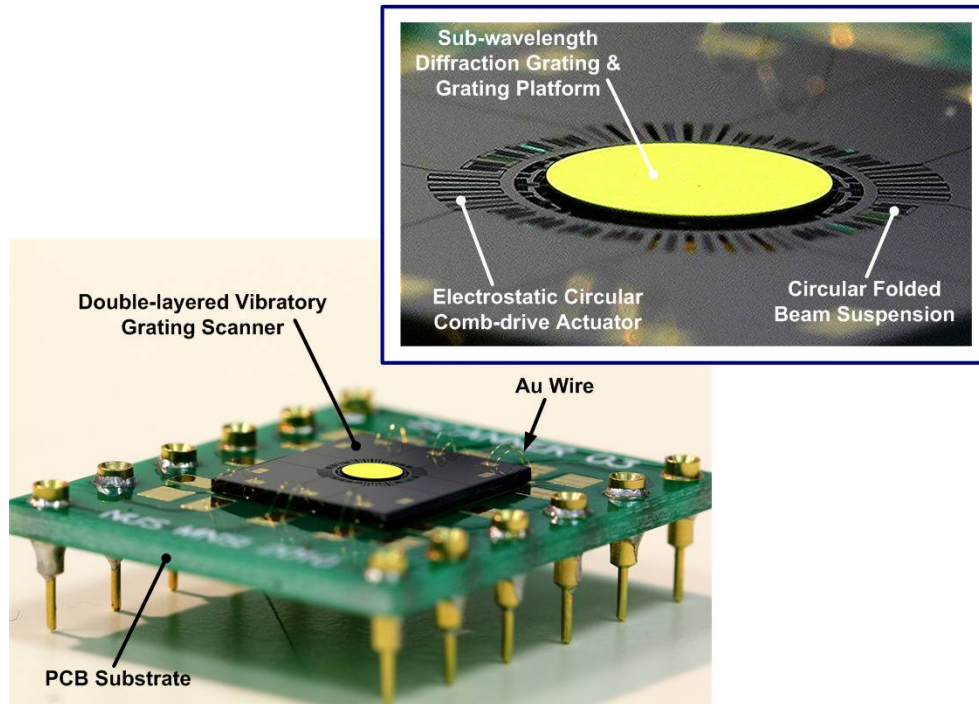


Figure. 3.15. Photographic image showing the assembled double-layered vibratory grating scanner on a PCB substrate.

The performance of the prototype electrostatic double-layered vibratory grating scanner was tested using a linearly TM-polarized He-Ne laser beam with a wavelength of 632.8 nm and the experimental setup is schematically illustrated in Fig.3.16. Since the grating pitch of the adopted diffraction grating is 400 nm, the incident angle of the illuminated laser

beam was determined to be  $71.8^\circ$  so that the bow-free scanning conditions are fulfilled.

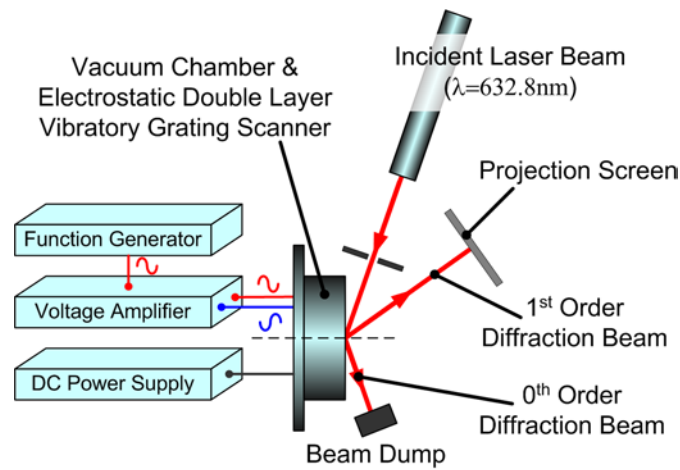


Figure. 3.16. Schematic illustration of the experimental setup for the prototype double-layered vibratory grating scanner.

The dynamic performance of the prototype electrostatic double-layered vibratory grating scanner was tested in a vacuum environment (1.2 mTorr). The circular comb-drive resonator was driven by a push-pull mechanism with a DC bias and an AC signal following a sinusoidal pattern. The optical scan angle was determined by measuring the length of the laser scanning trajectory on a projection screen. The projection screen was aligned perpendicular to the 1<sup>st</sup> order diffracted laser beam when the diffraction grating remained motionless. The frequency response of the prototype scanner was obtained by sweeping the frequencies of the driving signal. As expected, the double-layered vibratory grating scanner has two resonating modes. The resonant frequencies of the first and the second resonating modes were determined to be around 22.987 kHz and 34.941 kHz. The driving voltages were fixed at 5 V dc bias and 10 V ac peak-to-peak voltages to avoid the shift of resonant frequencies due to large deflection nonlinearities.

## 4. Hyperspectral Imaging in Double Galvano-Mirror Configuration

### 4.1. Configuration Overview

All spectral imaging systems employed require some form of post signal processing to reconstruct the spectral image. For pushbroom and whiskbroom configurations, this includes calibration compensating the intensity response function for the individual detectors in the arrays.

There are two main considerations for the gratings scanner based system to reconstruct the spectral image. First, as mentioned earlier, the spatial scan length of each wavelength varies according to the equation (15) which is the keystone artefact. Secondly, the oscillatory spatial scanning of the grating scanner results in pixel spatial placement errors on spacing non-uniformity if the sampling of the intensity points cannot be variably controlled. Conceptually, both aberrations can be compensated real-time in the system through various elegant means.

We have to recognize that the sinusoidal vibratory motion results in the sampled data having varying spatial location. Keeping in mind that the sampling was done at a constant rate, it is elementary to work out the actual spatial location of the intensity data for a given wavelength as scanning was performed.

It is also obvious that the length of the scan of a particular wavelength is linearly proportional to the wavelength currently being detected. This is also commonly known as keystone. This results in errors in assuming during image reconstruction the phase of the grating oscillation corresponds to the same spatial location for all wavelengths. The largest

image is therefore dependent on the shortest scan length possible. We can then remove the extraneous lengths of longer wavelengths to reconstruct the spectral image. To further reconstruct the image, the actual spatial location of the sampled data can be determined through a theoretical model. With the two galvano-mirrors performing the bow-free spectral scan, the spectral accuracy of the data points is ensured. To obtain a spatially-undistorted image, we interpolate the two spatially nearest intensities of each desired Cartesian pixel location.

To achieve even better optical performance, more detailed compensations are necessary. For example, the ideal bow-free scan profile is actually not a perfect straight line. Some small perturbations in the scan profile still occur. However these effects can largely be assumed to be negligible at low resolution requirements.

Secondly, as we are scanning through the image plane, pixel-to-pixel spectral mixings [12] do occur. Similarly, relative motion between pixels results in distorted or warped images. However, both aberrations are assumed negligible if we are able to scan at high frequencies as per our grating scanner.

## **4.2. Optical Model**

Prior to the conceptualization of the optical model, it is necessary to understand the characteristics and limitations of the scanning mechanism. To minimize cost and simplify the configuration, a single-pixel detector is used. Fig.4.1. shows the schematic of our optical model.

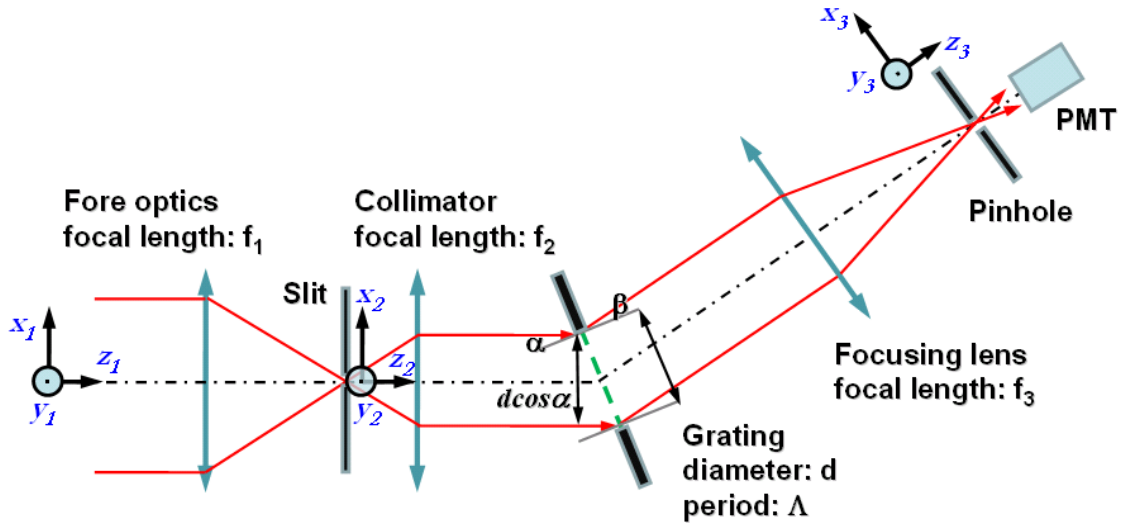


Figure 4.1. Schematic illustration showing the simplified model of the proposed hyperspectral imager

The focal lengths of the fore optics, collimating and focusing lenses are  $f_1$ ,  $f_2$  and  $f_3$ , respectively. The incident and diffraction angle of the diffraction grating are  $\alpha$  and  $\beta$  respectively. The grating diameter and grating period are denoted by  $d$  and  $\Lambda$ . The size of the ground area viewed by the detector are  $dx_1$  (along x axis) and  $dy_1$  (along y axis). The ground area is then imaged by the fore optics and the size of the image are  $dx_2$  (along x axis) and  $dy_2$  (along y axis). The shape of the pinhole is assumed to be a rectangle and the lengths along  $x_3$  axis and  $y_3$  axis are  $dx_3$  and  $dy_3$ .

In the system, the size of the light beam entering the imager will be limited by the size of the diffraction grating. Hence it is clear that the entry pupil will be an ellipse and its size is determined by the size of the diffraction grating. For conservative estimation, we use its minor diameter:

$$D_{mi} = \frac{f_1 d \cos \alpha}{f_2} \quad (18)$$

Eq. (19) shows the well-known grating equation [17]:

$$\Lambda \cos \theta (\sin \alpha + \sin \beta) = \lambda \quad (19)$$

where  $\phi$  is the field angle relative to the diffraction grating.

As can be seen from the grating equation, the diffracted beam's angle is affected by several factors including the incident angle, wavelength and the field angle of the grating. To simplify our analysis, we consider a case whereby the grating remains at rest. We will approach the more complex case of considering the variation of all the parameters later.

To estimate the ground area viewed by the detector at a fixed wavelength, we first set  $\phi = 0$  (at the middle of the field) and differentiate both sides of the equation:

$$\Lambda (\sin \alpha + \sin \beta) = \lambda$$

$$\Lambda (\cos \alpha d\alpha + \cos \beta d\beta) = 0$$

$$\frac{d\alpha}{d\beta} = -\frac{\cos \beta}{\cos \alpha} \quad (20)$$

Knowing  $f_2 d\alpha = dx_2$  and  $f_3 d\beta = dx_3$ , we obtain

$$\frac{dx_2}{dx_3} = -\frac{f_2 \cos \beta}{f_3 \cos \alpha} \quad (21)$$

Next, we examine the case where  $\phi$  is varied with a small amount closed to zero while fixing  $\alpha$  and  $\beta$ . We can obtain  $f_2 d\phi = -dy_2$  and  $f_3 d\phi = dy_3$

$$\frac{dy_2}{dy_3} = -\frac{f_2}{f_3} \quad (22)$$

Combining, we obtain

$$dx_2 dy_2 = \left( \frac{f_2}{f_3} \right)^2 \frac{\cos \beta}{\cos \alpha} dx_3 dy_3 = \left( \frac{f_2}{f_3} \right)^2 \frac{\cos \beta}{\cos \alpha} A_{pixel} \quad (23)$$

The area on the ground viewed by the detector can then be approximated by:

$$\frac{dx_1}{L_o} = \frac{dx_2}{f_1}$$

$$\Rightarrow dx_1 = -\frac{L_o}{f_1} dx_2 \quad (24)$$

$$\text{Similarly } \Rightarrow dy_1 = -\frac{L_o}{f_1} dy_2 \quad (25)$$

$$dx_1 dy_1 = \left( \frac{L_o}{f_1} \right)^2 dx_2 dy_2 = \left( \frac{L_o f_2}{f_1 f_3} \right)^2 \frac{\cos \beta}{\cos \alpha} A_{pixel} \quad (26)$$

#### 4.2.1. Spectral Resolution

Now, consider the system's spectral resolution at the middle of the field of view ( $\phi = 0$ ).

$$\Lambda(\sin \alpha + \sin \beta) = \lambda \quad (27)$$

According to the grating equation Eq.(27), we keep the angle  $\alpha$  fixed and differentiate both sides of the equation:

$$\Lambda d\beta \cos \beta = d\lambda \quad (28)$$

Since  $f_3 d\beta = dx_3$ ,

$$d\lambda = \Lambda \frac{dx_3}{f_3} \cos \beta$$

$$\Delta \lambda = \frac{\Lambda}{f_3} \cos \beta \Delta x_3 \quad (29)$$

Thus, the spectral band that is allowed to pass through the slit  $x_3$  changes according to the diffractive angle. The spectral resolution then depends on the actual spectral range the system is designed for.

#### 4.2.2. Spatial Resolution

Now we consider the ground resolution, from Eq. (25) and (22), we can obtain:

$$\begin{aligned} dy_1 &= \frac{L_o}{f_1} \frac{f_2}{f_3} dy_3 \\ &= \frac{L_o}{f_1} \frac{f_2}{\Lambda \cos \beta} \frac{d\lambda}{dx_3} dy_3 \end{aligned} \quad (30)$$

Assuming the grating scanner has an optical scan angle of  $\phi_{opt}$ , the number of the spatial pixels can be calculated as:

$$\begin{aligned} N_{spatial} &= \frac{L_o FOV}{dy_1} \\ &= \frac{L_o}{dy_1} \frac{f_2 \phi_{opt}}{f_1} = \frac{\Lambda \phi_{opt} \cos \beta}{d\lambda \left( \frac{dy_3}{dx_3} \right)} \end{aligned} \quad (31)$$

From Eq. (31), we can see that the spatial resolution is also independent of focal lengths  $f_1$ ,  $f_2$  and  $f_3$ . It is proportional to the optical scan angle, grating period and inversely proportional to the spectral resolution and  $dy_3/dx_3$ . Increasing grating period and decreasing of  $dy_3/dx_3$  will increase the spatial resolution but the light intensity will be decreased.



### 4.2.3. Theoretical Limits

The previous equations only estimate the optical performance at  $\phi = 0$ . To determine the overall system resolution limits, by considering all parameters, we chose a computational approach.

A ray-tracing method using the grating equations was employed to model the system performance of the hyperspectral imaging system. The model should provide a reference relating to the spatial resolution, spectral resolution, etc, that we would expect.

We first determine the effect the size of the pin-hole has on the performance of the system. To present generalized results here, instead of specifying the wavelength  $\lambda$  and the grating period  $\Lambda$ , we use the normalized wavelength  $\lambda/\Lambda$ . The model the algorithm is based on is shown in Fig.4.2.

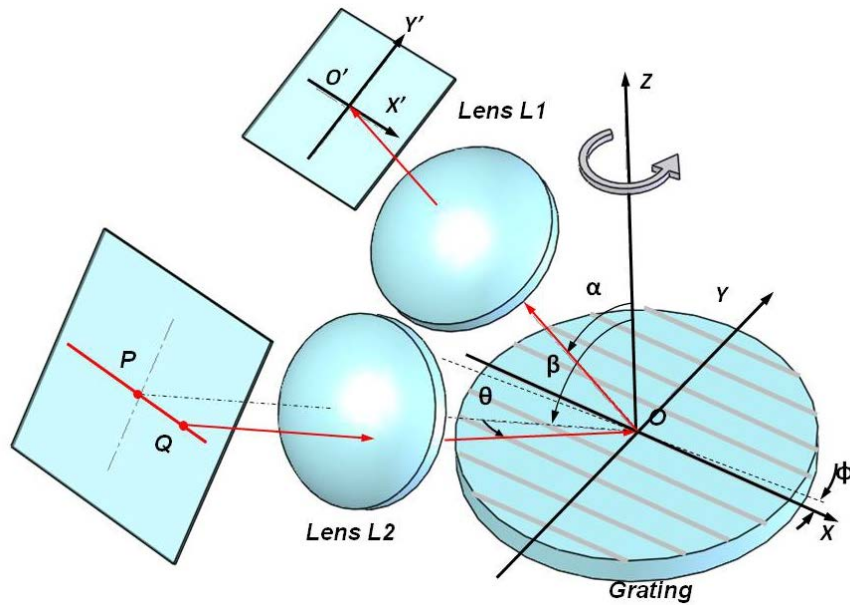


Figure 4.2. Schematic showing the parameters involved in the algorithm

The algorithm to determine the pin-hole effect is as follows:

- Determine the angles  $\alpha$  and  $\beta$  respectively using Eqs. (16) and (17) at a given normalized wavelength  $\lambda/\Lambda$
- Calculate the required grating in-plane rotation angle  $\phi$  such that the light of this wavelength incident from a chosen field angle  $\theta$  upon the grating can be diffracted and focused to the point  $O'$  in the focal plane of the lens L1. This is done by recognizing that in order for all beams of light to reach the photodetector,  $k_x^m = 0$ , i.e. from (7)

$$m \frac{2\pi}{\Lambda} \sin \phi = \left( \frac{2\pi}{\lambda} \right) \sin \theta \quad (32)$$

This effectively provides the rotational angle of the grating necessary to get the incident beam from the image plane to be directed onto the photodetector. The  $\phi$  angle necessary was already calculated at the previous step.

- Now keeping the grating line orientation  $\phi$  and the normalized wavelength  $\lambda/\Lambda$  fixed, we investigate the slope angle of the diffracted light  $\gamma$ , defined as the angle that the out-going diffracted ray makes with the optical axis  $OO'$ , as a function of a small variation in the field angle  $\delta\theta$
- We further determine the ratio  $\gamma/\delta\theta$  at each field angle and normalized wavelength. Typical results are plotted in Fig.4.3, where  $\delta\theta$  is set at 0.05 degree and the maximum field angle  $\theta$  is assumed to be 15 degrees.

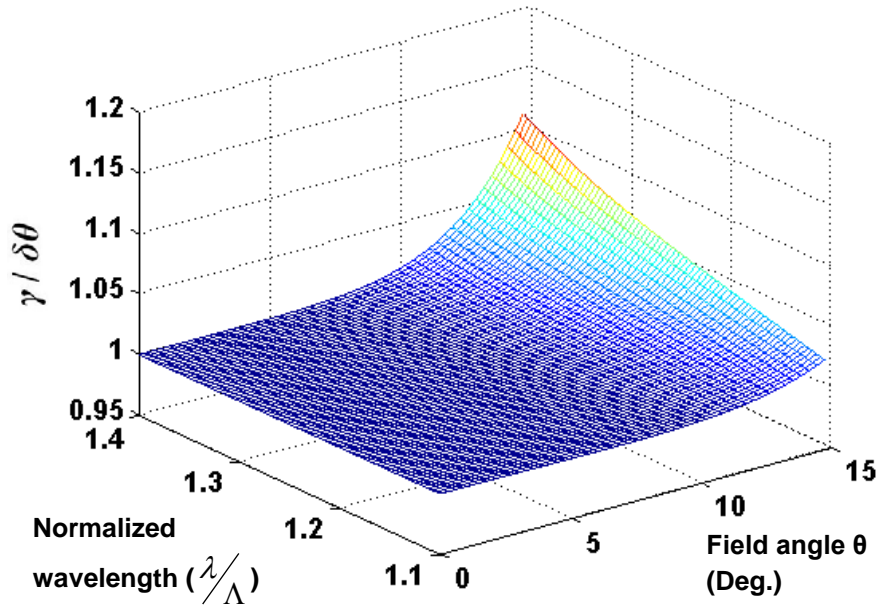


Figure 4.3. Graph showing ratio  $\gamma/\delta\theta$  with varying normalized wavelengths and field angles

We observed that the ratio  $\gamma/\delta\theta$  is close to 1 for all wavelengths and fields in the operational range. This can be utilized to estimate the spatial resolution of the system. For instance, given a lens L1 with a focal length of  $f$  and a pinhole with a diameter of  $D$  located in the lens' focal plane and centered at  $O'$ , we can determine the maximum slope angle of the diffracted light rays that are allowed to pass through the pinhole, i.e.

$$\gamma_{\max} = \tan^{-1}(D/2f). \quad (33)$$

Hence, the angular extent of the field angles from which the incident light can be collected by the detector is roughly  $2\gamma_{\max}$ , at a given instant of time. The spatial resolution can then be estimated accordingly.

A similar method can be used to determine the spectral resolution of the system. At each normalized wavelength  $\lambda/\Lambda$  and field angle  $\theta$ , we keep the grating line orientation  $\phi$  and field angle  $\theta$  fixed and investigate the slope angle  $\gamma$  of the diffracted light as a function of a small variation in the normalized wavelength  $\delta(\lambda/\Lambda)$ . Typical results showing the ratio

$\gamma/\delta(\lambda/\Lambda)$  as a function of field angle and normalized wavelength is plotted in Fig.4.4, where  $\delta(\lambda/\Lambda)$  is set at 0.002 in our calculations. We note that the minimum value of the ratio  $\gamma/\delta(\lambda/\Lambda)$  is close to 57 degrees or 1 radian over the operational range. We can then conservatively estimate the spectral resolution of the hyperspectral imaging system to be

$$\delta\lambda_{\max} = 2\gamma_{\max}d = 2\tan^{-1}(D/2f)d. \quad (34)$$

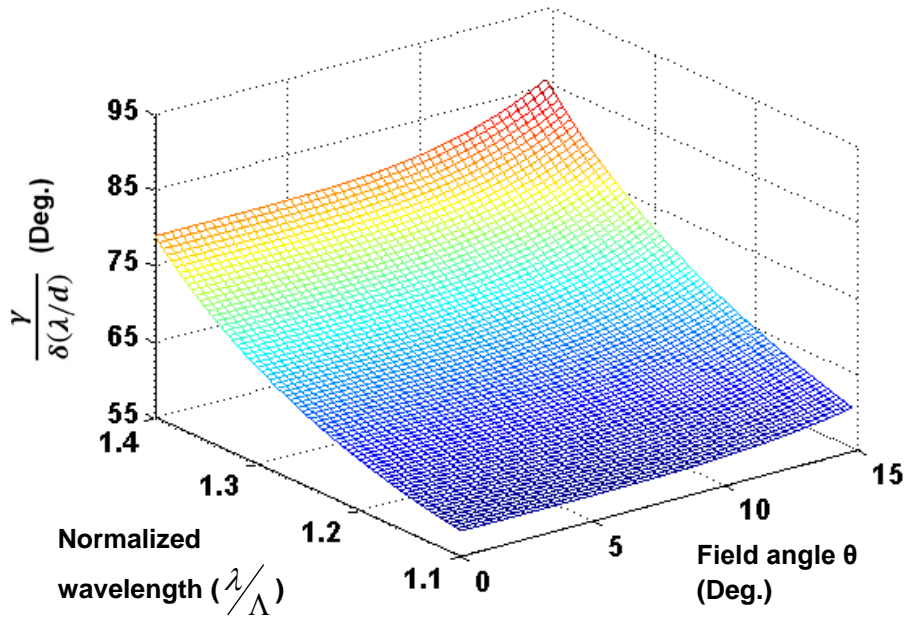


Figure 4.4. Graph showing ratio  $\gamma/\delta(\lambda/\Lambda)$  with varying normalized wavelengths and field angles

### 4.3. Correction of Distortion

Due to the nature of having a diffraction grating, the scanning trajectory will be bow-like (smile distortion) and the scanning amplitude will vary with the wavelength (spectral keystone distortion). Fig.4.5. shows the simulated scanning trajectory when the wavelengths are 450nm and 850nm, respectively.

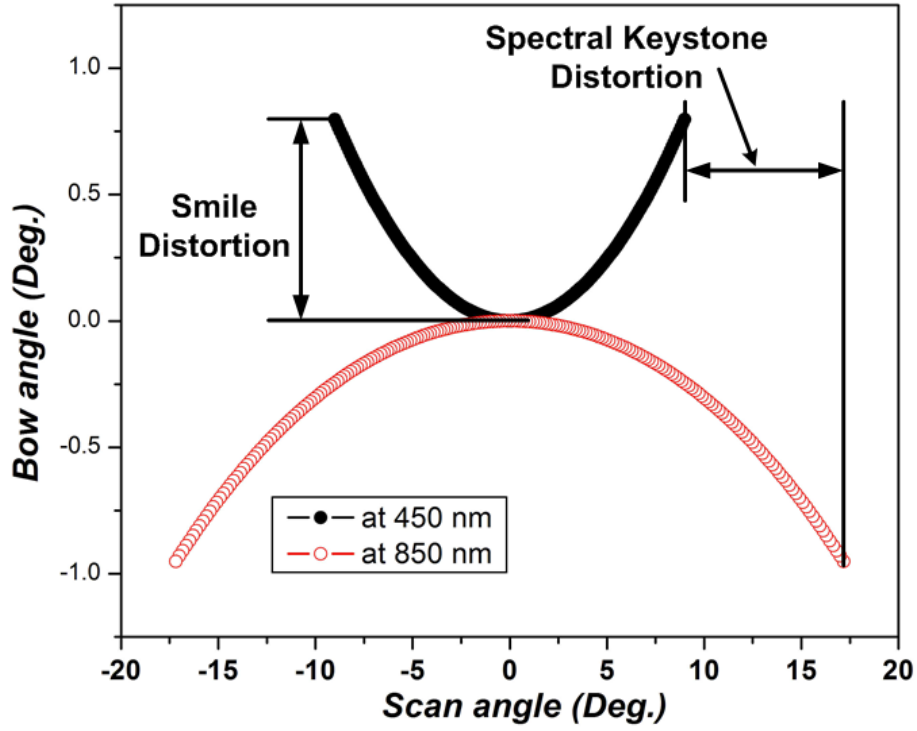


Figure 4.5. Schematic illustration showing the “smile” and spectral keystone distortions.

The “smile” distortion can be corrected through adjusting the diffraction angle  $\beta$  using a scanning mirror synchronized in accordance to the bow-free scanning condition described earlier in Eq. (16) and (17). Figs.4.6.(a) & (b) show the simulated scan bow before and after correction for wavelengths of 450nm and 850nm respectively. The simulation results show that the “smile” distortion can be effectively minimized to a negligible level.

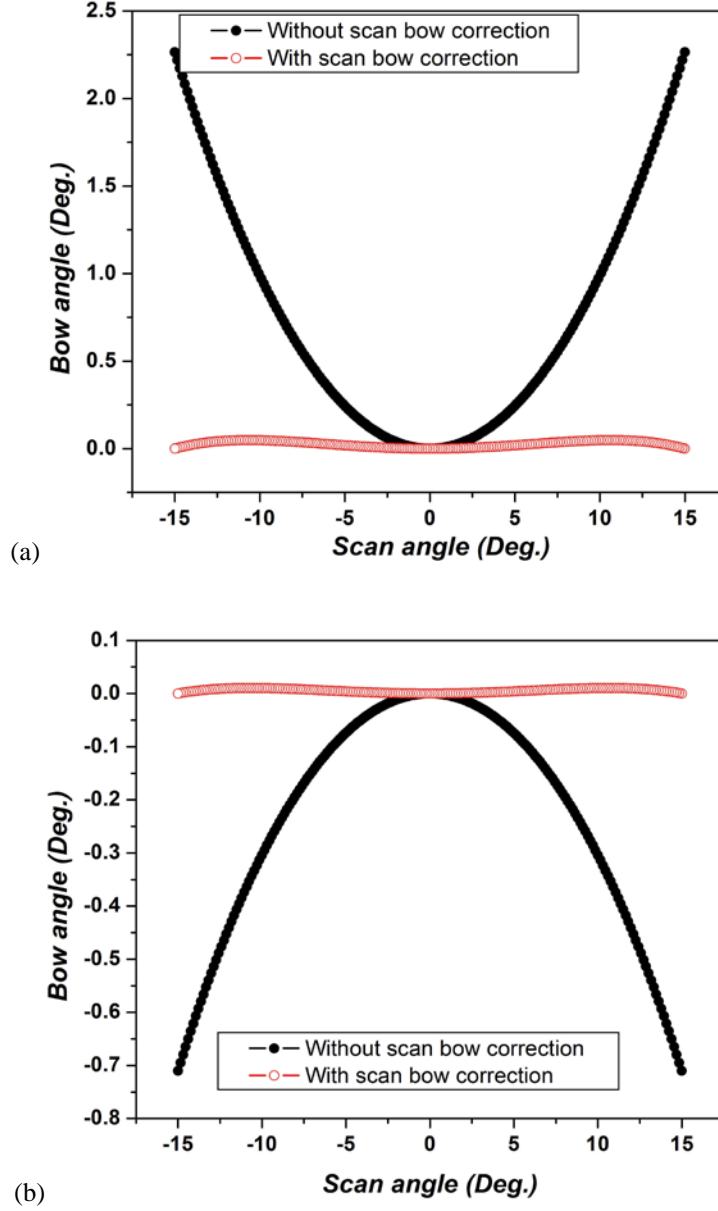


Figure 4.6 Simulated scan bow before and after correction with wavelengths of (a) 450nm and (b) 850nm respectively.

The keystone distortion is a result of a difference in scan length for various wavelengths. We considered two possible approaches to correct this aberration.

Firstly, one way of correcting is by modulating the in-plane rotation angle of the grating platform according to the wavelength. By predicting the actual optical scan length for various wavelengths, the driving amplitude to the grating scanner can be adjusted to achieve

the necessary scanning amplitude at each particular wavelength. Fig.4.7. shows a simulated relationship between the grating rotation angle and the wavelengths to correct the spectral keystone distortions.

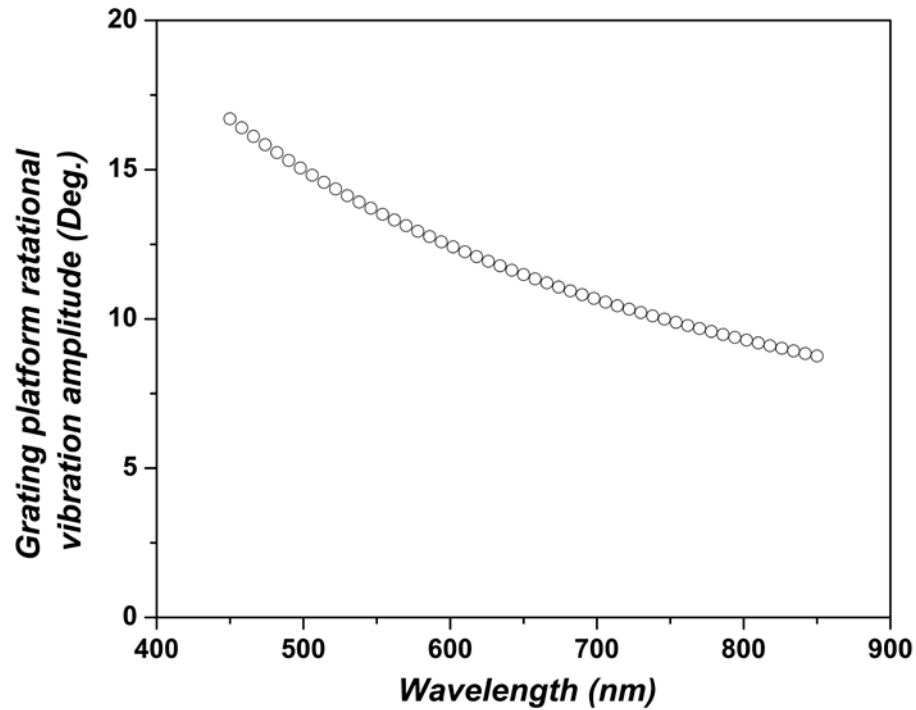


Figure 4.7. Simulated relationship between the rotation angle and the wavelengths to correct the spectral keystone distortions.

Fig.4.8. shows the simulated scan bow at different wavelengths after corrections of the “smile” and spectral keystone distortions. It is obvious that both “smile” and spectral keystone distortions can be minimized to a negligible level using the proposed driving scheme.

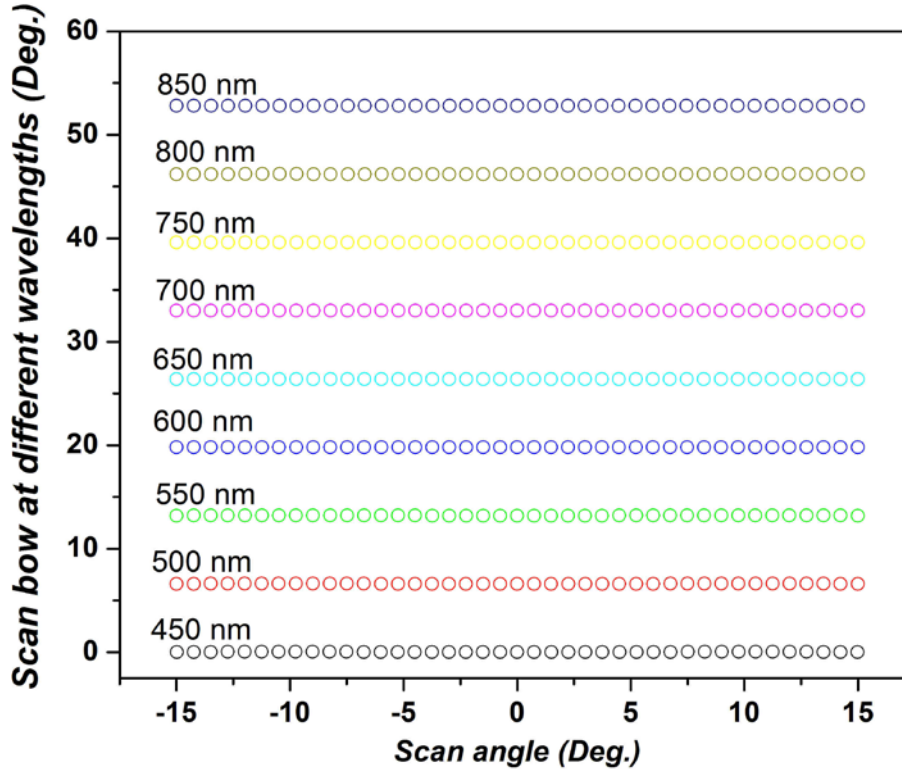


Figure 4.8. Simulated scan bow at different wavelengths after corrections of the “smile” and spectral keystone distortions.

This approach, while viable, imposes significant requirements in the synchronization and control of the driving schemes.

A potential issue with keystone distortion is that, together with the sinusoidal oscillatory nature of the gratings’ spatial scanning, the data points in the center of the field of view risks being undersampled. This may result in inaccuracies in intensities of the post-processed spectral map. Such an issue will not arise if oversampling is performed. The second approach that was considered was thus oversampling the data points. This would require a faster detector and DAC than theoretically required. However, detectors and DAC are typically faster than what is actually required in the system. The other downside will be a lost of data points that are not used at spatial locations beyond the scan length of the shortest wavelength. This is the approach we adopt in the subsequent systems.



The resulting setup requires a high-speed scanning mechanism, which the grating scanner fulfills. Two galvano mirrors are used to steer the incident and reflected beam angles of the grating scanner, thereby determining which dispersed wavelength reaches the photodetector. A pin-hole is placed before the detector to select the wavelength that enters the detector. A single-point highspeed avalanche photodiode detects the intensity of the resultant beam. The two galvano mirrors have to traverse synchronized through a predetermined angular relationship governed by the dispersion characteristics of the binary grating. Thus the grating scanner performs the spatial scanning while the galvano mirrors perform spectral scanning. Due to the nature of the high-speed grating scanner, the spatial scanning is performed at a much higher frequency than the spectral scanning of the galvano-mirror. The resultant data collected are sequential spatial information of specific wavelengths. The optical configuration is shown in Fig.4.9.

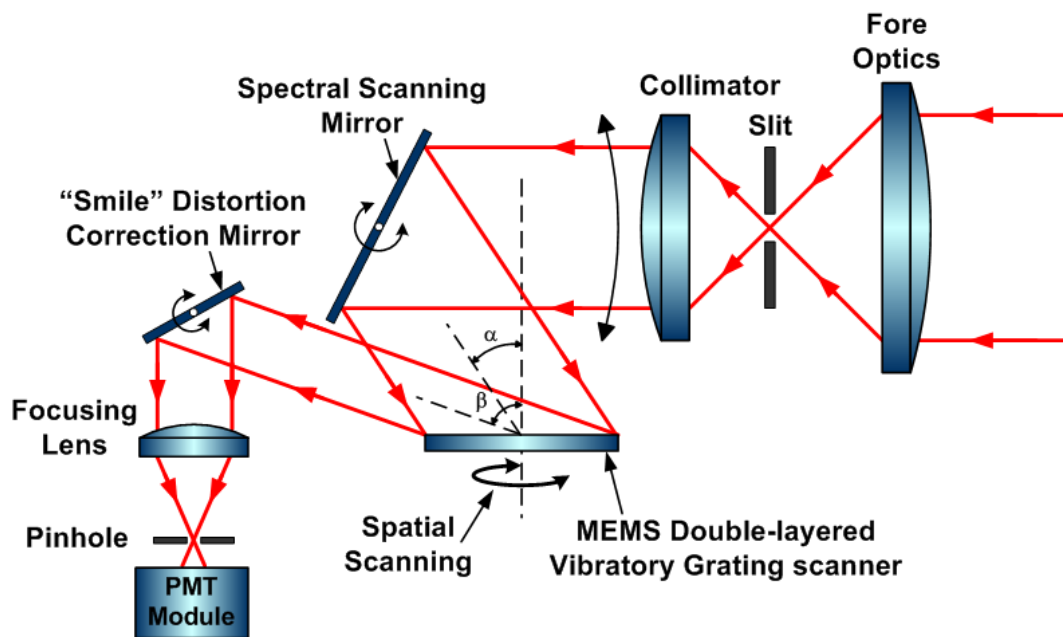


Figure 4.9. Schematic of a miniature double galvano-mirror hyperspectral imager with MEMS vibratory grating scanner.

For the spectral discrimination, if the angles  $\alpha$  and  $\beta$  satisfy respectively the

equations(16) and (17) for bow-free spectral scanning, only light of wavelength  $\lambda$  from a specific location along the slit (depending on the orientation of the grating lines) can pass through the pinhole and reach the detector.

#### 4.4. Post Signal Processing

There are two main considerations for the gratings scanner based system to reconstruct the spectral image. Firstly, the spatial scan length of each wavelength can be proven to vary approximately with the equation (15) described earlier

$$R'_x \approx \left( -\frac{m\lambda}{\Lambda} l \phi \right)$$

where  $R'_x$  = scan length,  $m$  = diffraction order,  $l$  = distance of projection from grating scanner, and  $\phi$  = grating rotation angle. It is obvious that the length of the scan of a particular wavelength is linearly proportional to the wavelength currently being detected. This is also commonly known as keystone. This result in errors in assuming during image reconstruction the phase of the grating oscillation corresponds to the same spatial location for all wavelengths.

Secondly, the oscillatory spatial scanning of the grating scanner results in pixel placement errors. As the sampling of the photodetector signals are at a constant rate, the actual spatial location of the sampled data will vary in a sinusoidal relation. More data points will be sampled at the end of the image line than at the center.

Conceptually, both aberrations can be easily compensated real-time in the system through various elegant means. In our system, we deployed an image post-processing mechanism.

It is obvious to recognize that the largest image size is dependent on the shortest scan length possible. We then remove the extraneous spatial points of higher wavelengths to reconstruct the spectral image. With the two galvano-mirrors performing the bow-free spectral scan, the

spectral accuracy of the data points is ensured. To obtain a spatially-undistorted image, we interpolate the two spatially nearest intensities of each desired Cartesian pixel location.

The algorithm can be broken down into the following steps:

1. Index each scan line intensity separately
2. Calculate the respective wavelength being acquired during each scan line
3. Calculate the respective scan length for each wavelength
4. Calculate the spatial positions for each pixel considering the scan lengths and sinusoidal oscillation of the grating scanner
5. To reconstruct an image, we consider only the shortest possible scan length (at the lowest wavelength) and remove the extra spatial points for the rest of the wavelengths

## 5. Double-Galvano Mirror Implementation

### 5.1. Optical Setup and Procedure

A prototype system was set up to demonstrate the operation principle. The intent is to illustrate the capability of the system to

- a) Accurately identify the location(s) of an object in the spatial domain
- b) Accurately identify the wavelengths of the object

With those objectives in mind, two fiber pigtailed laser diodes of wavelength 635 nm and 653.3 nm are used. The laser signals are sent to a fiber assembly setup consisting of two single-mode fibers aligned along the  $z$ -axis with a center-to-center distance of 11 mm as a line test target for the spectral imaging system.

As a proof of concept to simplify the system, foreoptics are not used. Instead, this line test target is used to emulate the image passing through a slit aperture located in the image plane of a foreoptic system. The output light from the fiber assembly setup is collimated by a lens of focal length 150 mm. After passing through the scanning system consisting of two galvano mirrors and a MEMS grating with a period of 500 nm, the light is focused by a lens with a focal length of 150 mm to its focal plane where a pinhole of diameter 400  $\mu\text{m}$  is employed to limit the spectral band and field angle seen by the high-speed avalanche photodiode (APD). From Chapter 4, the spectral resolution and spatial resolution can be estimated by equation (33)

$$\gamma_{\max} = \tan^{-1}(D/2f)$$

The angular extent of the field angles from which the incident light can be collected by the detector is roughly  $2\gamma_{\max}$  and equation (34) tells us that

$$\delta\lambda_{\max} = 2 \tan^{-1} \left( \frac{D}{2f} \right) d$$

With  $D = 400 \mu\text{m}$  and  $f = 150\text{mm}$ , this system has therefore an estimation spectral resolution of  $1.3 \text{ nm}$  and a geometric spatial resolution of  $0.4 \text{ mm}$  along the line test target.

Fig.5.1. below illustrates the optical setup schematic.

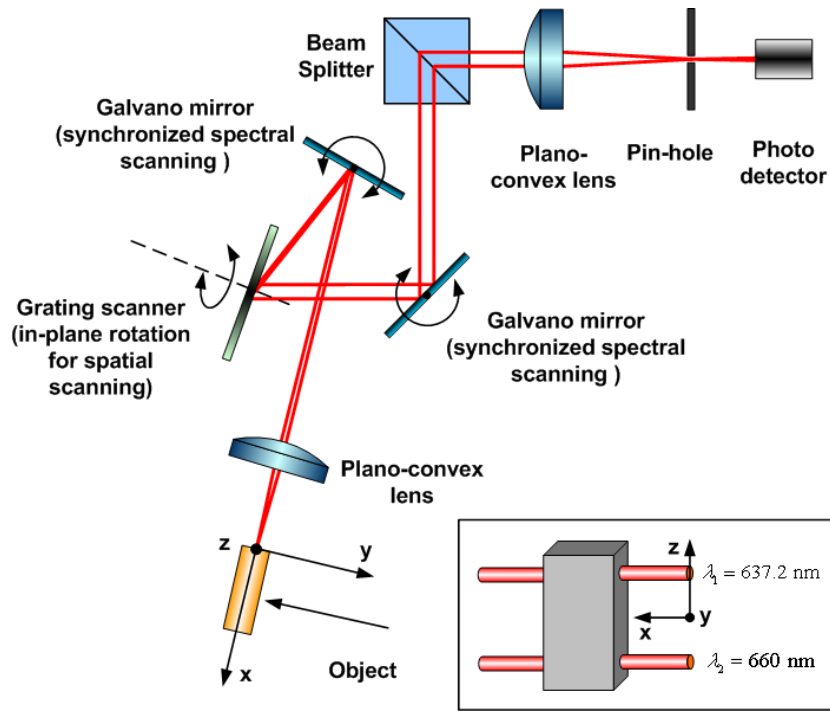


Figure 5.1. Schematic showing the optical configuration for the proof-of-concept

The actual optical set up is shown in Fig.5.2. below.

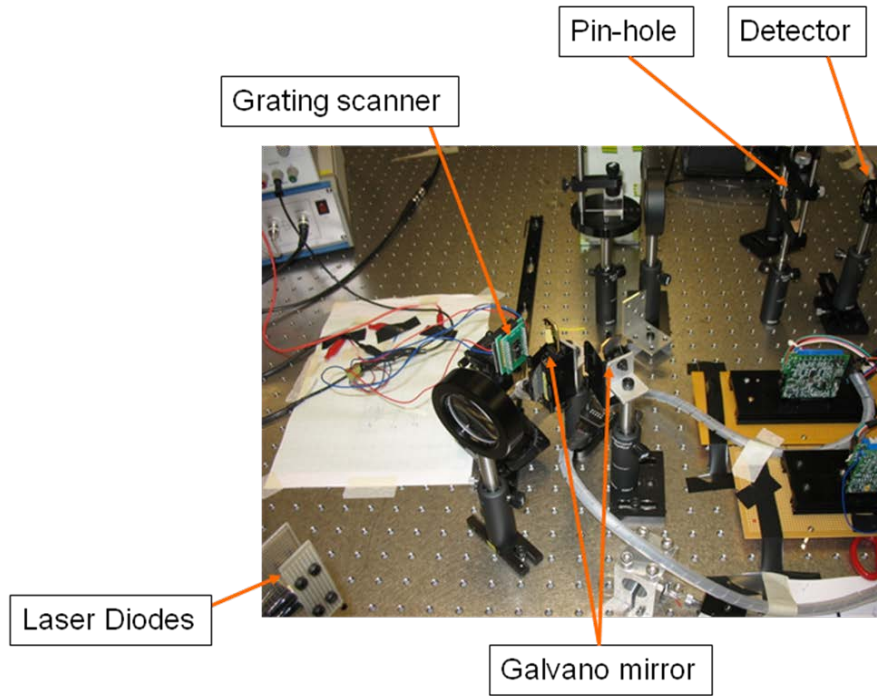


Figure 5.2. The optical setup used in the experiment

The two galvano mirrors are used to adjust the angles  $\alpha$  and  $\beta$  according to the Eqs. (16) and (17), thereby determining which wavelength reaches the detector. For proof-of-concept, the rotational angles of the two mirrors are only calibrated to accommodate a spectral range from 600 nm to 700 nm, i.e. normalized wavelength from 1.2 to 1.4. In this case, the necessary angles to scan are shown in Fig.5.3. below.

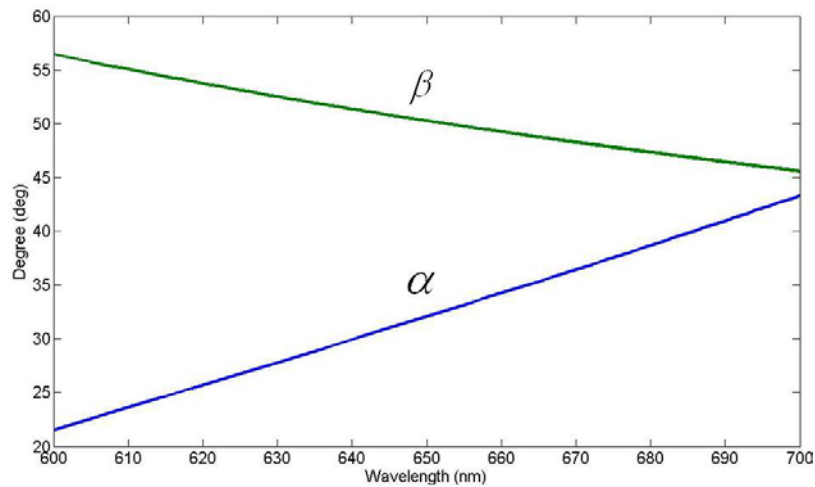


Figure 5.3. Incident and diffracted angles required for bow-free scanning for 500nm pitch grating

Prior to operation, a couple of parameters had to be calibrated. Firstly, the voltage-to-angle ratio was determined for the two galvano-mirrors. Eqns (16) and (17) determines the scanning profile which the two galvano-mirrors have to traverse in order to selectively control the wavelengths that reaches the photodetector. Some preliminary work has to be done to determine the voltage-to-angle ratio of the galvano-mirrors. A target surface was set up at a fixed distance from the galvano-mirrors. A reference laser beam was aimed at the galvano-mirror at  $45^\circ$  and projected to the target surface. The projected scanned length was measured at the target surface while varying the input voltage to the driving circuit of the galvano-mirror. The voltage driving function is then calculated and output using an arbitrary function generator.

Secondly, a He-Neon laser of 632nm was used to align the optical setup and provide the reference wavelength. From Eq (16) and (17), we calculate the  $\alpha$  and  $\beta$  necessary, which is  $7^\circ$  and  $70^\circ$  respectively. For alignment, we traced the optical path from the photo detector to the object instead since the diffractive grating equation is valid bi-directional as mentioned earlier. We decided that at 0V input voltage to the galvano-mirror is to be the beginning of the wavelength, at 600nm ( $21.5^\circ$ ). When doing the optical alignment, the voltage given to the galvano-mirrors are coincident to 632nm. To ensure that the angles  $\alpha$  and  $\beta$  of the system is correctly aligned as well as the positions of the fibre-optic object, the grating scanner is allowed to scan. The resultant scan line at the plane of the object has to be a straight line that passes through the center of the two fibre-optic outputs.

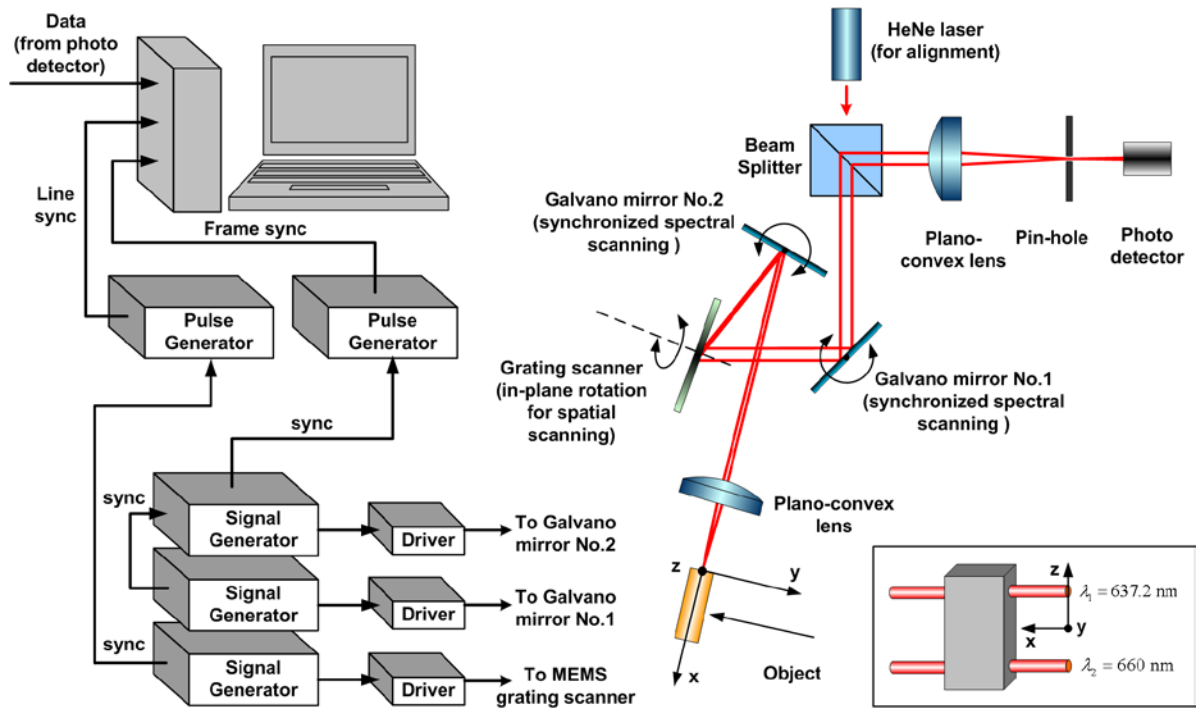


Figure 5.4. The signal synchronization and control necessary in the imaging system

With the grating scanner performing the high-speed spatial scanning and the galvano-mirrors scanning the slower spectral sweep, the operating frequency of the galvano-mirrors effectively determines the frame-rate. Considering that the rotation of the galvano-mirrors has to travel a non-linear triangle path and that the amplitude is large, it was not possible to operate it at more than 200Hz. The maximum framerate of the system is limited as such. The spectral resolution of the system is limited by the optical resolution permissible through the pin-hole and as well as the relative operating frequencies between the grating scanner and galvano-mirrors.

Synchronization was a major issue in the setup. There were a total of 4 signals which had to be synchronized concurrently: two galvano-mirrors, one grating scanner and one photodetector. The main driving signal was the one to the grating scanner. The driving signal initiates the acquisition by sending a triggering pulse at the onset of each scanning line. It was necessary then to compensate for the delay in the driving signal and the scanner to make sure



the trigger only occurs at the start of the scan line. For this, an initial test is necessary to be performed utilizing an acousto-optic modulator to determine the delay which will correspond to the start of the scan line.

Fig.5.5. below shows the setup that was performed to obtain this delay. A He-Neon laser of 632nm is directed on the grating scanner which is operated at its resonance frequency. An acoustic optical modulator is placed in between the optical path to allow only certain phases through the grating scanners operating period to pass. The operation of the optical modulator and the driving signal of the grating scanner are thus synchronized. The diffracted beam is allowed to scan onto a CCD camera which is relayed onto a screen. As the grating scanner is operating at resonance, the phase delay of the modulator is adjusted until the spot seen is located at the end of the scan line. This phase delay is then the phase difference between the driving signal sent into the grating scanner and the actual rotational position of the grating scanner. Once that is obtained, multiple pulses at different phases of the driving signal are sent to verify the consistency of the grating scanner's operation. It is seen from Fig.5.5 below that stable spots are seen on the monitor, thereby illustrating the stable operation of the grating scanner as well as the sinusoidal oscillatory behaviour.

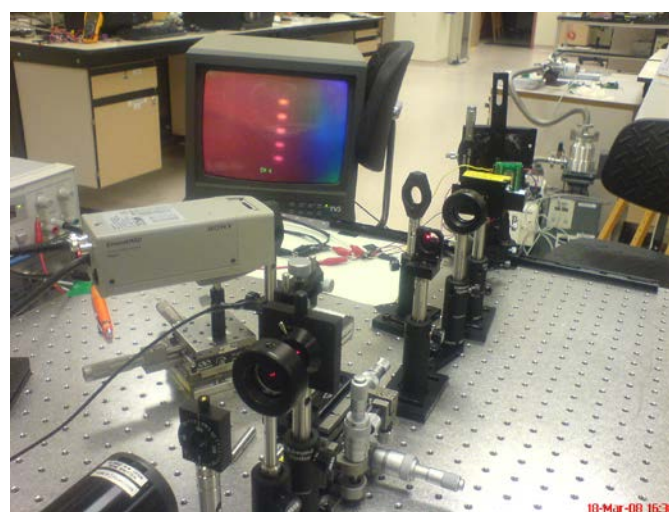


Figure 5.5. Optical setup showing stable laser spots when grating scanner at resonance

The acquisition begins from the start of the driving signal of the grating scanner. The phase delay acquired is incorporated to generate a synchronization pulse. This triggers the scanning of both galvano-mirrors as well as is used as a reference signal to the data acquisition system to start reading signals from the photo-detector. The synchronized pulse is thereby coincident with the start of the grating scanner's optical scan line and generated for every one.

The driving signals for both galvano-mirrors are synchronized. As can be seen from Fig.5.6. the waveform for  $\alpha$  (galvano-mirror 2) is essentially linear throughout the scan range of 600nm-700nm. The resultant necessary waveform for  $\beta$  (galvano-mirror 1) however is not. A triangle waveform was generated for galvano-mirror 2. The waveform for galvano-mirror 1 is less straightforward since it is non-linear. The data points for the waveform was calculated and manually entered into as an arbitrary waveform pattern in the function generator. The function generator is then controlled to generate the waveform by sweeping through the datapoints both in the forward and backward directions, resulting in the pseudo-triangle output. Fig.5.6. shows the waveform generate for each galvano-mirror for one period. The voltage for galvano-mirror 2 is inverted since the galvano mirror is rotating in the opposite direction from galvano-mirror 1.

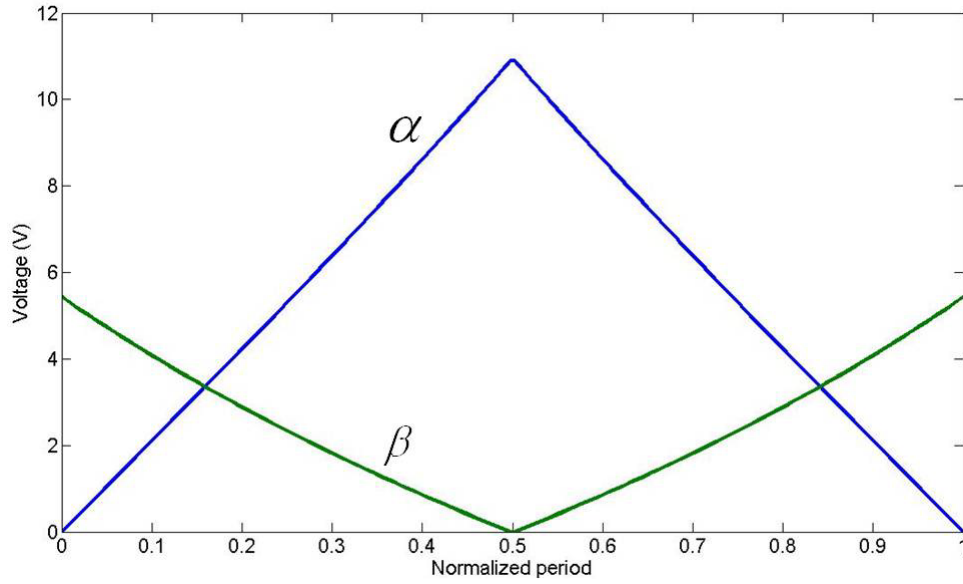


Figure 5.6. Schematic showing the driving voltages for both galvanometers

The generated signal for galvanometer 2 is sent to the acquisition system. Each periodic waveform from galvanometer 2 represents a fully acquired spectral frame for the line imager. By monitoring the number of triggering pulses, we essentially determine the number of scan lines per frame. We configured the system for a single pass for the two galvanometers i.e. no data is acquired on the return pass of the grating scanner.

Signal intensity from the photodetector is acquired at a constant sampling rate of the data sampling system. Without a positioning feedback mechanism, intensity values are acquired throughout each scanning period upon activation by the synchronization pulse. The wavelength that is currently being scanned is known through the acquired galvanometer's driving signal. Each intensity values' spatial location is thus determined by knowing its phase during the scan and the wavelength being scanned.

## 5.2. Results

Fig.5.7. shows the acquired post-processed spectral line image. The x-axis is the calculated distance of along the optical scan line. The y-axis is the wavelength selected

through the two galvano-mirrors. The two spots of higher intensity represent the location and spectral information collected of the two laser diodes. The peaks are found to be at 635.5nm and 656nm which corresponds well to the actual 635nm and 653.3nm laser diodes used respectively. The measured distance between the two diodes is found to be 11.4mm compared to the actual distance of 11mm. Both results demonstrate the viability of the configuration. The frame-rate is currently limited by the scanning speed of the galvano-mirrors, peaking at about 200Hz before instabilities sets in for our system. Replacing them with higher speed MEMS micromirrors would allow better performance. MEMS micromirrors can typically achieve scanning rates at kilohertz range.

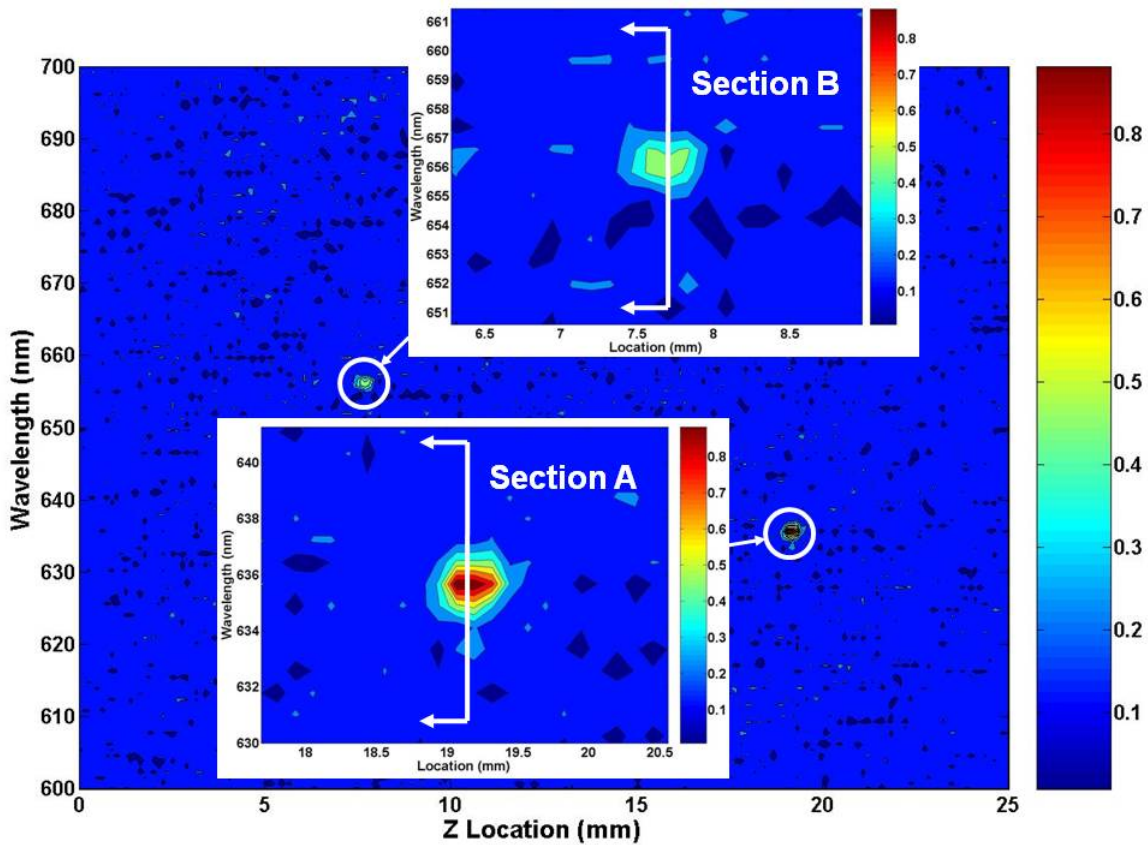


Figure 5.7. Post-processed spectral image with insets showing the detailed spot profiles

Fig.5.8. further shows the cross-sectional view of each of the detected peaks.

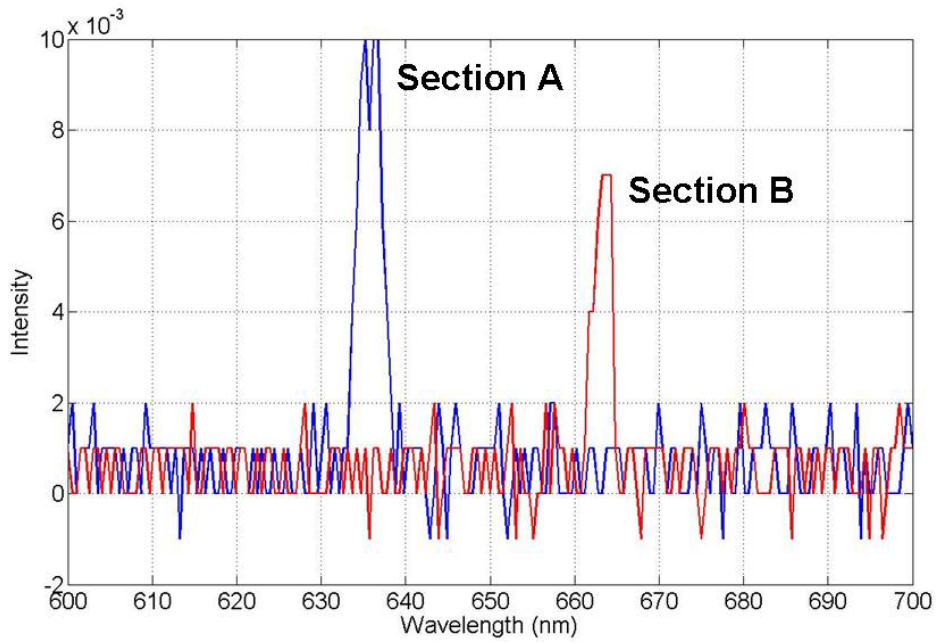


Figure 5.8. Schematic showing the spectral cross-section profile of the laser diodes

### 5.2.3. Summary

Several observations can be made on the system. Firstly, in order to achieve the bow-free scan throughout all visible wavelengths between 450nm to 650nm, the two mirrors need to traverse a wide range of angles. With a grating scanner of 500nm pitch, the dispersion is insufficient to cover all the wavelengths. Even with a 400nm pitch, the necessary scan angles are shown below.

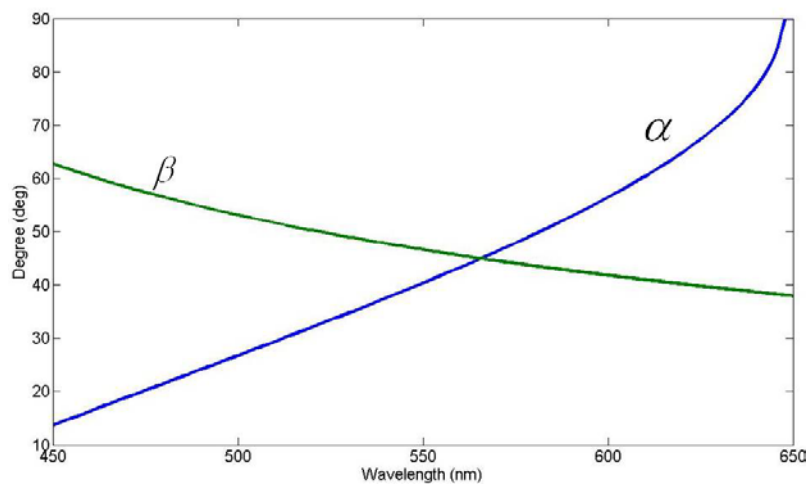


Figure 5.9. Incident and diffracted angles required for bow-free scanning with 400nm grating

The  $\alpha$  needs to be adjusted from a wide range of  $14^\circ$  to close to  $90^\circ$ , which is impossible. The wide angles to be covered imposes limitations not only in the rotational range of the galvano-mirrors in real-time but also the optical configuration. Each of the galvano-mirrors has about 10mm width. It will be challenging in the optical layout to arrange the galvano-mirrors to be able to cover such a wide angle without overlapping the other galvano-mirror.

Secondly, it can be seen that synchronizing multiple signals imposes significant burden on the control elements. More importantly, having the two galvano-mirrors working in perfect tandem is essential in obtaining an accurate spectral profile.

Lastly, small galvano-mirrors with a large rotational angle capable of operating at 60Hz or higher traversing non-linear profiles are uncommon. The galvano-mirrors we worked with barely made the grade. Having two of such galvano-mirrors in the system severely limits the future miniaturization.

### **5.3. Zeroth-order Optical Feedback**

We obtained spatial information through calibrating the phase difference between the driving signal and the actual scan position. It is a simple mechanism that works sufficiently well at low resolution when a positioning feedback loop is lacking. However, it will be inadequate when resonance frequency of the actuator changes over time due to fatigue or environmental conditions. To truly utilize the grating scanner as a viable scanning mechanism, closed-loop control is required. This requires a feedback signal in terms of a position sensor to obtain the scanning amplitude and phase information. Encoders, piezo-electric[22] or introducing additional incident beams[23] are some of the ways typically used to acquire real-time position information for other scanning systems. The vibratory grating scanner possesses a unique inherent optical signal which can be tapped to obtain a real-time position feedback.

As mentioned earlier, a diffraction efficiency greater than 75% is attainable when a TM-polarized beam is incident on the sub-wavelength gold-coated grating [9] with optimal groove depth. The high-efficiency first-order diffracted beam scans while the zeroth-order beam remains stationary as the grating platform rotates.

To illustrate the viability, rather than scanning, a grating scanner with a 400nm pitch grating platform is statically rotated. A TM-mode beam of 532nm is incident on the grating scanner  $35^\circ$ . The resulting first-order diffracted beam is measured at  $49^\circ$ . The grating scanner is statically rotated and the diffracted beams intensity is collected and measured. Fig.5.10. shows the percentage drop in intensity over the  $20^\circ$  optical scan angle. A drop of optical intensity of only about 4% is seen over the full angular rotation, demonstrating the viability of a well-designed sub-micron grating scanner.

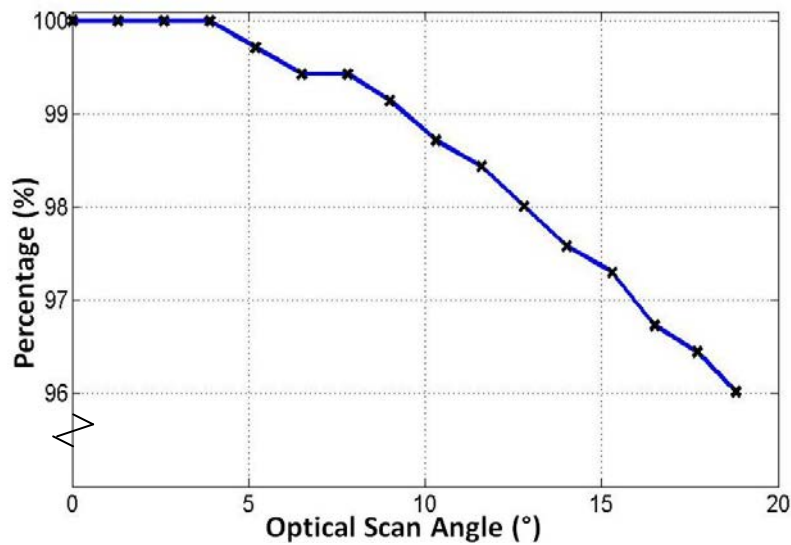


Figure 5.10. Graph showing the percentage drop in overall intensity of the first-order diffracted beam as the grating platform is rotated with respect to an incident TM-polarized beam.

This loss of intensity at the first-order beam should manifest itself as an increase in the zeroth-order beam. In addition, due to the polarization-sensitive sub-wavelength diffraction grating used, we also anticipate a change in the output polarization of the diffracted beams. Thus, we expect changes in both intensity and polarization of the zeroth-

order beam as the grating rotates and attempted to profile this relationship to investigate the possibility of utilizing it as a position feedback signal.

This change in intensity is only apparent when a polarized light source like a laser is used. A broadband source without polarization will not be able to utilize this mechanism. In that perspective, this mechanism will not be suitable when imaging a scene such as in a spectral imager because the polarization of light from the object is likely to be random. However, modifications can be made to the gratings scanner device or the optical system in order to incorporate this mechanism. For example, an additional laser source and detector can be carefully placed in the optical system separately to monitor the zeroth-order beam of the laser.

Firstly, we attempted to characterize the variation in intensity of the zeroth-order beam. Fig.5.11. below shows the schematic of the optical setup to demonstrate the measurements. A TM-polarized light is incident on the 400nm pitch grating scanner with 150nm groove depth. As the grating rotates  $\phi$ , the first-order beam scans accordingly. The zeroth-order beam however remains stationary throughout the scanning process.

Since we suspect that this out-going zeroth-order beam contains polarization information, a polarizer is placed in front of the out-going zeroth-order beam before reaching the photodetector. This polarizer can be rotated at an angle of  $\theta_p$  thus allowing only a component of the zeroth-order beam to be incident on the detector. The polarizer's angular reference is in-line with the polarized incident beam. Thus, at  $\theta_p = 0^\circ$  corresponds to being aligned with the incident TM-polarized beam. The first-order beam is optically directed to scan in a line perpendicularly to the plane of the incidence as the grating rotates  $\theta_R$ . Through proper selection of the conditions [10], the scanned line can be shown to be bow-free.



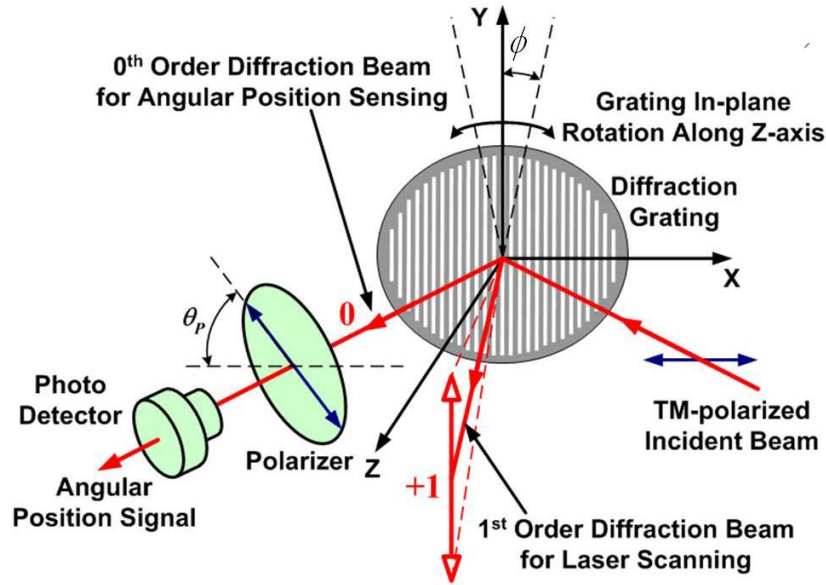


Figure 5.11. Schematic of the optical setup to measure the zeroth-order beam

As a preliminary test of the hypothesis, the polarizer was fixed at two orthogonal extremes:  $0^\circ$  and  $90^\circ$  and the zeroth-order's beam intensity were monitored at various grating's rotation angle. Fig.5.12. shows the results. At  $0^\circ$ , we see that the intensity values drop as the grating scans. This is as expected. At  $0^\circ$ , the maximum intensity passes through the polarizer. Optimal intensity occurs at rest where the incident TM-mode is simply diffracted off the grating without any change in polarization. As the grating rotates in either direction of the rest state, the diffracted radiation beam's polarization rotates as well. The resulting component that is aligned at  $0^\circ$  polarization decreases.

The converse happens when the polarizer is turned  $90^\circ$ . At rest, minimal amount of radiation passes through the  $90^\circ$  polarizer since it will be perpendicular to the incident TM beam. This is evident in the absolute intensity reading of about 4mV, which is significantly less than at  $0^\circ$  polarization. With the polarizer's orientation fixed in space, increasing amount of TM-mode radiation passes through to the detector as the grating's rotation angle increases.

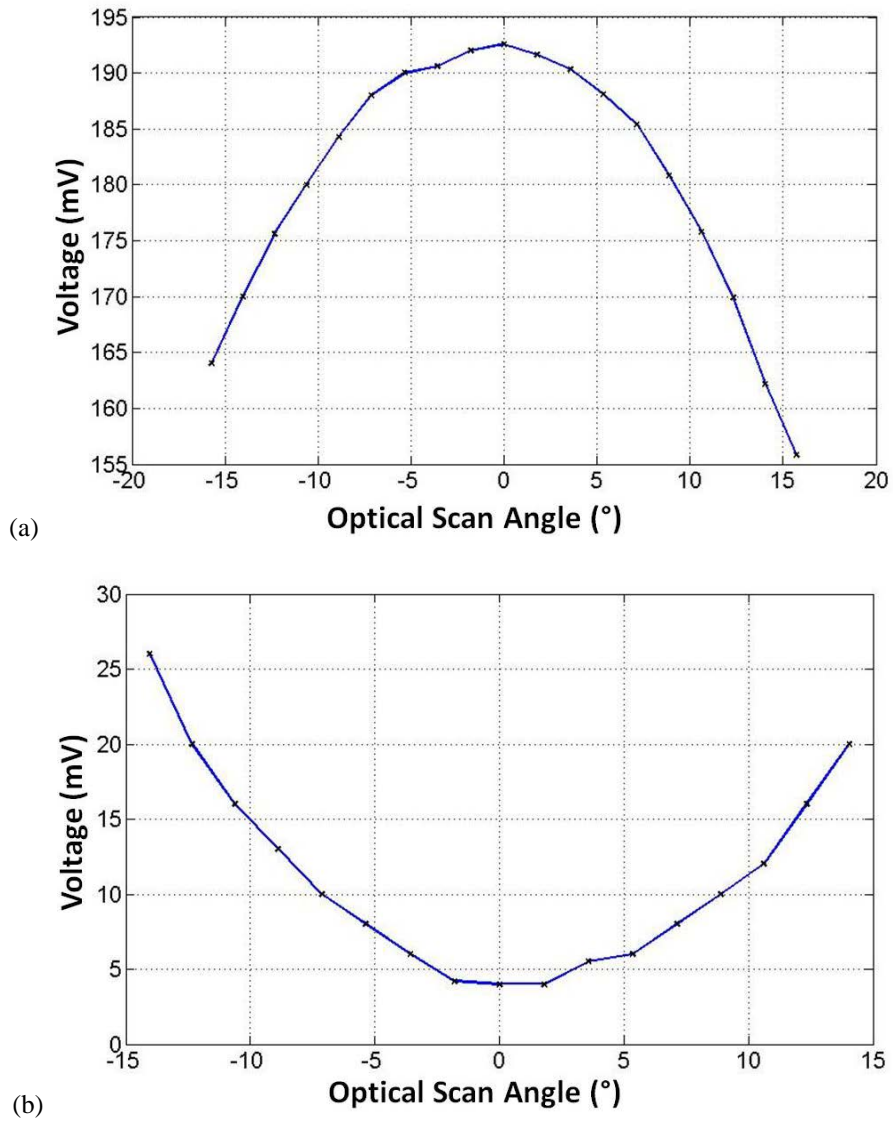


Figure 5.12. Intensity profile of zeroth-order beam at orthogonal polarization angles of (a) 0° and (b) 90°.

We require a linear relationship between the voltage and optical angle in order to utilize it as a feedback signal. Apparently, neither of these extreme conditions meets the requirement. However, we should expect a particular polarization that satisfies and we proceeded to determine that angle through exploring the intensity profile through all the polarization angles.

For a feedback signal, a linear relationship between the output signal and position is desired. To find out what is the best orientation to accomplish this, we varied the polarizer to obtain the intensity distribution as the grating rotates. The polarizer's angle  $\theta_P$  is in reference

to the plane of the incident beam and zeroth-order beam, with  $0^\circ$  being aligned with the incident TM-polarized beam. Fig.5.13. shows the intensity of the zeroth-order beam as the grating is statically rotated over the scanning range of between  $-20^\circ$  and  $20^\circ$ . We normalize the intensity readings to reflect the respective change in detector voltage readings when the grating scanner is at rest.

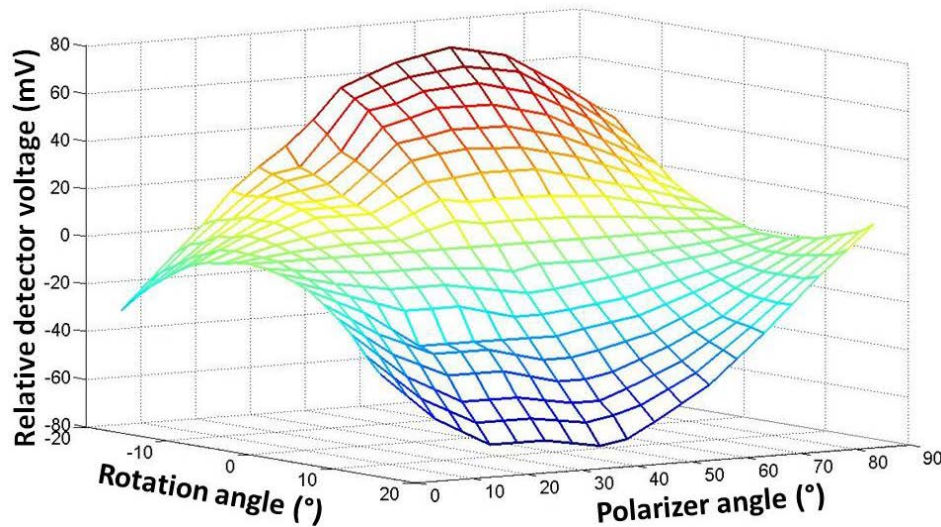


Figure 5.13. Graph showing the profile of the intensities obtained for the zeroth-order beam as the polarizer and the rotation angle of the grating is changed

At  $90^\circ$  polarization, we expect an increasing intensity profile for both ends of the rotation of the grating. This results in a ‘smile’. Utilizing the zeroth-order signal as a positioning signal requires a linearly varying intensity relationship with rotation angle. From Fig.5.13, we can see that such a signal occurs when the polarizer is aligned at  $45^\circ$ .

To demonstrate the viability of using the zeroth-order to do real-time position sensing, we actuated the device at resonance of 21.5 kHz at various amplitudes. The photodetector detects a sinusoidal time-varying intensity signal. The peak voltage is measured. Fig.5.14. below shows the resultant correspondence. A good linearly-varying intensity response to a changing amplitude of the optical scan angle of the grating scanner is demonstrated.

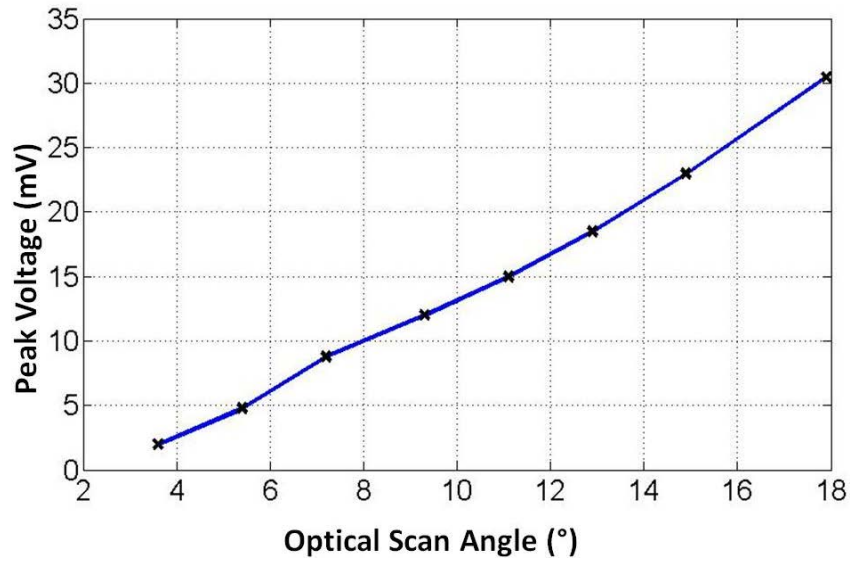


Figure 5.14. Zeroth-order peak voltage with respect to the optical scan angle during resonance operation

Fig.5.15. shows the actual driving signal before amplification with the acquired output waveform. The phase of the detected signal is  $90^\circ$  out-of-phase, clearly demonstrating the device operating at resonance. The phase difference is also well maintained throughout the different amplitudes.

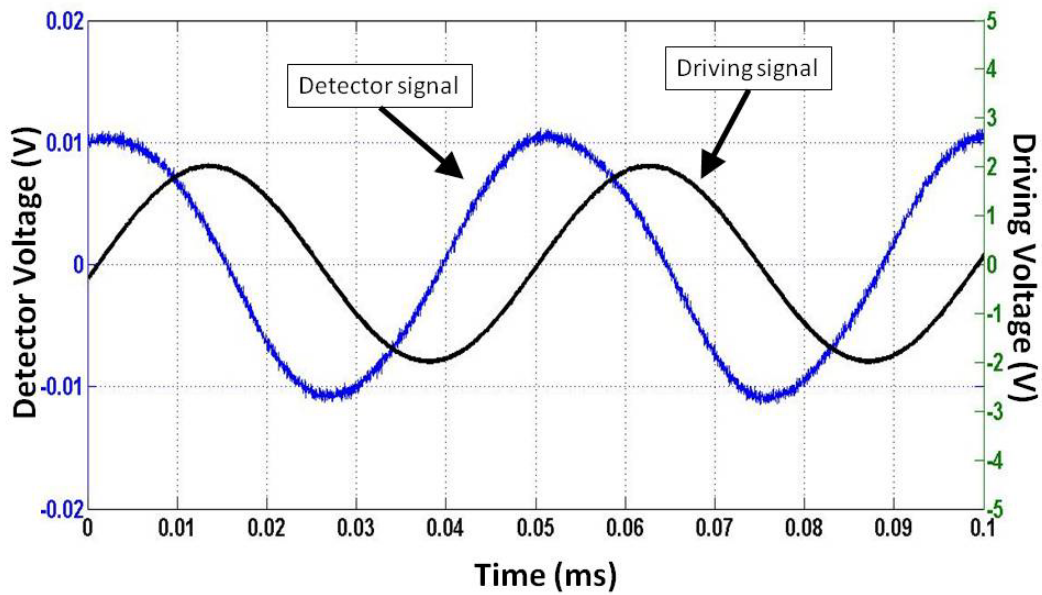


Figure 5.15. Real-time sinusoidal driving voltages and acquired detector readings for the zeroth-order beam

With the first-order beam performing the scanning operation, the zeroth-order beam can

be used as an effective position feedback for closed-loop operation. An optical configuration was demonstrated to be viable to tap into the zeroth-order beam's intensity change with respect to the grating's rotational angle by having a polarizer at  $45^\circ$  polarization before incident on the detector. The polarizer's angle was varied between  $0^\circ$  to  $90^\circ$  to explore how the intensity signals change as the grating rotates. The  $45^\circ$  polarization was demonstrated to be optimal in terms of obtaining a linearly varying signal.

This mechanism is suitable only for incident light with fixed polarization e.g. laser beams. For imaging objects with random polarization such as the case for a spectral imager, modifications to the optical system might be necessary to incorporate this mechanism. An additional laser beam and source can be carefully selected and placed in the optical system. Or if modifications to the grating scanner device fabrication process can be managed such that gratings can be etched on the backside of the platform, the additional laser source and detector can utilize the rear grating for position sensing.

## 6. Single-Galvano Mirror Configuration

### 6.1. Overview

The double-galvano mirror configuration suffers from several shortcomings. The reliance on having two galvano mirrors to control the spectral band results in a complicated system. Firstly, two galvano mirrors have to be synchronized together the grating scanner and single-pixel detector to reconstruct the line spectral image. This places additional burden on the electronics in terms of control and power requirements. Each galvano-mirror introduces a high power load requirement which limits the mobility of the system. Secondly, the size of the galvano-mirrors limits the miniaturization of the overall system. The two galvano-mirrors and the driving electronics take up substantial space. Thirdly, requiring two galvano-mirrors to control the spectral range limits the possible operational range of the system.

The key objective of having the two scanning mirrors is to maintain the bow-free scanning conditions for every wavelength. Properly synchronized, the incident and diffracted angles are correctly positioned during scanning to minimize the spatial distortion. Without which, a nonlinear distortion arises in the spatial location during scanning.

However, such distortions can be computationally compensated. One way is by pre-calculating the spatial and spectral locations of each distorted sample point and mapping them to the required spatial and spectral locations. Thus by removing the “smile” correction mirror, the system becomes less complex but increases the image processing cost, which in today’s microprocessors is fully capable to handle. Electronically, there is one less mirror to synchronize and less power to operate. In the original configuration, this mirror is required to be driven at high frequency which can be challenging to implement and possibly require high

power. Optically, there is one less optical component to align and can therefore reduce the overall size of the system significantly and improve the robustness of the system.

## 6.2. Image Processing

Three imaging artefacts occur during the data collection process. The first, as mentioned earlier, is the spatial distortion due to the nonlinear diffracted angles of the various wavelengths, “smile”. The second is the spectral distortion due to a different scanning angle for different wavelengths. The combined effect of the first two artefacts results in an acquired distorted profile of which a possible example is as shown in Fig.2.2. reproduced below. The region that is linear (in the figure below is 400nm), will be the one that satisfies the bow-free scanning condition. The rest of the wavelengths will exhibit smile distortion during the scanning process.

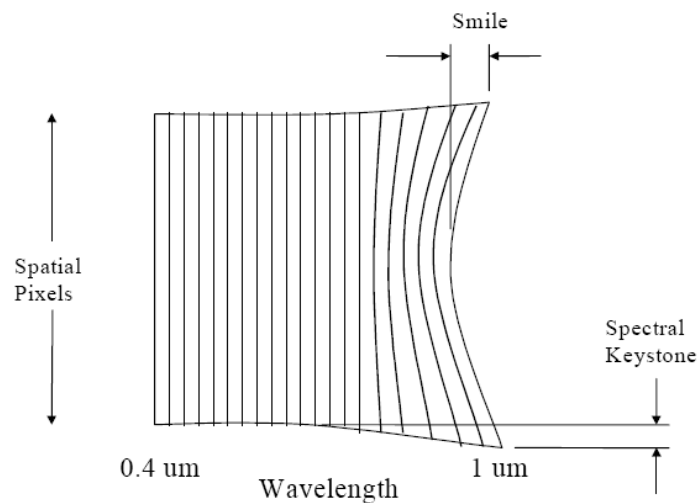


Figure 2.2. Schematic xxx

The third is due to the constant sampling rate utilized by the ADC and the sinusoidal vibratory oscillation of the grating scanner. This results in the spatial points acquired not being evenly distributed along the spatial scan line.

The objective is to correct these distortions post-sampling. All of the sampled data

points can be correlated to their actual wavelengths and spatial locations, as the mirror, grating scanner and the acquisition timing are synchronized. The resulting distorted image map is much similar to the figure above. From this known distorted image map, a corrected profile where the wavelengths and spatial points are linearly distributed is required, of which the points are known. Since the locations of the corrected points will not likely fall correspondingly to the acquired points, some way of mapping one onto the other is required.

The means of achieving this is simply to realise that the information of these corrected points lies collectively in the nearest neighbouring acquired points. The key is to select efficiently which of these neighbouring acquired points should be used for each corrected point and then perform a two-dimensional interpolation amongst the points. With a sufficient dense number of points, the resultant compensated spectral map should be accurate. Since the image space is two-dimensional in nature, three data points or a triangle is sufficient to fully describe any region within the sampled space.

### **6.2.3. Delaunay Triangulation**

One way of selecting neighbouring points is through Delaunay triangulation (DT) [27]. Delaunay triangulation is a commonly used algorithm for generating triangle meshing, often used in finite element modelling and finite volume modeling. A key characteristic of DT is that it maximises the minimum angle of all the triangles in the mesh. In our situation, it basically minimises the furthest distance of the neighbouring points from which to select for each corrected points, thereby improving the accuracy of the subsequent interpolation step.

The key premise in DT is that no fourth point should lie in any meshed circumcircle, which is also known as the Delaunay criterion. On this basis, several algorithms are available in literature to generate the required 2D mesh. Our approach is based on the Quickhull algorithm which utilizes the computation of convex hulls to determine the Delaunay



triangulation. The convex hull of a set of points is defined as the smallest convex set that includes all the points.

The Quickhull algorithm employs a recursive approach to determine the convex hull given a set of points,  $P$ . The algorithm is as follows:

1. Find the two furthest points,  $P(1)$   $P(2)$ , in a particular direction
2. Draw an imaginary line between the two points  $P(1)$   $P(2)$
3. Separate the rest of the points into two sectors depending which side of the line they lie
4. For each sector, find the furthest point  $P(3)$  perpendicular to the imaginary line drawn in step 2.
5. Draw two imaginary lines from the previous two points to the new furthest point
6. A triangle is created between the three points and points that lie inside the triangle are henceforth ignored
7. Consider the line  $P(1)$  to  $P(3)$ , find the furthest point  $P(4)$  and form triangle again
8. Repeat until no more points are available

Finding the Delaunay Triangulation of a set space  $P$  is through using a property which states that the exterior face of the Delaunay Triangulation is the convex hull of the point set. Thus, to generate the Delaunay Triangulation of set space  $P$ , is to sequentially remove each point of the generated convex hull.

#### **6.2.4. Processing Steps**

The first step is to calculate based on a system model, the set of points in the spectral

image plane that the data acquisition system is collecting. This set of acquired points is the basis for the Delaunay Triangulation. Performing DT on these points results in a mesh network being generated. Fig.6.1. below illustrates a sample spectral image plane with 10x10 points in order to visualize clearly the mesh network generated. The points in red are the locations that the data acquisition system collects intensity information on, the lines in blue are the mesh network generated using DT.

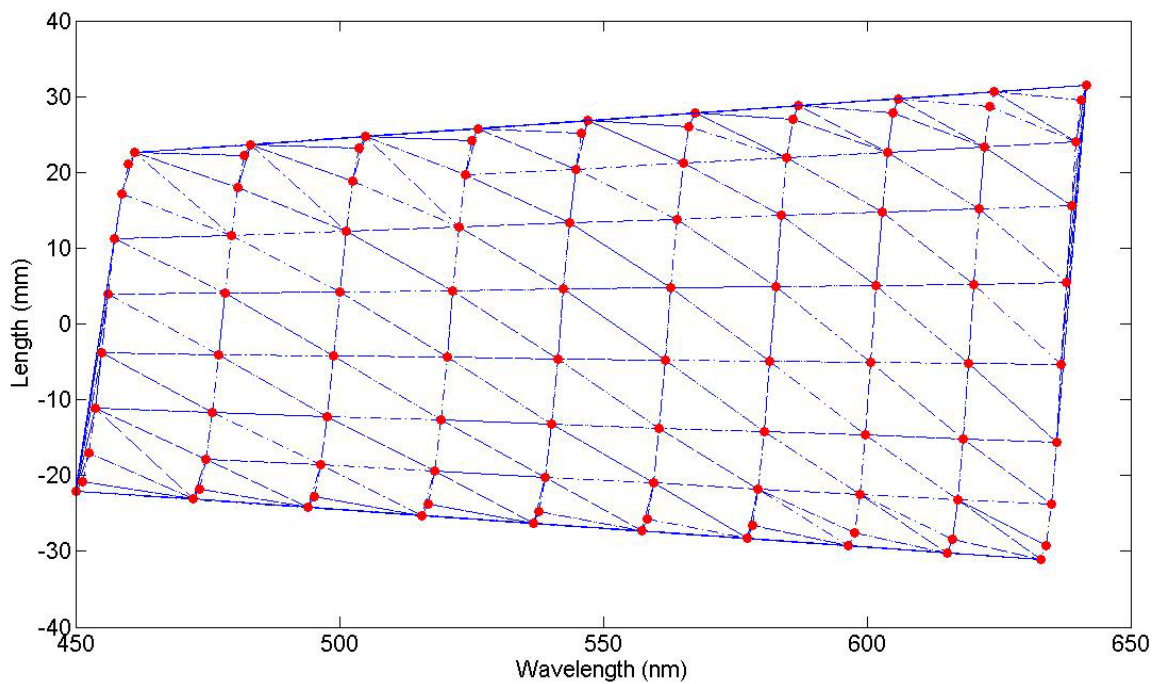


Figure 6.1. Schematic illustration showing three major image distortions in the proposed spectral imager and meshed network using DT on a modelled 10x10 set of points.

Once obtaining the meshed profile based on the modelled sample points, the next step is to determine the locations on the spectral image plane where a generated image should result. Most likely, it should form Cartesian grid. Each of these points should lie within one of these meshed triangles. A triangle bilinear interpolation algorithm is then performed to calculate the corrected points intensity.

Fig.6.2. below shows the desired corrected Cartesian profile superimposed on the

uncorrected spectral map.

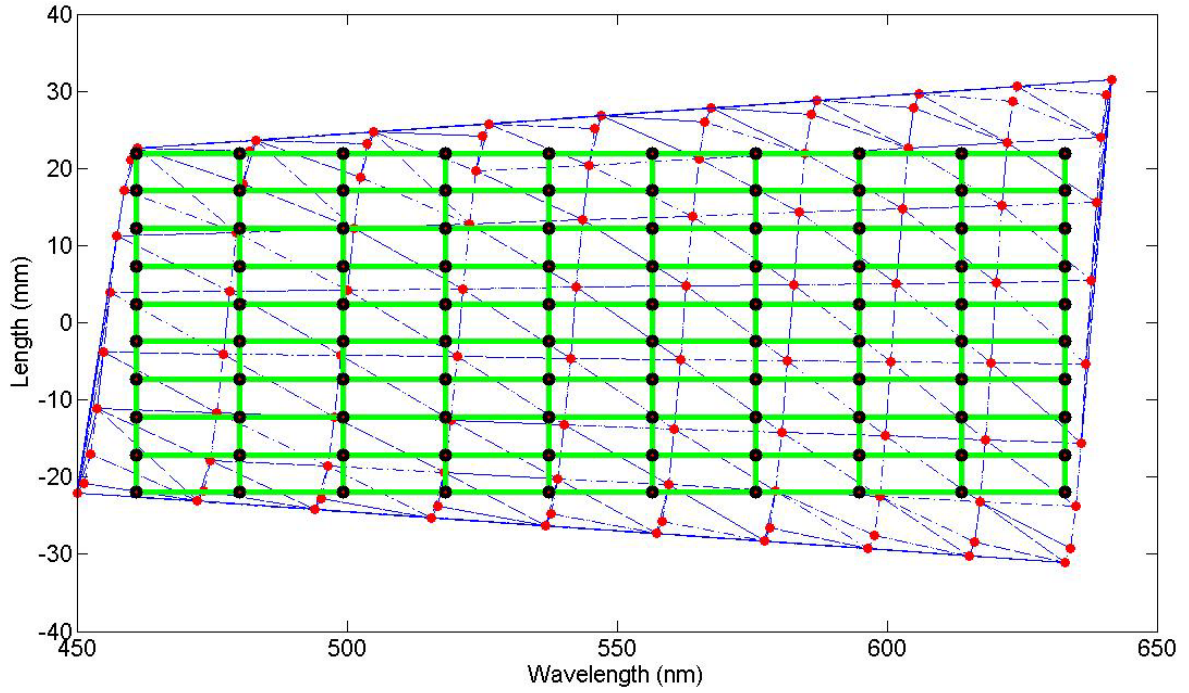


Figure 6.2. Schematic illustration showing meshed network using DT on a modelled 10x10 set of points with the desired Cartesian grid

For every corrected point  $P = (x, y)$  within the triangle of points  $P_1 = (x_1, y_1)$ ,  $P_2 = (x_2, y_2)$  and  $P_3 = (x_3, y_3)$ , each having an intensity  $I_1$ ,  $I_2$  and  $I_3$  respectively, obtain the weights  $a$ ,  $b$  and  $c$  such that

$$A\lambda + By + CI + D = 0$$

The relationship between parameters  $A$ ,  $B$ ,  $C$  and  $D$  can be obtained by solving

$$\begin{bmatrix} A & B & C \end{bmatrix} \begin{bmatrix} \lambda_1 & \lambda_2 & \lambda_3 \\ y_1 & y_2 & y_3 \\ I_1 & I_2 & I_3 \end{bmatrix} + D \begin{bmatrix} 1 \\ 1 \\ 1 \end{bmatrix} = 0$$

Thus the intensity of the data point  $P(\lambda, y)$  can be calculated using

$$I = \frac{D - A\lambda - By}{C} \quad (35)$$

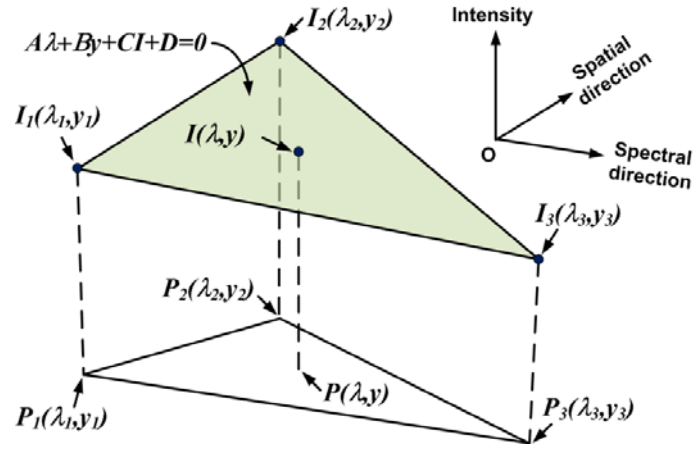


Figure 6.3. Schematic illustration of obtaining intensity of a data point in the correct profile using linear interpolation.

### 6.3. Single-Galvano Mirror Optical Modelling

#### 6.3.3. Sampling Points Modelling

The next step then is to generate a model for the resulting optical system. A distorted image map is generated of the sampled points. The corresponding actual spatial and spectral positions at each sampled point can be calculated through reverse ray-tracing iteratively.

Fig.6.4. shows the schematic of the optical model to be used.

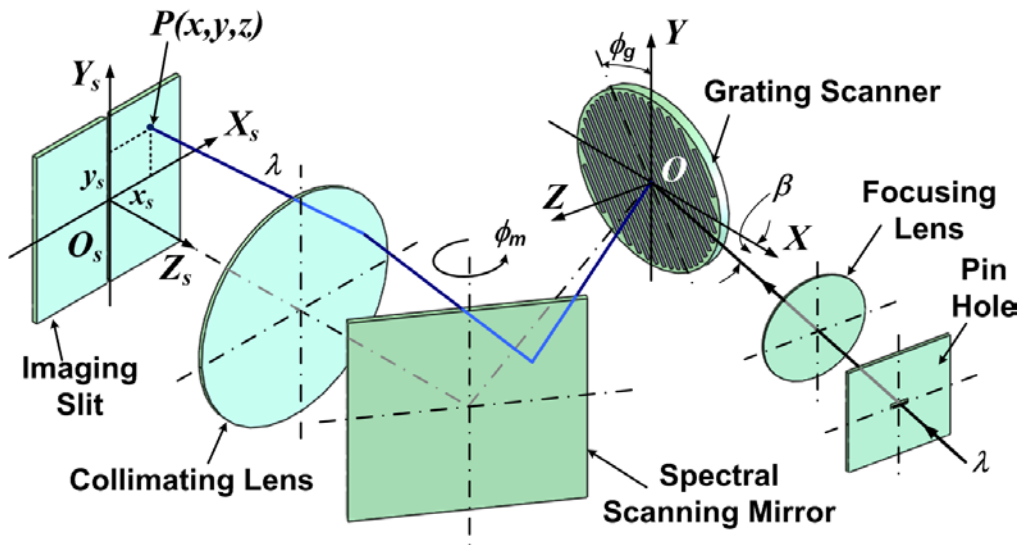


Figure 6.4. Schematic illustration showing the configuration of the improved scanning grating based hyperspectral imaging system.

For  $(i,j)^{\text{th}}$  sampling point, the rotational angles of the spectral scanning mirror and the diffraction grating are denoted by  $\phi_m(i)$  and  $\phi_g(j)$ , respectively. The light propagation direction is reversed, as shown in Fig.6.4. The light starting from the center of the pinhole passing through the center of the focusing lens is traced for convenience. The initial wavelength of the traced light  $\lambda$  is set to be at the center of the spectral searching range, which is from 400 nm to 700 nm in our system. The light is diffracted by the grating, which lies in XOY plane. The unit vector of the outgoing diffraction light  $\mathbf{r}_g$  is calculated based on the expanded equation (10):

$$\vec{r}_g = \left[ -\frac{\lambda}{\Lambda} \sin \phi_g(j) \right] \vec{e}_x + \left[ \sin \beta - \frac{\lambda}{\Lambda} \cos \phi_g(j) \right] \vec{e}_y + \left\{ 1 - \left[ \frac{\lambda}{\Lambda} \sin \phi_g(j) \right]^2 + \left[ \sin \beta - \frac{\lambda}{\Lambda} \cos \phi_g(j) \right]^2 \right\}^{\frac{1}{2}} \vec{e}_z$$

where  $\Lambda$  is the grating pitch;  $\vec{e}_x$ ,  $\vec{e}_y$  and  $\vec{e}_z$  are unit vectors along X-, Y- and Z-axes, respectively. The light is then reflected by the spectral scanning mirror. The unit vector of the reflected light  $\mathbf{r}_m$  from the mirror is calculated using

$$\vec{r}_m = \vec{r}_g - 2 \left\{ \vec{r}_g \cdot \mathbf{n}[\phi_m(i)] \right\} \cdot \mathbf{n}[\phi_m(i)] \quad (36)$$

where  $\mathbf{n}[\phi_m(i)]$  is the normal vector of the mirror with the mirror steering angle of  $\phi_m(i)$ .

The light is focused by the collimating lens and intersected with the imaging slit at point  $P(x,y,z)$ . A coordinate transform from XYZ to  $X_s Y_s Z_s$  is performed to find out the relative position of the intersection point  $P$  on the imaging slit plane, namely  $x_s$  and  $y_s$  as shown in Fig.6.4. Since a narrow slit is placed along the  $Y_s$ -axis on the imaging slit plane, we then assume that if  $P$  is adequately closed to the  $Y_s$ -axis (i.e.  $|x_s| < \varepsilon$ , where  $\varepsilon$  is a small number), the light is judged to be able to pass through the imaging slit. Consequently, according to the reciprocity principle in optics, given the mirror and grating's respective orientation angles

$\phi_m(i)$  and  $\phi_g(j)$ , the light from the point  $P$  is able to pass through the imaging system and recorded by the detector.

Thus,  $y_s$  and  $\lambda$  are recorded to be the corresponding spatial and spectral locations of the  $(i,j)^{th}$  data point in the hyperspectral image, and the intensity reading from the photodetector is assigned to it. On the other hand, if the light is blocked by the slit (i.e.  $|x_s| \geq \varepsilon$ ), either the lower or upper boundary of the spectral searching range is then replaced by the current wavelength  $\lambda$  depending on the sign of  $x_s$ . The ray-tracing procedure is then iterated until the light is able to pass the imaging slit. After considering all the spatial and spectral locations of the sampled data points are recorded and calculated, a distorted image map is obtained. Fig.6.5. shows the flowchart of the calculation procedure.

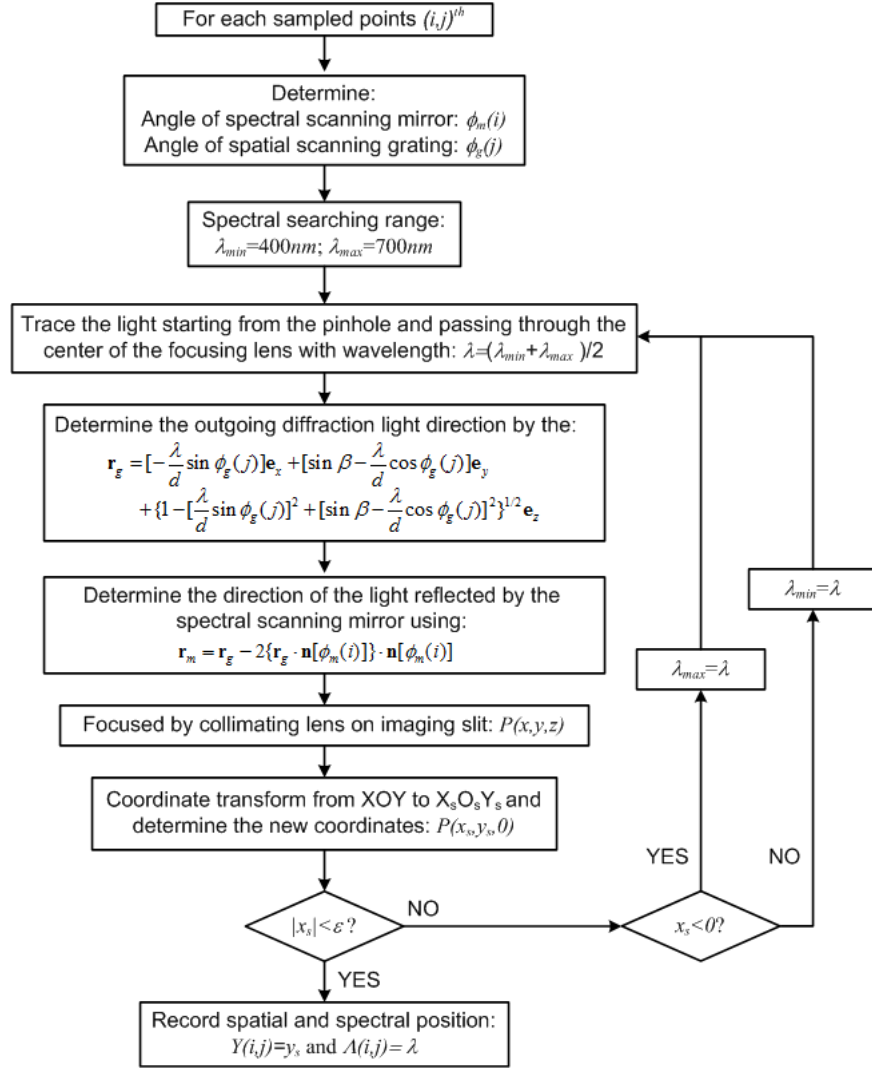


Figure 6.5. Flowchart of obtaining corresponding spatial and spectral positions of each sampled data point using reverse ray-tracing.

#### 6.3.4. Optical Performance

The resulting system configuration is shown in the Fig.6.6. below

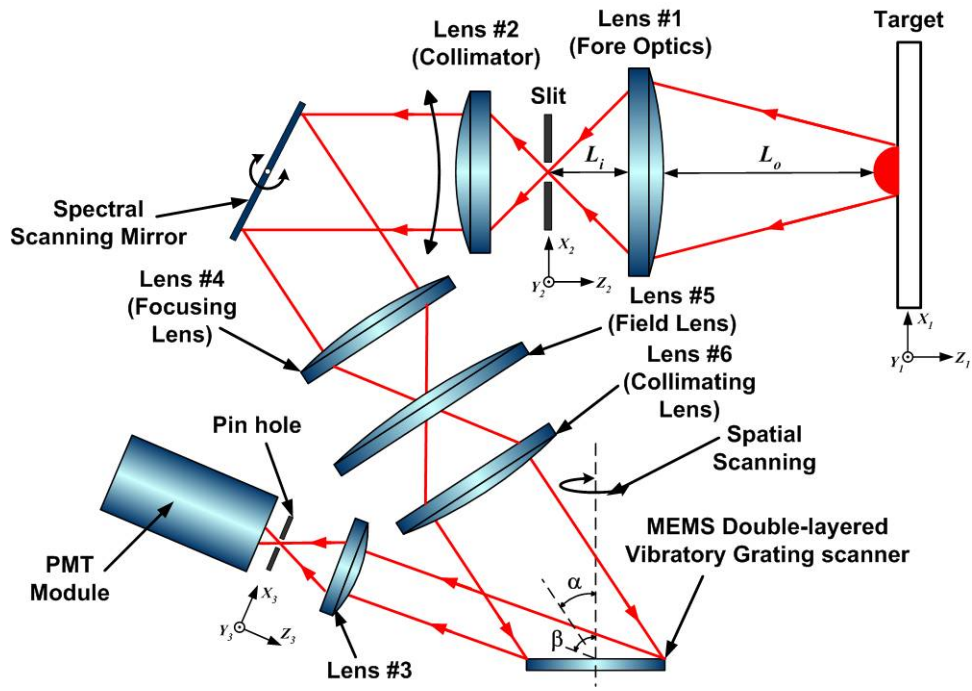


Figure 6.6. Schematic illustration of a single galvano-mirror miniature hyperspectral imager using MEMS vibratory grating scanner.

An imaging lens (lens #1) is placed between an object and an imaging slit. The object distance is 495mm and the slit is placed on the imaging plane of the imaging lens. The light passing through the slit is collimated by lens #2. The collimated light is reflected by a galvano-scanning mirror, which is used for spectral scanning through changing the angle of the reflected light beam.

The collimated light is then illuminated on the grating scanner with an incident angle  $\alpha$ , which is thus determined by the rotation of the galvano-mirror. Considering the size of the grating scanner diameter of only 2mm, the reflected beam off the galvano-mirror easily moves out of the grating scanner's usable area. Lens #4 #5 and #6 are placed between the galvano-mirror and the grating scanner to ensure in resulting incident beam from #6 arrives onto the grating scanner's surface. Lens #4 and #6 are aligned with their focal plane coincidence and the reflected light beam is focused by lens #4 and collimated by lens #6. A



field lens (lens #5) is placed at the focal plane of lens #4. The lenses combination is used to image the spectral scanning mirror at the plane of the grating scanner and maintains the light collimated.

The diffracted light beam from the grating scanner (with an angle  $\beta$ ) is focused by lens #3 and pass through a regular pinhole. The light passing through the pinhole is received by a Photo Multiplier Tube (PMT) detector, which is placed behind the pin hole.

In this manner, the optical performance of the system can be evaluated.

$$FOV_x = \frac{x_2}{f_1} \quad (37)$$

$$FOV_y = \frac{y_2}{f_1} \quad (38)$$

The spectral resolution can be obtained from the previous equation (29)

$$\Delta\lambda = \frac{\Lambda}{f_3} \cos \beta \Delta x_3$$

Similarly, the spatial resolution from equation (31)

$$N_{spatial} = \frac{\Lambda \phi_{opt} \cos \beta}{d\lambda \left( \frac{dy_3}{dx_3} \right)}$$

## 7. Single-Galvano Mirror Implementation

### 7.1. Electronics Setup

The modified system now needs to synchronize only one rotating mirror instead of two, together with the grating scanner and the acquisition system. The synchronization's key again lies with the grating scanner. The rotation angle of the grating has to be determined for every acquired data point in order for post signal processing to be done. Without a built-in position feedback on the device like a piezo-resistive sensor, the alternative is to determine the position through the driving signal applied to the grating scanner. And rather than knowing the angular position of the grating scanner in real-time, we synchronize through a generated pulse which corresponds to a constant phase during operation.

Operating the grating scanner at resonance implies there is a phase difference between the driving signal and the actual oscillation of the device. The objective is to allow the acquisition system to know the start of every oscillation. To achieve this, we synchronized the driving signal with another function generator to output a pulse at a certain delay as per the previous configuration. This delay is to coincide with each peak of the actual oscillation. The acquisition will then trigger at each pulse to sample each oscillation.

The spectral scan is accomplished through the rotation of the galvano mirror. The voltage-to-angle relationship is again pre-calibrated prior to installation. The angle determines which spectral band after dispersion from the grating is picked up by the detector after going through a pin hole. A triangle waveform is used to drive the galvano mirror of which the frequency essentially determines the framerate of the system. Since a triangle wave is used, the operation framerate of the system is twice that of the galvano scanning frequency.

The forward and reverse direction of the mirror results in valid spectral images that are mirror images of each other. An extra post-processing step is required to utilize the reverse direction. However, we only used the forward direction in generating our images.

The setup of the system's driving electronics is shown below (Fig.7.1.). A function generator is used to generate the driving sinusoidal signal to the grating scanner. A synchronized pulse which coincides with the start of the optical scan line is generated for every period. This pulse is sent both to the data acquisition as well as the function generator generating the triangle waveform for the galvano-mirror. The position feedback signal of the galvano-mirror is read by the acquisition system. Thus, three signals in total are acquired: a triggering pulse from the grating scanner driving signal, a position feedback from the galvano-mirror and the intensity signal from the PMT. The first provides the spatial information, the second the spectral information for each acquired data and lastly the intensity readings. The information is then downloaded to be post-processed by a computer.

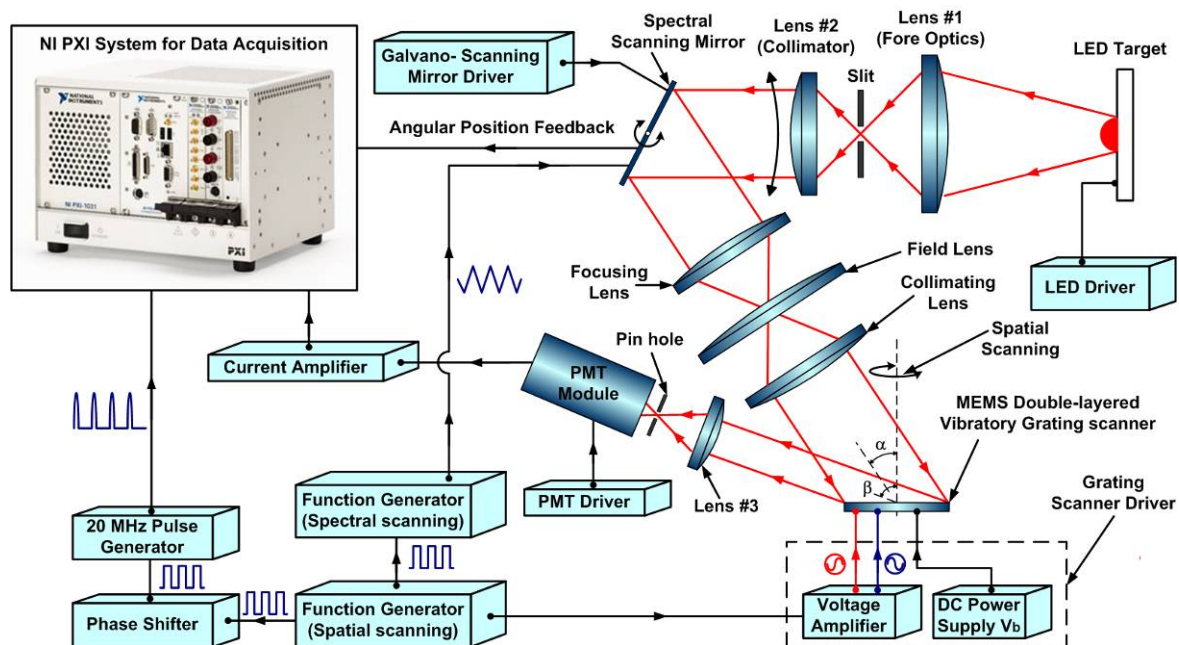


Figure 7.1. Schematic showing all the electronics involved in the operation, synchronization and data acquisition of the spectral imaging system.

The PMT module outputs a current that is proportional to the incident intensity. A highspeed current amplifier is required to convert the current values to a voltage to be read by the data acquisition system.

A National Instruments PXI system is used to collect the system's data in real-time. The DAQ is capable of handing 15Mega-samples/s, more than sufficient for our requirements. A GUI was created to assist in the overall data acquisition as well as in the optical alignment process which we will explore later.

## 7.2. Optical System Setup

The image showing the whole optical setup is shown below in Fig.7.2. The components in the optical system can be correlated to the earlier schematic diagram.

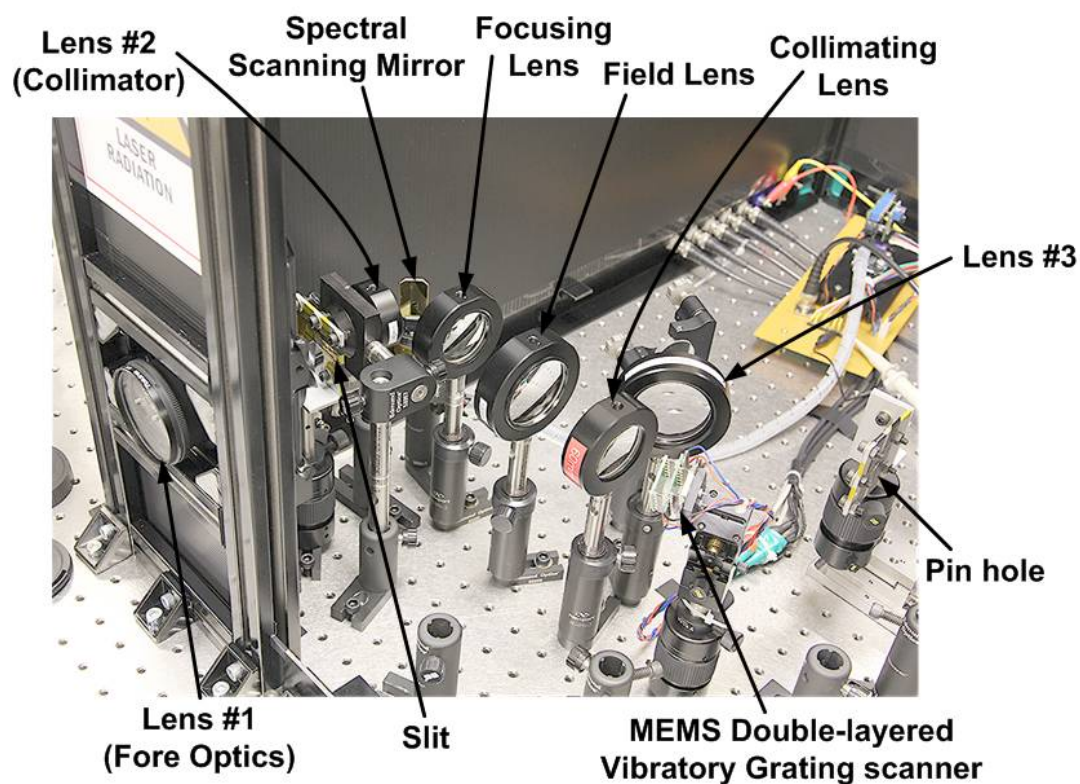


Fig.7.2. Picture of the optical system aligned on an optical isolation table with one side of the enclosure removed.

The slit and pin holes directly affects the optical performance of the system.

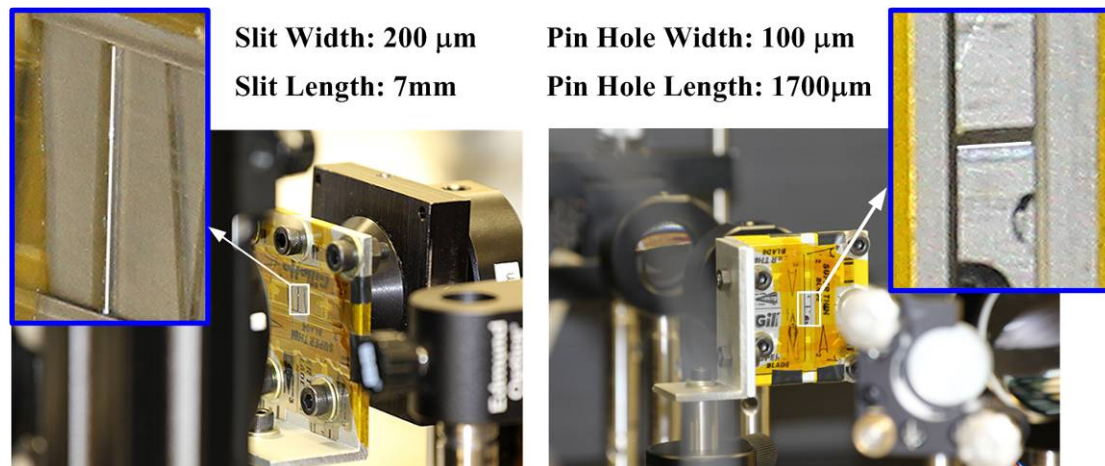


Figure 7.3. Photographic image showing the (a) imaging slit and (b) rectangular pinhole.

Fully implemented, the system's performance was calculated based on the optical model. Fig.7.4. below shows the achievable spectral image based on a simulated lower resolution in order to illustrate the data distribution clearly.

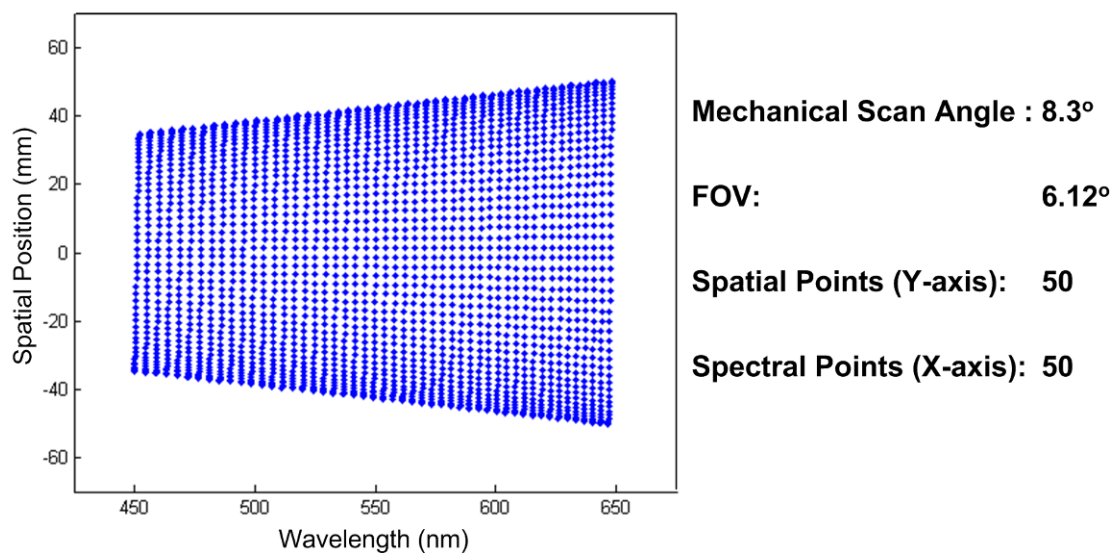


Figure 7.4. Visual representation of the spectral image characteristics simulated at fewer data points.

The optical system was aligned to enhance the quality and accuracy of the acquired signals. As compared to the previous embodiment, a couple of parameters were changed. A

key modification was an increase in the angles  $\alpha$  and  $\beta$  in the optical system alignment, resulting in greater dispersive angles in the wavelengths reaching the PMT detector. This essentially resulted in a narrower wavelength band able to pass through the pin hole and a higher number of resolvable spectral bands. Fig.7.5. below shows the calculated overall system performance.

## System Parameters

Grating Diameter: 2mm  
Grating Pitch: 400nm  
Mechanical Rotation Angle:  $16.7^{\circ}$   
Angle  $\beta$ :  $78^{\circ}$

Spectral Range: 440nm to 650nm  
Angle  $\alpha$ :  
 $7.0^{\circ}$  (440nm)  
 $40.3^{\circ}$  (650nm)

Focal Length:  
Lens #1: 55mm; Lens #2: 40mm;  
Lens #3: 150mm; Lens #4: 40mm;  
Lens #5: 100mm; Lens #6: 40mm;

Slit Dimension:  
 $x_2 = 196\mu\text{m}$ ;  $y_2 = 6.6\text{mm}$ ;  
Pinhole Dimension (rectangular):  
 $x_3 = 100\mu\text{m}$ ;  $y_3 = 1.7\text{mm}$ ;

Spatial Scanning:  
Grating Scan Rate: 21295Hz;  
Optical Scan Angle:  $10^{\circ}$ ;  
Waveform: Sinusoidal;

Spectral Scanning:  
Mirror Scan Rate: 100Hz;  
Optical Scan Angle:  $33.3^{\circ}$ ;  
Waveform: Triangular;

## System Performance

Operation Mode: Pushbroom;  
Spectral Band: 450nm to 650nm;  
Spectral Resolution: 0.94nm;  
Spectral Band: 212;

Frame Rate: 200Hz;  
Spatial Resolution: 250 pixels  
Ground resolution @ 495mm: 0.2mm  
Field of View (FOV):  $6.11^{\circ}$

Figure 7.5. Summary of new system parameters and the predicted performance.

### 7.2.3. Optical Alignment and Calibration

Alignment of the system involved the optics, slits, galvano mirror, grating scanner and the PMT detector with a known wavelength beam of light. A red 635nm laser diode was used in this situation. The diode is positioned approximately in the center of the field of view. During the alignment stage, the galvano mirror is electronically given the appropriate voltage to direct the wavelength band through the slit to be picked up by the detector. The laser diode



is also used as a reference signal to verify the data acquisition process. We also take the opportunity here to illustrate how the image is processed in each step. Fig.7.6. below shows the laser diode setup for alignment purposes.

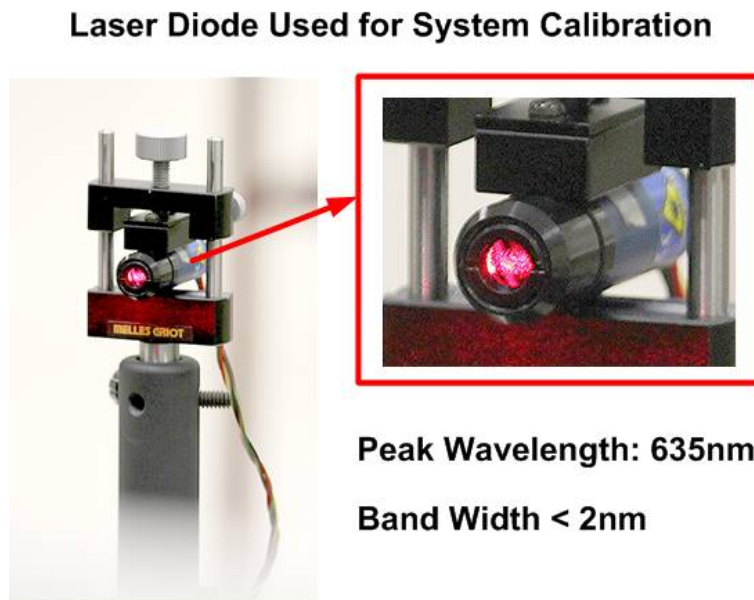


Figure 7.6. Picture showing the red laser diode being used to calibrate the system and the inset shows the close-up view

The initial optical alignment is performed with the laser diode positioned close to the center of the object plane. In this scenario, the grating scanner is at rest. Knowing that the diode's wavelength is 635nm, the only adjustment necessary is for the galvano-mirror to be rotated to the correct angle and all the optical components are aligned to allow the subsequent beam to reach the detector. When that is achieved, the optical system is considered aligned.

When positioning the sample object, the fore-optics is once again adjusted to ensure the image plane is located at the first slit. The laser diode is moved back into place without changing the fore-optics to perform the subsequent image calibration.

With the laser diode in place, the acquisition system is operated to capture a single

frame. An unprocessed, initial raw data is reconstructed as a spectral image in Fig.7.7. below, with a close-up into the region showing the profile of the diode's spectral image.

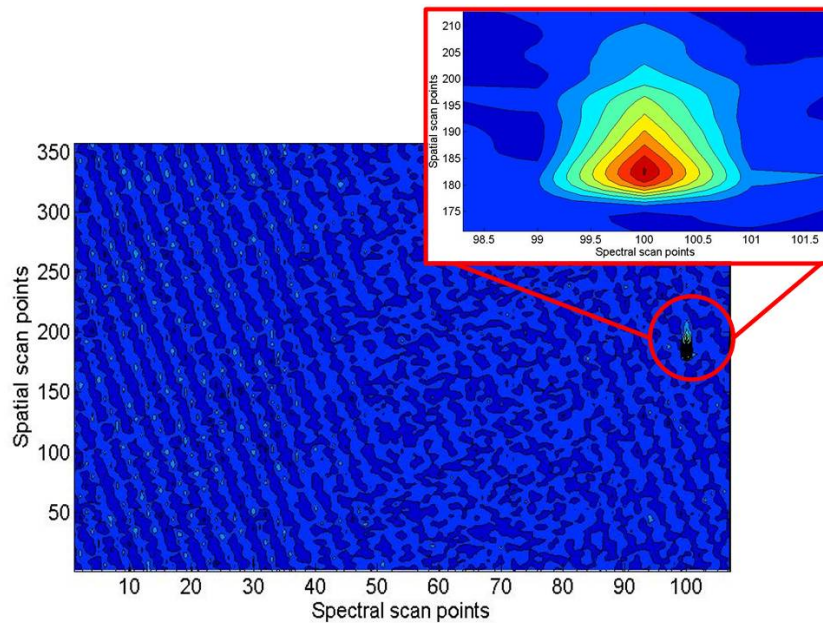


Figure 7.7. Picture showing the raw data map

Taking into account the keystone and smile aberrations through the optical model established earlier, the true spectral image when the individual points are correlated to its actual location in the spectral image plane, results in the distorted image Fig.7.8. below. The zoomed in profile of the laser spot is shown inset.



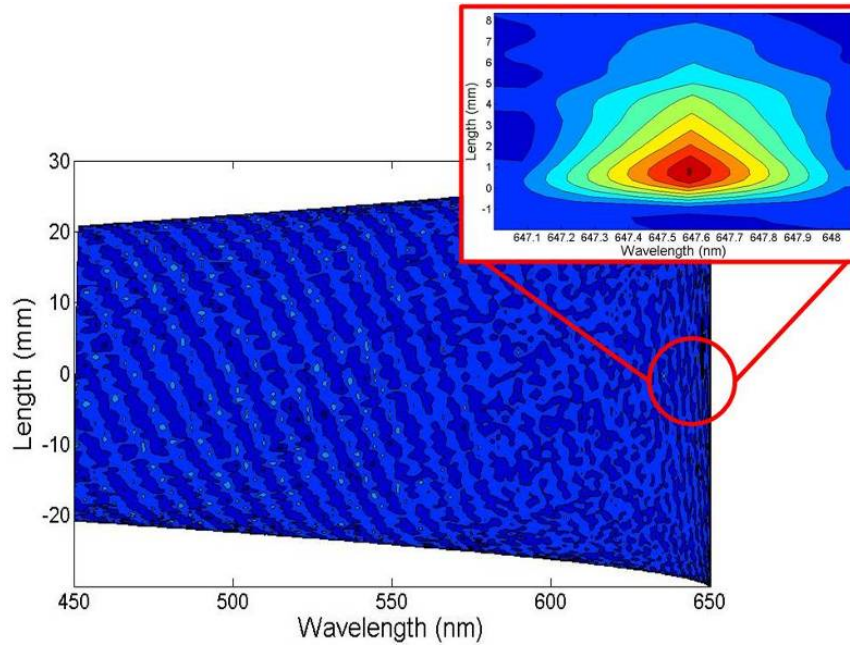


Figure7.8. Picture showing the data points being mapped to its spatial and spectral locations

In this distorted spectral map, the actual points distribution are not linear. However, we can see that the predicted spectral resolution ( $\sim 2\text{nm}$ ) and accuracy ( $635\text{nm}$ ) is not far off.

To obtain the Cartesian map, we utilized the Delaunay Triangulation methodology discussed earlier to obtain the final reconstructed spectral image in Fig.7.9.

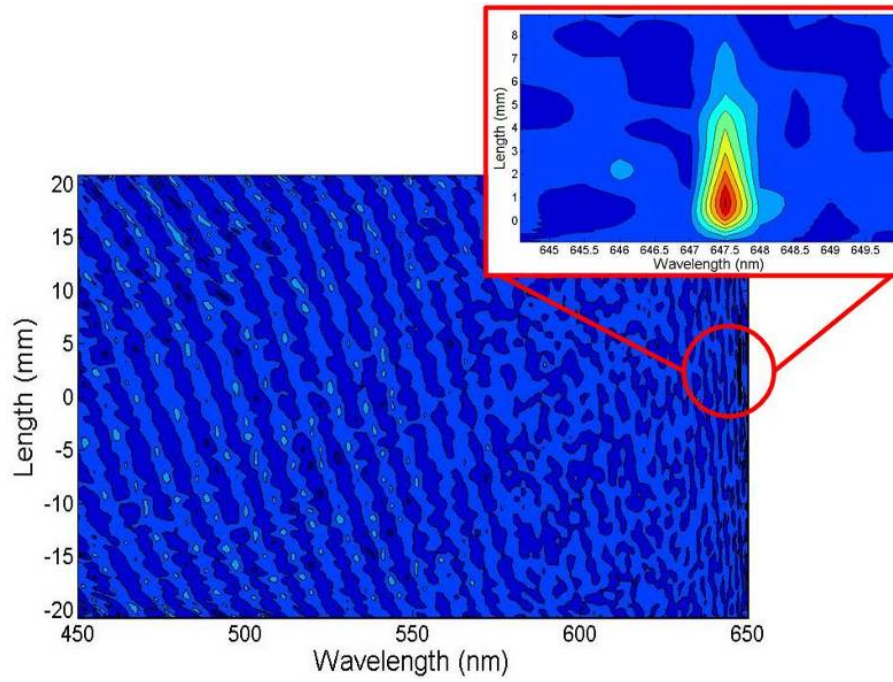


Figure 7.9. Picture showing the final distortion corrected Cartesian spectral map

Although the system's performance can be theoretically calculated, slight systematic errors like misalignments in the optical system can occur. To compensate, the known wavelength for the laser diode was used as the reference. With the known diode wavelength at 635nm, we recalibrated the algorithm for the subsequent actual signal processing. Fig.7.10. shows the recalibrated spectral image.

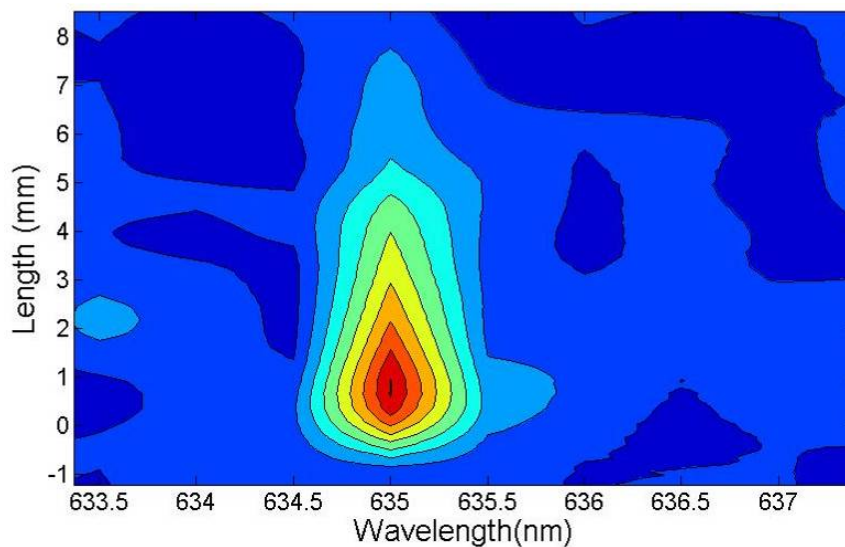


Figure 7.10. Picture showing the recalibrated system based on the 635nm red laser diode

Though more can be done to calibrate the system in terms of intensity, tilt and spatially, we can consider the reconstruction algorithm sufficiently accurate. Subsequent reconstruction processing that followed used the same algorithm as mentioned here.

To illustrate both the accuracy of the modelling as well as to characterize the performance of the system, more detailed series of measurements were made. From the modelling, we attempted to verify the two main performance parameters predicted for the system: spectral resolution and spatial resolution.

In order to verify the predicted system performance, more precise targets to be imaged is necessary. Ideally, different wavelengths should be tested across the spatial locations. To verify a predicted spectral resolution of 1.92nm would require lasers for such a narrow band. We used two lasers, one red at 632.8nm and another green at 532nm. For the spatial points, a visible wavelength range single-mode optical fiber of diameter 4um was used as that will be much smaller than the predicted spatial resolution. The optical fibre is placed at a distance of about 470mm away from the fore-optics of the imaging system. In order for subsequent testing for the spatial and spectral resolutions at various points in the field-of-view, the optical fibre is mounted on stages able to move along the FOV (vertically) as well as laterally across the FOV (horizontally).

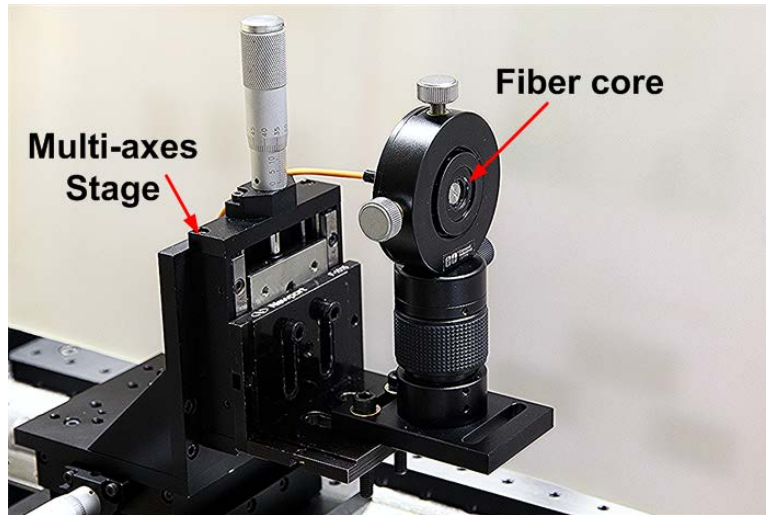


Figure 7.11. Picture showing the single-mode visible wavelength optical fiber with the stage assembly

Acquisition wise, in order to demonstrate the spatial resolution of the system, for 250 spatial points and operating at about 20kHz spatial scanning frequency in a single directional scan, we require a detector that has a bandwidth of at least 10 MHz. A Hamamatsu APD was used in this case. The ADC in the NI acquisition system has about 15 MHz sampling rate, which is sufficiently high.

Lasers have very narrow bandwidths, typically in the 1nm range. Thus it's ideal to use it to demonstrate the spectral resolution of the system. In our test, we separately coupled two different laser wavelengths into the fibre.

The first test is to locate the fibre at the center of the FOV. The two lasers were coupled into the fibre and a spectral map is obtained individually. The figures below show the results.

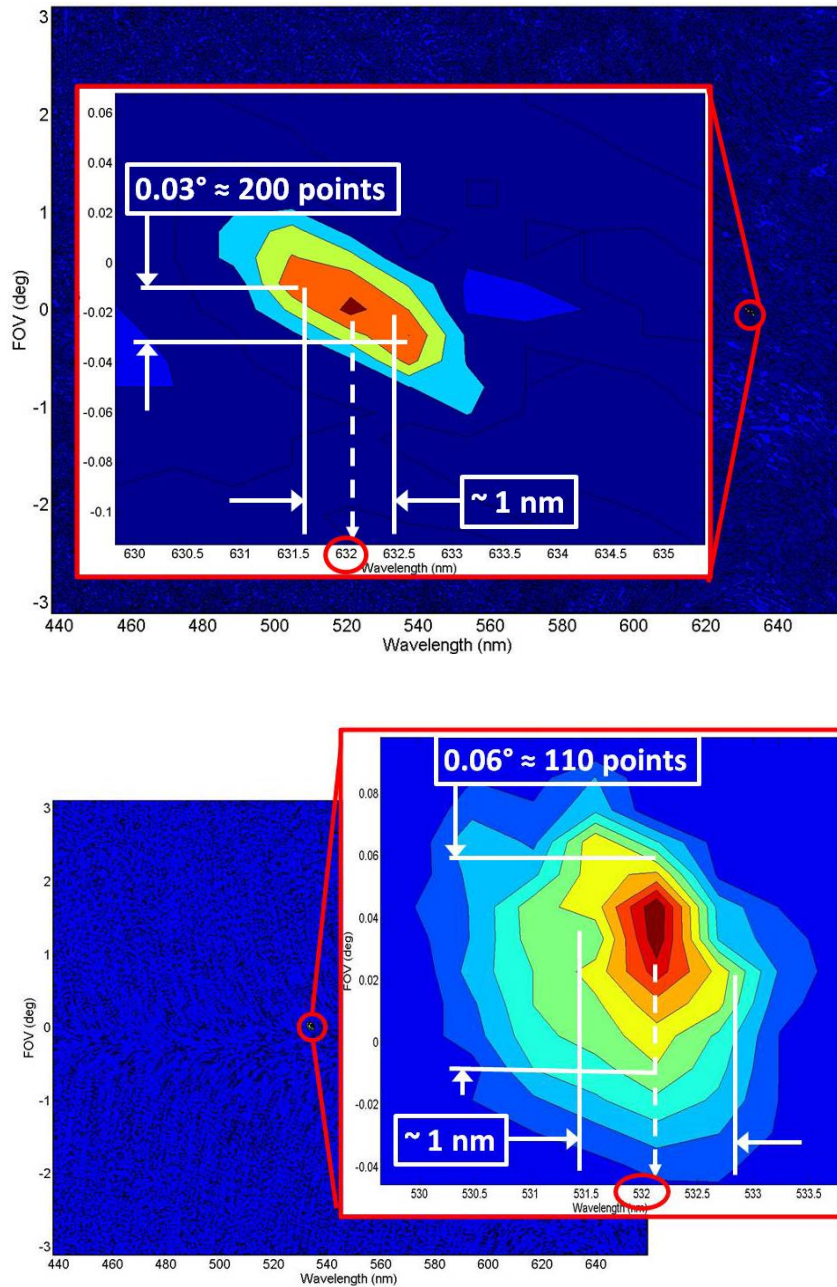


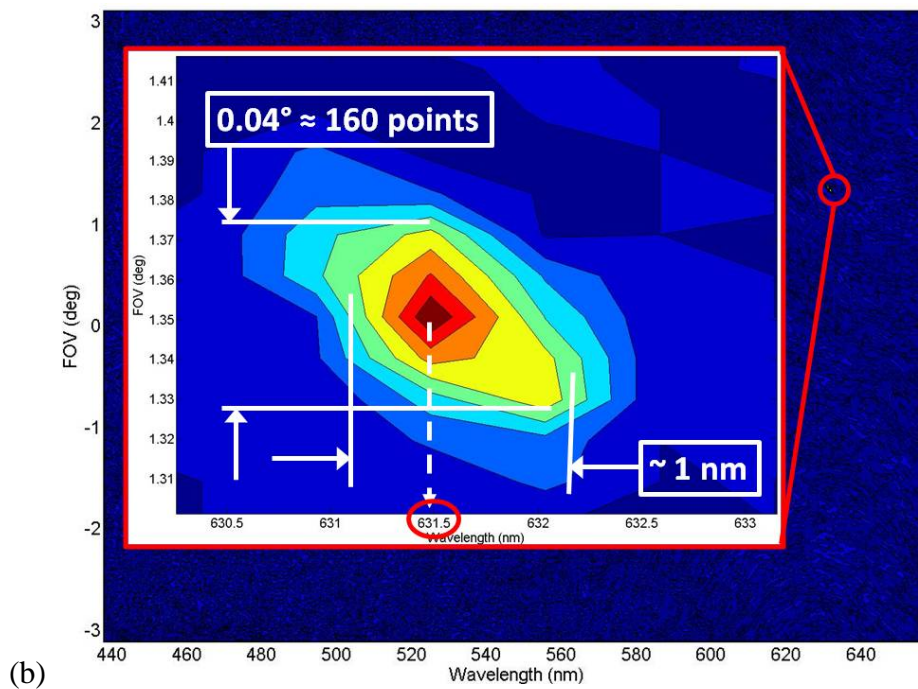
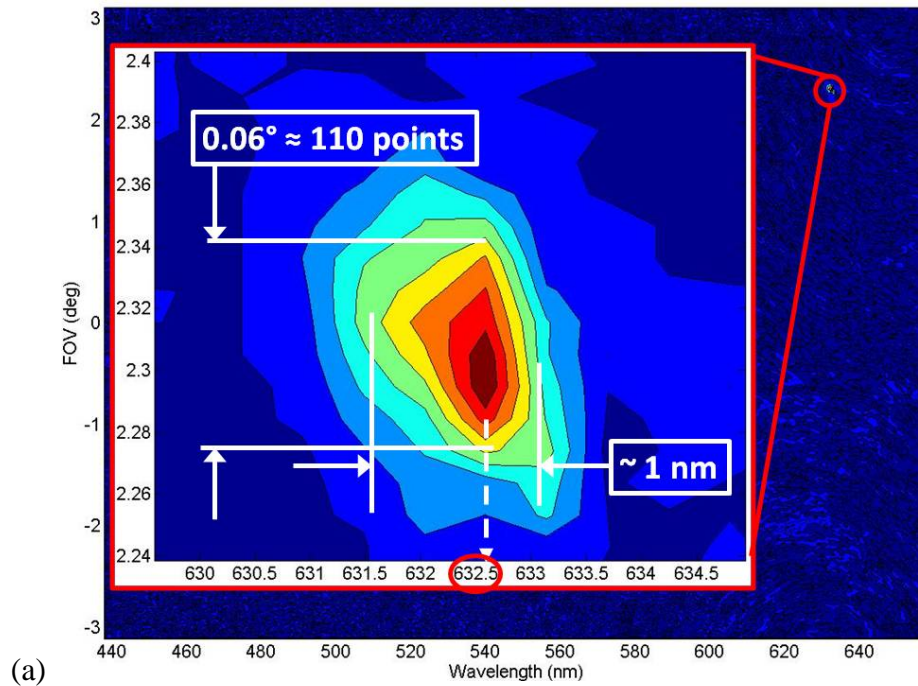
Figure 7.12. Figure showing the post-processed spectral image for red (top) and green (bottom) lasers

Both results demonstrate the accuracy of the predicted system performance with about 1nm wavelength band for each laser. In terms of the spectral accuracy, we obtained about 632nm for red and 532nm for green which is fairly consistent to the actual wavelengths of the lasers used.

To verify the spatial resolution and accuracy across the field of view, we moved the



optical fibre vertically up and down and collated the results to calculate the spatial resolutions. At the object distance of 470mm, we moved the optical fibre both up and down 10 and 20 mm each for a total of 4 sample points for each wavelength. The figures below demonstrate the results of the processed data for the red laser.



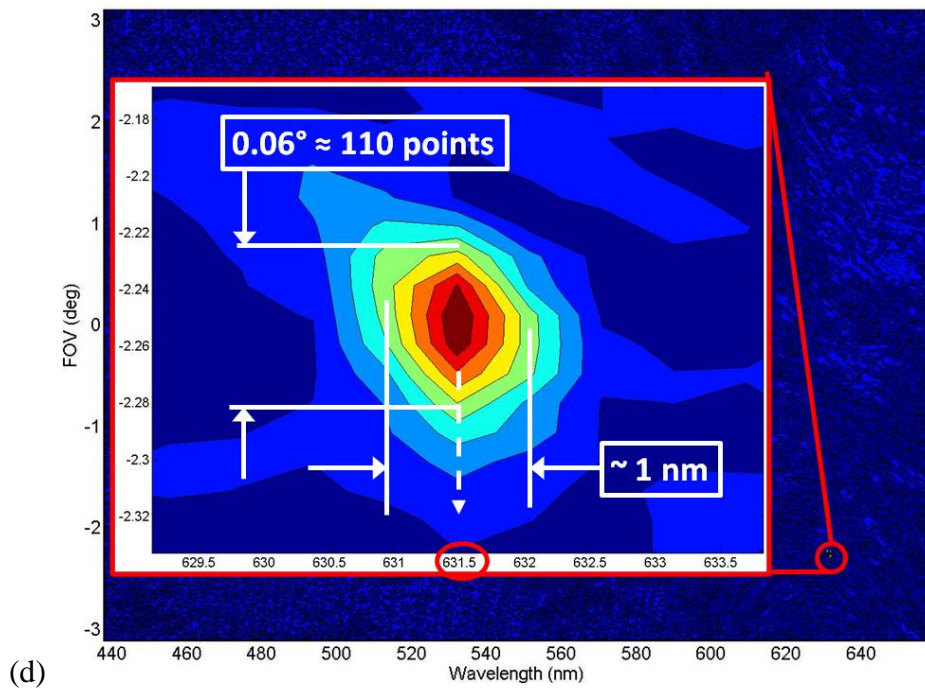
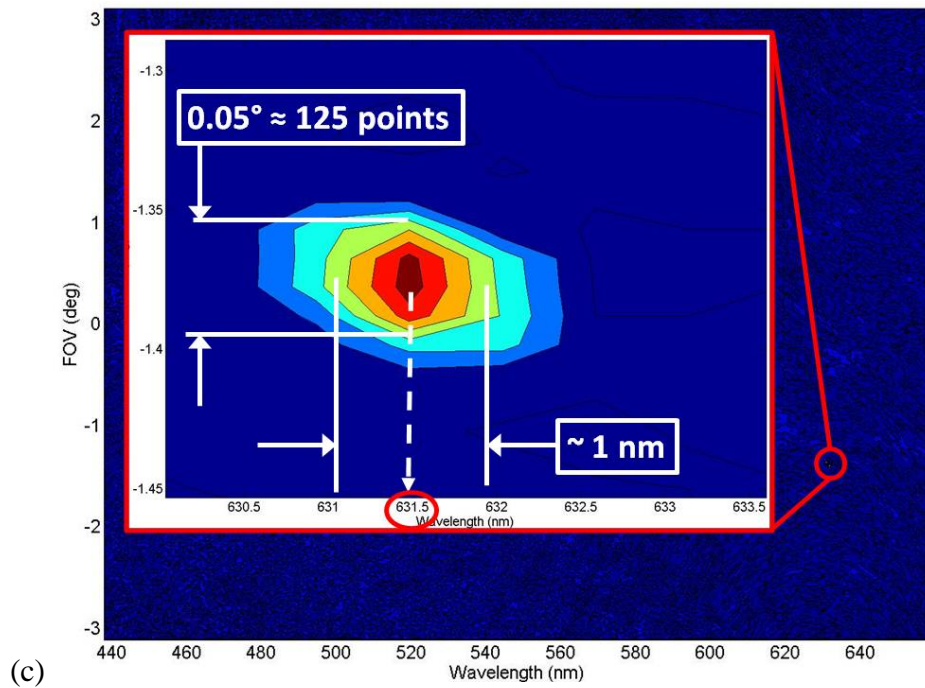


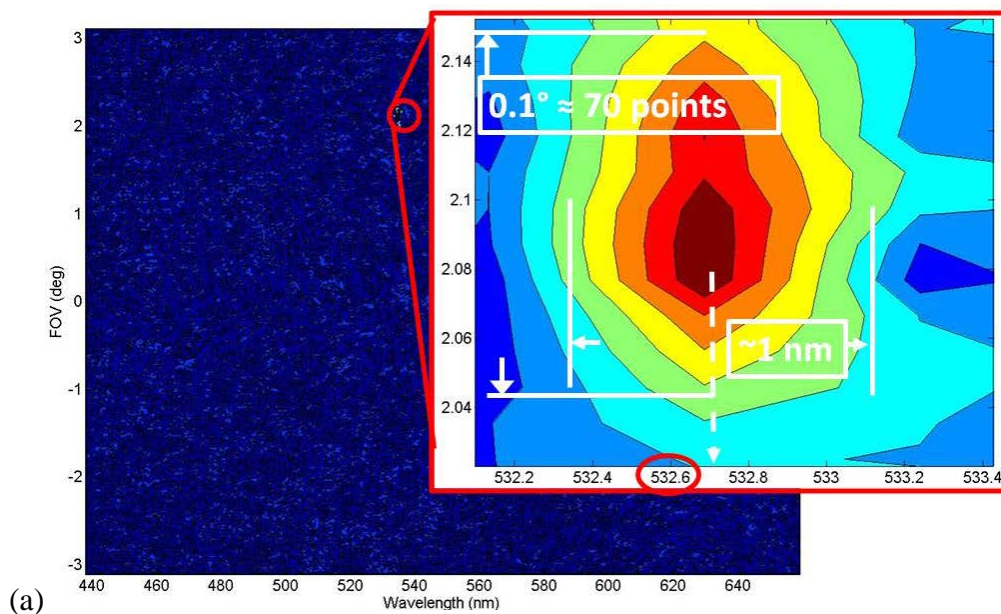
Figure 7.13. Figures showing the acquired images for 632.8nm red laser from (a) 20mm up, (b) 10mm up, (c) 10mm down and (d) 20mm down

Two key observations can be made from these series of images. By measuring the FWHM for each spot, some loss in spatial resolution can be observed. However, the spectral

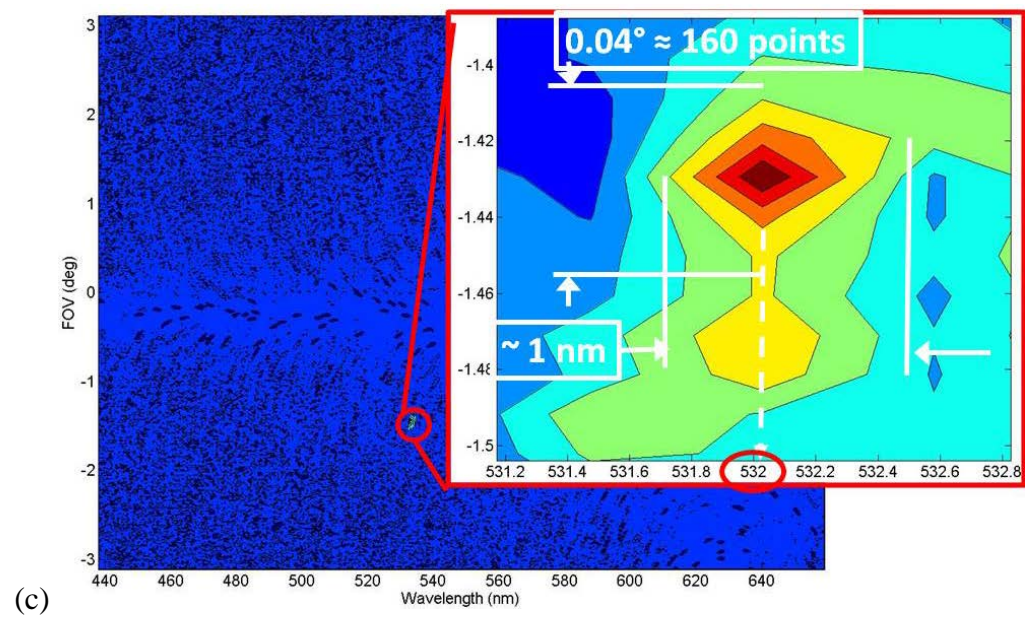
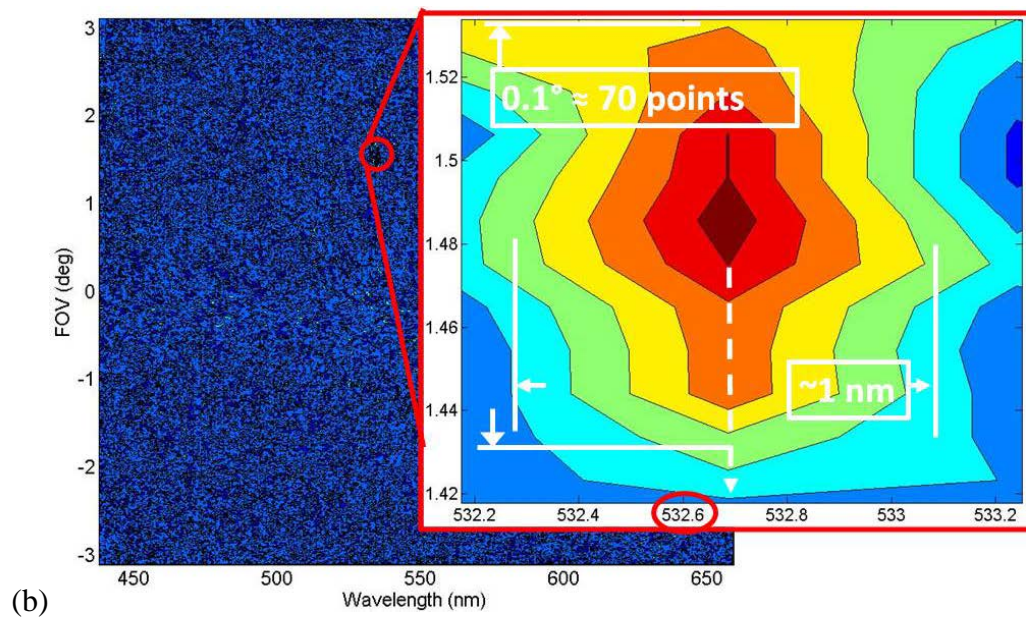
resolution consistently maintained across the FOV at about 1nm. The loss in resolution can be attributed to the focusing range that we are currently working on. The optical system was calibrated based on a collimated laser beam source, which accurately simulates real-life implementation where the object is far away from the imager. In our case however, the laser diode is only placed about 4-5 times of the focal length of the fore-optics, which means that the acquired image may not be well focused one. A completed real-time system will be able to correct for such off-focus if the images can be post-processed and displayed in real-time. The focusing can then be done by viewing the acquired image.

By looking at the location of the beams, the accuracy of the spatial location can also be determined. Each movement is a 10mm step. With the distance at about 470mm, the location of the beams spots in the FOV is about  $\pm 1.22^\circ$  and  $\pm 2.44^\circ$ . This corresponds well to the reconstructed images we obtained.

A similar series of data was acquired by switching the laser source to green. The following figures shows the results obtained.







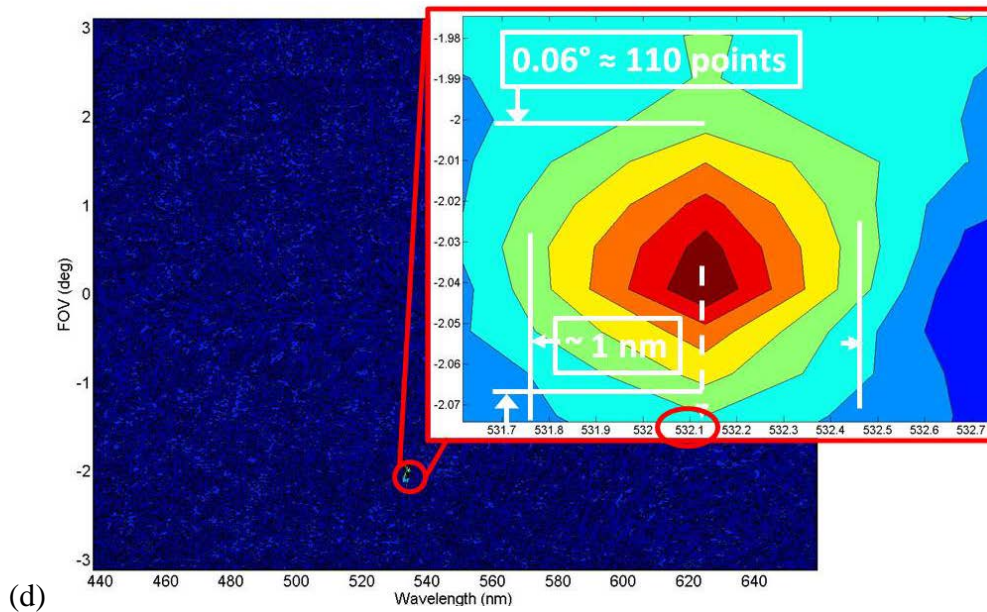


Figure 7.14. Figures showing the acquired images for 532.8nm green laser from (a) 20mm up, (b) 10mm up, (c) 10mm down and (d) 20mm down.

As is the case with the red laser, the spectral accuracy is also well maintained in our results, with spectral resolution remaining at about 1nm range. The wavelength obtained is also maintained at about 532nm throughout the FOV. The spatial resolution also achieves close to about 100 points across the FOV, the performance being not as good as the red laser above.

#### 7.2.4. Sample Target and Enclosure

To demonstrate the system, a sample object was created for image acquisition. This object is essentially 2 different LEDs arranged in a line on a PCB. The peak wavelengths are blue (462nm) and green (528nm). The wavelengths of the LEDs are selected to cover the full spectral capability of the designed system as far as possible. Fig.7.15. below shows the LED profile used for the image acquisition as well their respective spectral characteristics. The LEDs are located 20.5mm apart with the overall size of the LED at about 12.9mm.

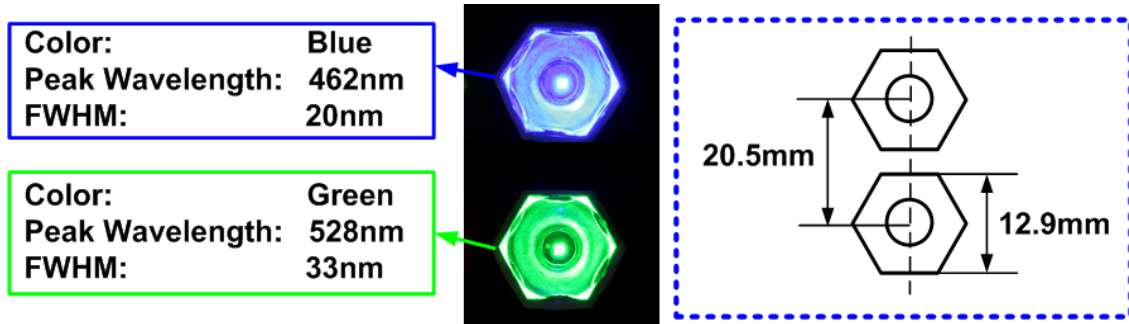
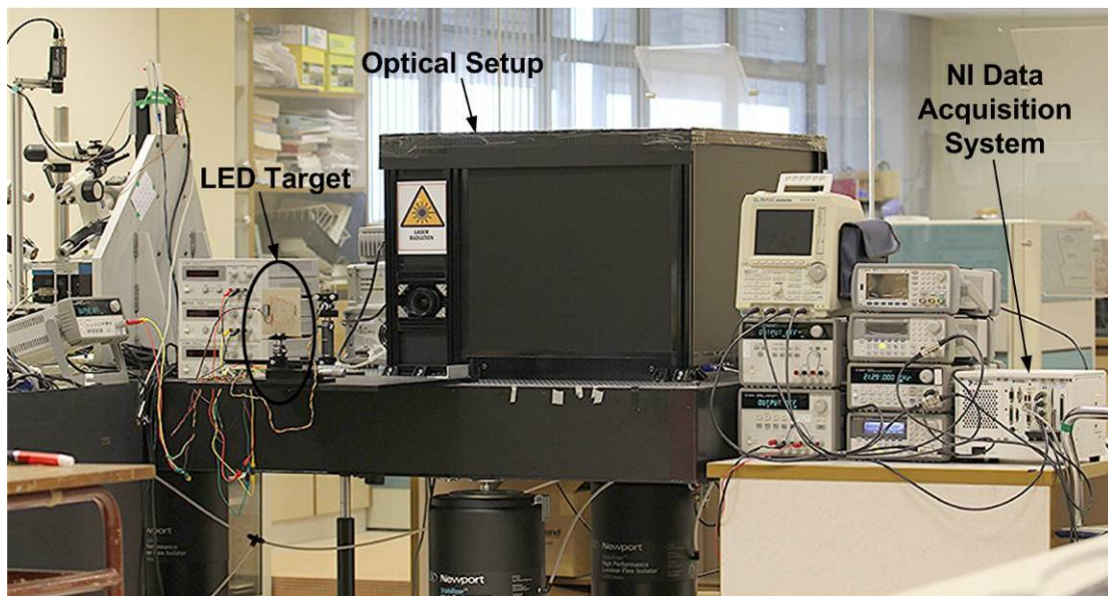


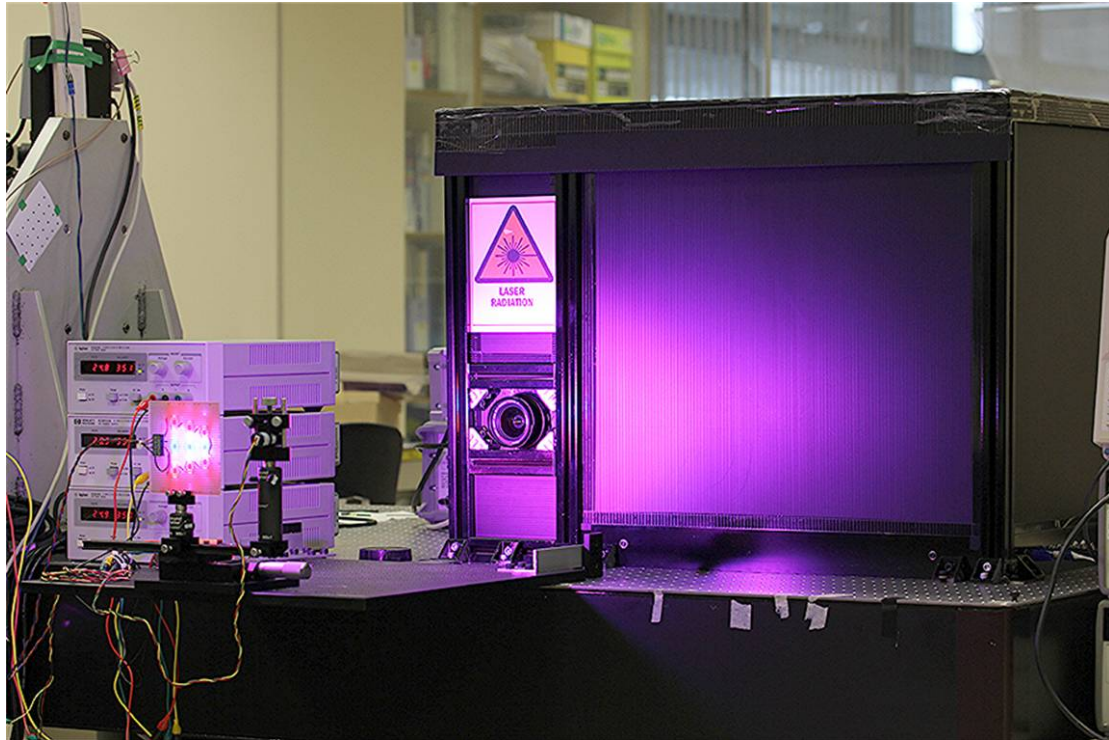
Figure 7.15. Photograph and parameters of the LED target;

To minimise the noise from the environment, a special enclosure was prepared for this system. All the optical components were setup on an optical isolation table to minimise vibration during testing. The enclosure was designed to be modular and easily removable for optics alignment purposes yet capable of minimising stray light from entering the enclosure. The complete setup with the enclosure and all the electronic equipment utilized is shown below in Fig.7.16.



(a)





(b)

Figure 7.16. (a) Picture of the complete enclosure and all the electronic instruments used in the operation and testing of the system. (b) Picture showing setup when illuminated by the LED array.

The resulting system after calibration operated at a spectral range of between 440nm to 660nm, and at a frame rate of 200Hz with a FOV of  $6^\circ$ . The optical system was calculated to obtain a theoretical spectral resolution of 1.92nm and a spatial resolution of 250 points. Operating at 15Mega-samples/s therefore oversamples the raw data map but that's intended to also compensate for the expected scanning acquisition time available at the center of the map as well as the loss of data points due to keystone correction.

The corrected spectral map of the LED target is shown in Fig. 7.17.

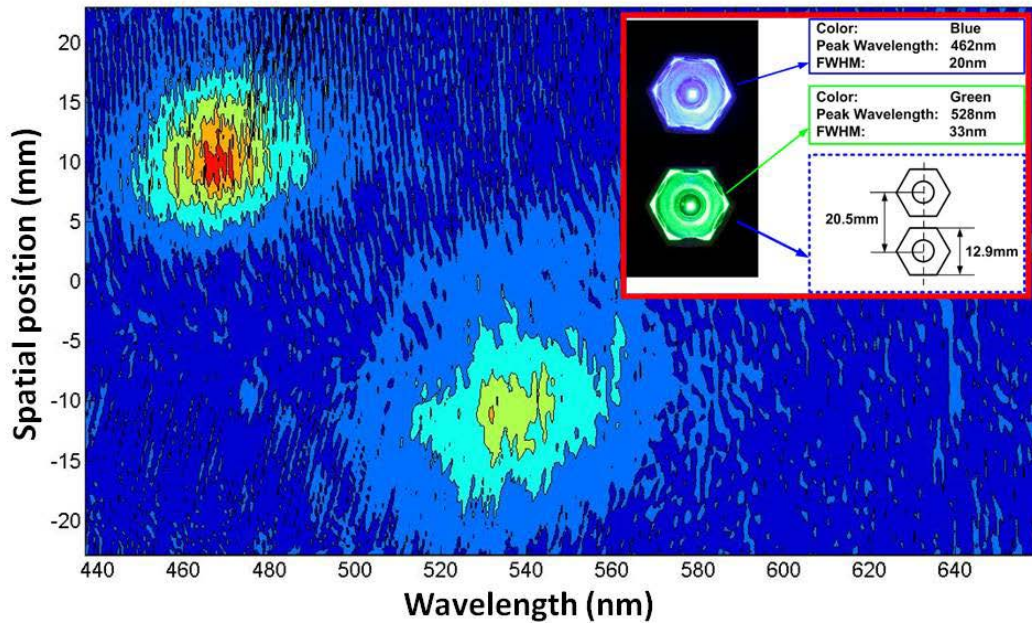


Figure 7.17. Corrected hyperspectral image of the LED target.

The spectral and spatial points of both LEDs can be seen to be well-correlated with the physical targets. Fig. 7.18. below shows another visualization of the spectral map.

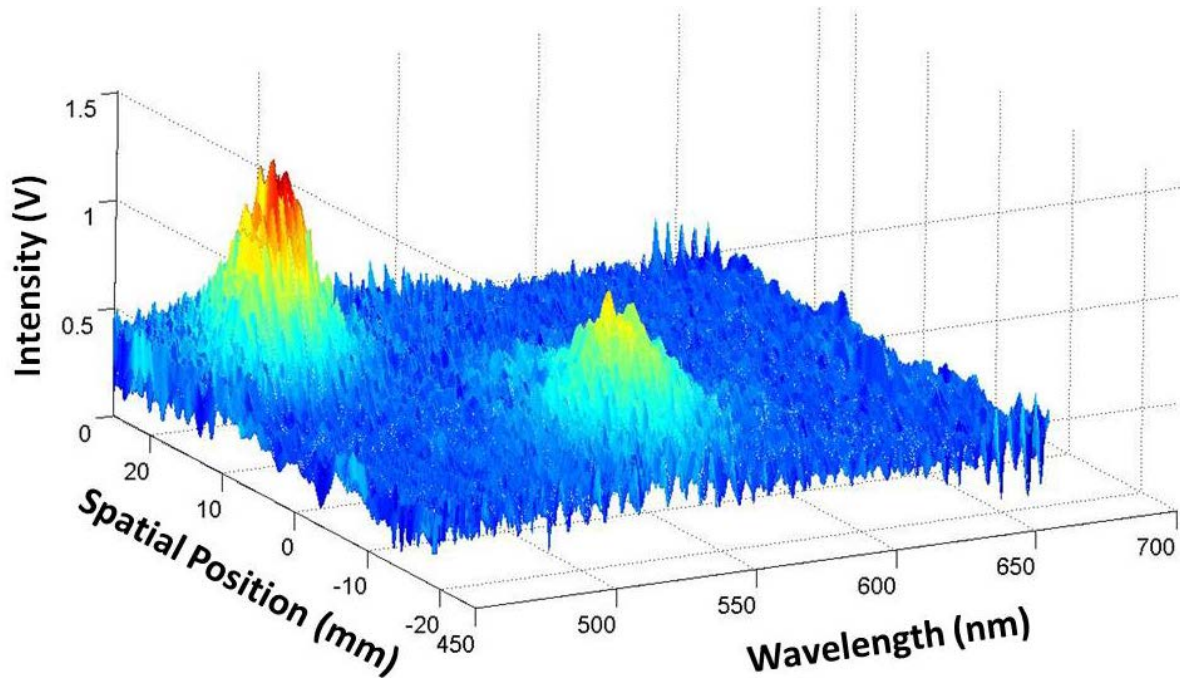


Figure 7.18. Intensity map image of the LED target.

The expected spectrum for the LEDs obtained from their respective datasheets was

compared to the acquired spectrum in Fig.7.19. As can be seen, the wavelengths of the LEDs and their relative positions were accurately identified by the system, which proves the validity of the post-correction algorithm. The small discrepancy is probably due to the system's misalignment and the LED manufacturing imperfections since we used the datasheet's theoretical value as comparison.

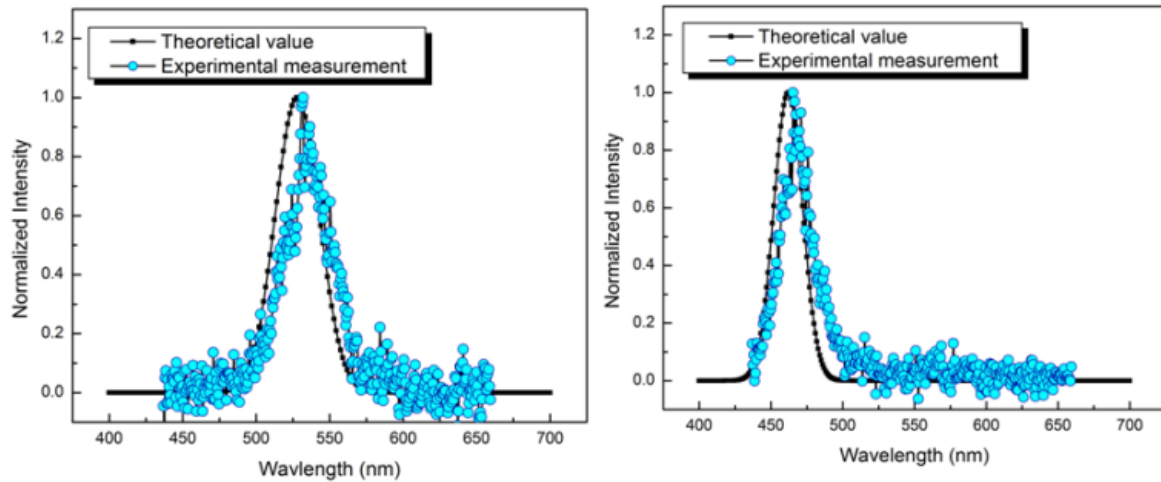


Figure 7.19. Comparison of LEDs expected datasheet spectrum and acquired spectrum for (Left) green LED and (right) blue LED.

The resulting system demonstrated the viability of utilizing the dispersive properties of the grating scanner as a spectral discrimination system. High-frequency scanning capability would allow higher image resolutions. However, as scanning speed increases, the integration time per pixel decreases. This would potentially affect the signal-to-noise ratio for low-light applications. To increase the signal strength, it is then necessary to increase the light collection capacity of the grating scanner. The effective aperture size of the grating scanner is essentially the size of the grating platform. There are two main approaches which the aperture size increase can be achieved.

It could be done on a device level: designing a larger grating platform on the device. A double-layer grating device can achieve this easily. However, a larger platform basically

means having a larger mass which lowers the resonance frequency of the device. Depending on the system requirements, high resonance frequencies might not be necessary and lowering the resonance frequency may not be a negative point. The current system operates at 200Hz framerate which may or may not be useful, depending on the application. The resonance frequency of the grating scanner essentially determines the number of spectral lines that can be scanned per second. Lowering the resonance frequency of the device will be helpful to increase the integration time per pixel.

A second approach is to synchronize multiple grating scanners to achieve a synthetic aperture. In this way, a larger overall aperture is achieved. The difficulty in this approach lies in requiring an integrated positioning feedback mechanism on each grating scanner and utilizing it to synchronize individual driving circuitries to ensure all the devices actuate with the same phase and amplitude. Manufacturing tolerances between devices adds to the complexity of the problem.

## 8. Conclusion

The development of miniaturized high-speed optical scanning devices has been opened up several unique applications, like optical communications, micro projectors and miniature confocal endoscopes. These developments take advantage of micro devices' key characteristics of high-frequency operation, low-cost and miniaturization capabilities. High-frequency operation, large scanning range and high-resolution often results in conflicts in terms of design. Fundamentally, the out-of-plane rotation of mirror-based optical scanners results in significant dynamic deformation of the mirror surface at high-frequencies and amplitudes. The necessity to balance between the performance specifications limits the potential applications that micromachined devices are capable to explore.

The development of an in-plane vibratory grating scanner was intended to resolve this issue. Initial developments focused on improving the optical efficiency of the grating scanner. Through careful design of the grating, optical efficiency of greater than 80% can be achieved. This was verified both through theoretical and experimental results. The next key development was to increase the size of the grating diameter. Simultaneously achieving large optical scan angles and large aperture sizes was possible through the double-layer vibratory grating design. This involves fabricating the grating platform and the actuating resonator separately and post-assembly them. In this manner, a 2-DOF grating scanner with a 2mm diameter aperture capable of an optical scan angle of  $33^\circ$  is achieved.

The grating scanner possesses several unique characteristics that allow it to be utilized in other applications. A key feature is the dispersive nature of its operation. Besides performing scanning, incident light is dispersed into its constituents. It thus possesses the



capability to scan and disperse light at the same time. It is in this regard that we find synergy with spectral imaging applications.

Spectral imaging is a tool which brings together imaging and spectroscopy. An image consisting of continuous bands over a spectral range is acquired and output for a spectral imager. The number of spectral bands determines the spectral resolution of the system. Several different mechanisms exist for acquiring the spectral image, including push-broom and whiskbroom systems. Detectors wise, arrayed detectors such as a line detector or a 2-D detector such as a CCD are common.

Miniaturizing spectral imagers based on arrayed detectors brings its own sets of challenges. Imposing space constraints implies the imaging system has to disperse light at larger angles with smaller pitch gratings in order for the various diffracted spectral bands to be picked up. The higher dispersion angles yet results in distorted spectral distributions which array detectors have difficulty picking up. Moreover, having an array of detectors mean that individual pixel calibration has to be performed to ensure spectral response uniformity. At longer wavelengths, e.g. infra-red range, arrayed detectors are also more expensive and difficult to obtain at high densities.

A single-pixel detector configuration will resolve these issues. No pre-calibration steps need to be done and single-pixel detectors are more easily available over a wide spectral range. High-speed scanners are then necessary to scan through the spatial points and dispersed spectral bands to direct them to the single-pixel detector in order to achieve real-time operation.

A silicon micromachined grating scanner suits the task perfectly. In the first configuration of a line spectral imager, two galvano-mirrors are used to perform the spectral

scanning and the high-speed grating scanner is used to perform the spatial scanning. Two galvano-mirrors are required to achieve bow-free scanning throughout the different wavelengths by controlling the incident and diffracted beams from the grating scanner.

A proof-of-concept line spectral imaging system was demonstrated to be viable based on a proprietary micromachined double-layer grating scanner device. The grating scanner possesses unique characteristics like high-speed operation and light dispersion which can be exploited for novel imaging systems. A model using a ray-tracing method for the spectral imaging system was established to predict the performance and limitations of the system. Data acquired was recognized to require post-signal processing to compensate for keystone and smile artifacts in reconstructing the spectral image.

However, this configuration suffered from a few limitations. Firstly, it was realized that the spectral range of the system is limited due to the need to have two galvano-mirrors. Secondly, the power load of the driving circuitry and size of the galvano-mirrors limits the potential miniaturization of the overall system.

The necessity of having two rotating mirrors was to correct for the smile distortion in the spectral image. With a single rotating mirror, a non-linear relation results between the spatial and spectral bands and the angle of the galvano-mirror and grating scanner. However, it is realized that a model can be established that takes into account these distortions and a mapping algorithm such as Delaunay Triangulation used to correct for them. Post-signal processing takes on a greater load in this configuration as compared to the previous configuration which relies on optical correction. With the advance of today's mobile processing speed, real-time computation is still feasible.

An optical model was established to predict all the sampling points, taking into account the angle of the grating scanner, dispersion angles and the sinusoidal oscillation of the grating scanner. Delaunay Triangulation was used to correct for the distortions and obtain a Cartesian coordinate map of the spectral image. A detailed alignment and calibration process was performed using two different laser wavelengths across the FOV. The process also verifies the accuracy of the optical model and mapping methodology.

Finally, two LEDs of blue and green in colour were used as a sample target to verify the accuracy of the optical system. A spectral image which correctly represented the spectral band of the LED and their respective spatial locations along the FOV was obtained. The cross-section of the spectral profile was also accurately profiled as compared with the manufacturer's datasheet.

Several future developments are possible to fully utilize the capabilities of the grating scanner, primarily in achieving a synthetic aperture system. This entails developing a feedback control system to control both the amplitude and phase of the grating scanner. With a double-layer grating device, resonance frequencies and aperture sizes can be independently design to cater for different specifications. Reducing the current devices' resonance frequency can help to improve the signal-to-noise ratio if necessary.

# References

- [1] K.E. Petersen, "Micromechanical light modulator array fabricated on silicon," Appl. Phys. Lett., 31, pp. 521-523, (1977)
- [2] J.E. Ford, "Optical MEMS: Legacy of the Telecom Boom," Solid State Sensor, Acuator and Microsystems Workshop, Hilton Head SC, June 6-10, pp.1-3, (2004)
- [3] L.J. Hornbeck, "Projection Displays and MEMS: Timely Convergence for a Bright Future," Proc. SPIE-Int. Soc. Opt. Eng., USA, 2639, pp.2 (1995)
- [4] O. Solgaard, F.S.A. Sandejas and D.M. Bloom, "Deformable grating optical modulator," Opt. Lett. 17, pp. 688-690, (1992)
- [5] S.S. Lee, L.Y. Lin and M.C. Wu, "Surface-micromachined free-space fibre-optic switches," Electron. Lett., 31, 1481, (1995)
- [6] D.M. Marom, D.T. Neilson, D.S. Greywall et al., "Wavelength-selective 1xK switches using free-space optics and MEMS micromirrors: theory, design and implementation," J.Lightwave Tech., 23, pp. 1620-1630, (2005)
- [7] H. Toshiyoshi and H. Fujita, "Electrostatic micro torsion mirrors for an optical switch matrix," J. Microelectromech. Syst., 5, 231-237, (1996)
- [8] G. Zhou, L.Vj, F.E.H. Tay and F.S. Chau, "Diffraction grating scanner using a micromachined resonator," IEEE Photon. Tech. Lett. Vol.16, pp.2293-2295, (2004)
- [9] G. Zhou and F.S. Chau, "Micromachined vibratory diffraction grating scanner for multiwavelength collinear laser scanning," IEEE. J. Microelectromech. Syst., 15, 1777-88

- [10] G. Zhou, Y. Du, Q. Zhang, H. Feng and F.S. Chau, "High-speed, high-optical-efficiency laser scanning using a MEMS-based in-plane vibratory sub-wavelength diffraction grating," J. Micromech. Microeng., 18, (2008)
- [11] Y. Garini, I. T. Young, and G. McNamara, "Spectral imaging: principles and applications," Cytometry 69A, 735 (2006).
- [12] Willoughby, C.T, Folkman, M.A, and Figueroa, M.A., "Application of hyperspectral imaging spectrometer systems to industrial inspection," Proc SPIE, Vol.2599, pp.264-272, (1996)
- [13] F.A. Kruse, "Mapping spectral variability of geologic targets using Airborne Visible/Infrared Imaging Spectrometer (AVIRIS) data and a combined spectral feature/unmixing approach," Proceedings of SPIE's International Symposium on Aerospace/Defense Sensing & Control and Dual-Use Photonics, Vol. 2480, No.18, Orlando, FL, April 17-21, (1995)
- [14] R.G. Sellar, G.D. Boreman, "Classification of imaging spectrometers for remote sensing applications", Optical Engineering, 44(1), Jan (2005)
- [15] P. Mouroulis, R.O. Green, T.G. Chrien, "Design of pushbroom imaging spectrometers for optimum recovery of spectroscopic and spatial information", Appl. Opt. , vol.39, no. 13, 1 May (2000)
- [16] P. Mouroulis, M.M. McKerns, "Pushbroom imaging spectrometer with high spectroscopic data fidelity: experimental demonstration", Opt. Eng. 39(3), Mar, pp. 808-816, (2000)
- [17] L. Beiser, Holographic Scanning, New York: Wiley, (1988)

- [18] J. Tsai and M. C. Wu, "Design, Fabrication, and Characterization of a High Fill-Factor, Large Scan-Angle, Two-Axis Scanner Array Driven by a Leverage Mechanism", IEEE/ASME Journal of Microelectromechanical Systems, Issue 5, 15 pp. 1209-1213, (2006)
- [19] I. W. Jung and U. Krishnamoorthy and O. Solgaard, "High Fill-Factor Two-Axis Gimbaled Tip-Tilt-Piston Micromirror Array Actuated by Self-Aligned Vertical Electrostatic Combdriives", IEEE/ASME Journal of Microelectromechanical Systems, Issue 3, 15, pp. 563-570, (2006)
- [20] Descour, M.R. and Dereniak, E.L., "Nonscanning no-moving-parts imaging spectrometer," Proc of the SPIE, Vol 2480, pp.48-64, (1995)
- [21] Descour, M.R. and Dereniak, E.L., "Computed tomography imaging spectrometer: experimental calibration and reconstruction results" Applied Optics, Vol.34. No.22, pp4817-4826, (1995)
- [22] T.Sandner, H. Conrad, T. Klose, and H. Schenk, "Integrated Piezo-resistive Positions sensor for Microscanning Mirrors", IEEE/LEOS int. Conf. on Optical MEMS, pp. 195-196, 2007
- [23] H. Kamoda, H. Goto, K. Imanaka, "Two-dimensional optical position sensor using a dual axis miniature optical scanner", SPIE vol 1751, pp 280-288, (1993)
- [24] Carter, M.R., Bennett C.L. Fields, D.J., Lee, F.D. , "Livermore Imaging Fourier Transform Infrared Spectrometer," SPIE vol.2480, pp380-386, (1995)
- [25] Otten, L.J., Butler, E.W., Rafert, J.B and Sellar, R.G. , "The design of an airborne Fourier transform visible hyperspectral imaging system for light aircraft environmental remote sensing," SPIE, Vol.2480, pp418-424, (1995)
- [26] M. F. Duarte, M. A. Davenport, D. Takhar, J. N. Laska, T. Sun, K. F. Kelly, and R. G. Baraniuk, "Single-pixel imaging via compressive sampling," IEEE Signal Processing Magazine, 83 (2008).

- [27] S. Lertrattanapanich and N.K. Bose, "High resolution image formation from low resolution frames using Delaunay triangulation" IEEE Transactions on Image Processing, Vol. 11, No. 12, pp. 1427-1441, (2002).
- [28] Fisher, J., Baumbach, M., Bowles, J., Grossmann, J. and Antoniadis, J. "Comparison of low-cost hyperspectral sensors," SPIE, vol. 3438, pp.23-30, (1998)
- [29] Y. Du, G. Zhou, K.L. Cheo, Q. Zhang, H. Feng and F.S. Chau, "Double-layered vibratory grating scanners for high-speed high-resolution laser scanning," IEEE Journal of Microelectromechanical Systems, Vol. 19, No. 5, pp. 1186-1196 (2010).
- [30] G. Zhou, K. Cheo, Y. Du, F. Chau, H. Feng, and Q. Zhang, "Hyperspectral imaging using a microelectrical-mechanical-systems-based in-plane vibratory grating scanner with a single photodetector," Opt. Lett. 34, 764-766 (2009).
- [31] Y. Du, Kelvin K.L. Cheo, G. Zhou and F.S. Chau, "A Spectral Line Imager Based On A MEMS Vibratory Grating Scanner" IEEE/LEOS International Conference on Optical MEMS and Nanophotonics, pp. 210-211, (2012).
- [32] Tominaga, S., Takahashi, E. "Spectral image processing by a multi-channel camera", Image Processing, ICIP 99. Proceedings. 1999 International Conference on , Vol. 3, pp.575-579, (1999)
- [33] D. L. Donoho, "Compressed sensing," IEEE Transactions on Information Theory, vol. 52, no. 4, pp. 1289–1306, (2006).
- [34] A. Wagadarikar, R. John, R. Willett, and D. Brady, "Single disperser design for coded aperture snapshot spectral imaging," Applied Optics, vol. 47, no. 10, (2008).
- [35] DeNatale, J.F. ; Borwick, R. ; Stupar, P. ; Gunning, W. ;Kobrin, P. ; Lauxtermann, S. , "MEMS Tunable Filters for LWIR Spectral Imaging", Optical MEMS and Nanophotonics, IEEE/LEOS International Conference on 2007 , **pp. 169 – 170, (2007)**

- [36] Hennig, Georg ; Brittenham, Gary M. ; Sroka, Ronald ;Kniebuhler, Gesa ; Vogeser, Michael ; Stepp, Herbert, "Bandwidth-variable tunable optical filter unit for illumination and spectral imaging systems using thin-film optical band-pass filters" vol. 8, n.4. pp. 043113 - 043113-7, (2013)
- [37] Iga, Mitsuhiro ; Kakuryu, Nobuyuki ; Tanaami, Takeo ;Sajiki, Jiro ; Isozaki, Katsumi ; Itoh, Tamitake,"Development of thin-film tunable band-pass filters based hyper-spectral imaging system applied for both surface enhanced Raman scattering and plasmon resonance Rayleigh scattering", Review of Scientific Instruments, vol. 83, n.10, pp. 103707 - 103707-9 (2012)
- [38] Yi Wang ; Chuan Peng ; HuanLin Zhang ; Le, H.Q., "Remote spectral imaging with multi-wavelength and tunable, wavelength-modulation lasers", Lasers and Electro-Optics, 2004. (CLEO). Conference on, vol.1. (2004)
- [39] Wenyang Sun ; Kehan Tian ; Barbastathis, G., "Hyper-spectral imaging with volume holographic lenses", Lasers and Electro-Optics, 2005. (CLEO). Conference on, vol. 3. , pp. 2336 – 2338, (2005)
- [40] Wenhai Liu ; Psaltis, D. ; Barbastathis, G., "Spatial and spectral imaging using volume holograms", Lasers and Electro-Optics, 2001. CLEO '01. Technical Digest. Summaries of papers presented at the Conference on pp. 432 – 433, (2001)
- [41] Atlan, Michael ; Gross, Michel, "Wide-field Fourier transform spectral imaging", Applied Physics Letters, vol. 91, n. 11, pp. 113510 - 113510-3, (2007)
- [42] Yuehao Wu ; Mirza, I.O. ; Arce, G.R. ; Prather, D.W., "Development of a digital micromirror device (DMD)-based Snapshot Spectral Imaging (DMD-SSI) system", Photonics Conference (PHO), 2011 IEEE pp. 149 – 150, (2011)



- [43] Wagadarikar, A. A., Pitsianis, N. P., Sun, X., and Brady, D. J., “Video rate spectral imaging using a coded aperture snapshot spectral imager,” *Optical Express*, 17(8), 6368-6388 (2009).
- [44] Yan Na ; Tao Sun ; Cong Wang ; Fangfang Wang, “Panchromatic and multi-spectral images fusion with multi-directional transform”, pp. 2968 – 2971, (2008)
- [45] J. Romberg, “Compressive sensing by random convolution,” *SIAM Journal on Imaging Sciences*, vol. 2, no. 4, pp. 1098–1128, (2009)